Odd-frequency pairing in a one-dimensional topological superconductor

Daijiro TAKAGI

Contents

Abstruct

In this thesis, we relate Majorana fermions to odd-frequency Cooper pairs in a one-dimensional topological superconductor. In Chap. 1, we introduce knowledge to understand this thesis, superconductivity, unconventional superconductors, Majorana fermions, and odd-frequency Cooper pairs.

In Chap. 2, we investigate the superconducting proximity effect including a topological critical point in Kitaev chain systems [1]. Kitaev chain expresses a spinless p-wave superconductor and is useful to explain the Majorana fermions [2]. First, we focus on the relationship between Majorana fermions and odd-frequency Cooper pairs. The relationship has been expressed by calculating the Green's function in a superconducting nanowire [3] and by spectral bulk-boundary correspondence [4]. These works, however, do not address the spatial similarity between the Majorana fermions and odd-frequency Cooper pairs. Our work compares the normal Green's function to the anomalous Green's function at low frequency in the semi-infinite Kitaev chain. The normal (anomalous) Green's function is related to zero-energy states of Majorana fermions (to the odd-frequency pair amplitude). Our result shows that the spatial dependence of Majorana fermions coincides with that of the Majorana fermions at low frequency in the topological phase and at the topological critical point.

Furthermore, we describe the superconducting proximity effect including the topological critical point. Previous works about the proximity effect have used quasiclassical approximation because it is useful for analytical calculations [5]. The approximation, however, does not hold because the wavenumber changes greatly to the energy variation. We calculate the odd-frequency spin-triplet and even-frequency spin-singlet pair amplitude by recursive Green's function method [6]. As a result, we find the odd-frequency pair amplitude causes the proximity

effect even at the topological critical point although the pair amplitude is suppressed.

In Chap. 3, we discuss the topological phase with multiple Majorana fermions in a nonunitary p-wave superconductor in terms of odd-frequency Cooper pairs [7]. Kitaev chain, the spinless p-wave superconductor, hosts one Majorana fermion at the edge. A p-wave superconductor including the spin degree of freedom, magnetic field, and higher older hoppings can access the topological phase with multiple Majorana fermions [8]. Few studies have focused on the behavior of the odd-frequency Cooper pairs in the topological phase hosting multiple Majorana fermions. In this work, we investigate the relationship between the multiple Majorana fermions and the odd-frequency Cooper pairs, and the spin structure of odd-frequency Cooper pairs. It is not easy to focus on the local density of states at the edge of the semi-infinite system because multiple Majorana fermions are located on the same zero-energy. We considered breaking the Majorana fermions by changing system size and by applying magnetic fields that break chiral symmetry. We calculate the system size dependence of low-energy modes corresponding to Majorana fermions and that of odd-frequency pair amplitude at the edge. The result shows the behavior of the odd-frequency pair amplitude provides us remnants of multiple Majorana fermions and the parity of the number of Majorana fermions.

When we focus on the structure of winding numbers characterizing topological states, we find that accessing the topological phase with multiple Majorana fermions requires nonunitary pair potential. We investigate how this non-unitary pair potential affects the spin structure of the odd-frequency Cooper pairs. To express the spin structure of odd-frequency Cooper pairs, we define the $\mathbf{f}$ vector following the $\mathbf{d}$ vector that characterizes spin-triplet pair potential. Our result finds that the direction of the $\mathbf{f}$ vector is fixed to the same direction in any topological phases. Moreover, the spin of the odd-frequency Cooper pairs is tilted toward the direction of the magnetic field.

In Chap. 4, we summarize our work and explain the future works.

Acknowledgments

We are deeply grateful to Prof. Yukio Tanaka, Prof. Yuki Kawaguchi, Assistant Prof. Keiji Yada, Designated Assistant Prof. Shun Tamura, Dr. Shu Suzuki, Dr. Satoshi Ikegaya, Dr. Jorge Cayao, Dr. Mario Cuoco, and Dr. Maria Teresa Mercaldo for supporting this research.

I would like to express my deepest appreciation to Prof. Tanaka for a lot of advice and for proposing the direction of the research while he was busy. I would like to express my gratitude to Prof. Kawaguchi and Assistant Prof. Yada for a meaningful comment on my presentation at the group seminar. I would like to thank Designated Assistant Prof. Tamura for supporting my calculation in the Kitaev chain system. I would like to thank Dr. Suzuki, Dr. Ikegaya, and Dr. Cayao for discussions that helped me understand my research. I am deeply grateful to Dr. Cuoco, and Dr. Mercaldo for supporting the main research in this thesis.

I also would like to thank Prof. Satoshi Kashiwaya, Associate Prof. Kazumasa Iida, and Prof. Masatoshi Sato for undertaking the thesis review.

Finally, I'm full of gratitude to my family for supporting me for many years.

Chapter 1

Introduction

1.1 Superconductivity

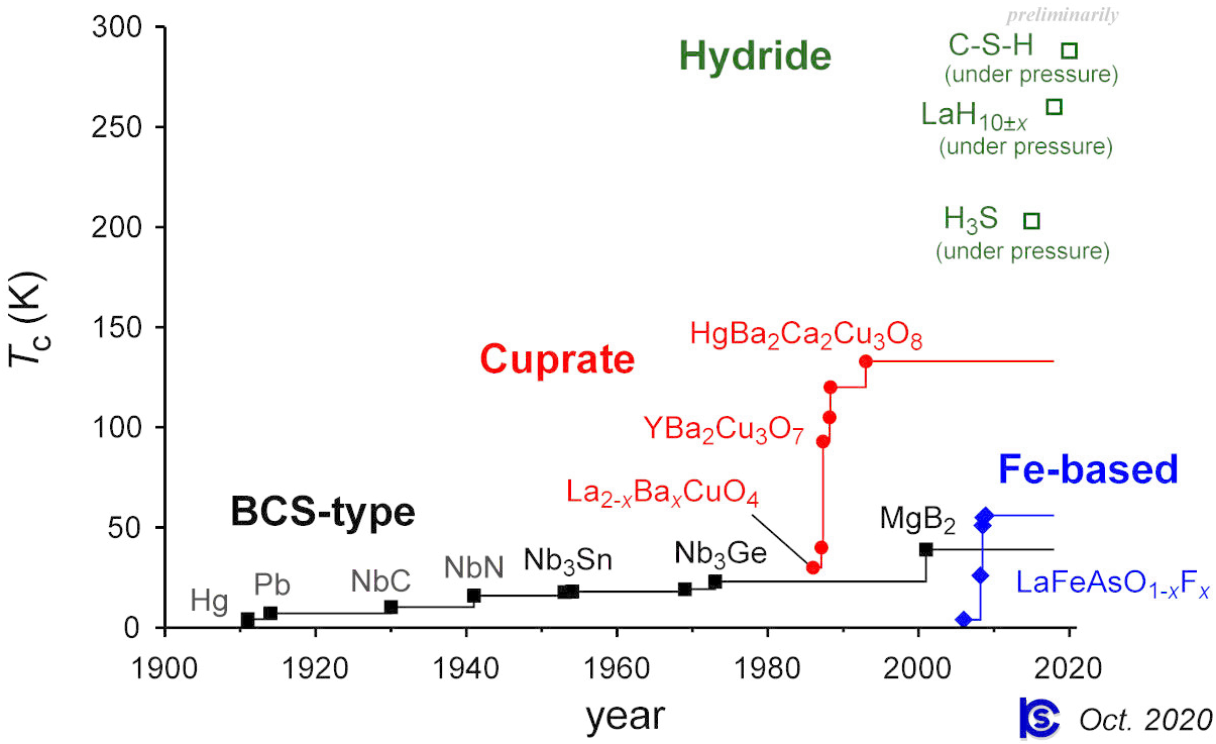

Figure 1.1: Superconducting transition temperature [9].

Superconductivity shows zero resistance at low temperatures, and complete anti-magnetism, the so-called Meissner effect. Because the zero resistance enables us to generate a strong magnetic field, superconductors are used in the magnetically levitated train, MRI, and motors.

In 1908, Kameringh Onness has succeeded in liquefying He. Also, he discovered super-

conductivity in Hg by observing zero resistance in 1911. In 1957, the BCS theory has been published to explain the magnetism of superconductivity [10]. Superconductors with higher transition temperatures have been sought owing to their convenience in the application.

Figure 1.1 shows the history of the superconducting transition temperature. A copper oxide superconductor [red plots in Fig. 1.1] $La_{2-x}Ba_xCuO_4$ has discovered in 1986 [11]. In 1987, a superconducting transition temperature $90K$, exceeding the boiling point of liquid N_2 $77K$, has observed in $YBa_2Cu_3O_7$ [12]. This makes it possible to carry out superconductivity experiments at a lower cost than using liquid He. In 2006, a new type of superconductor, an iron-based superconductor [blue plots in Fig. 1.1] has been discovered [13, 14]. In 2015, It has shown that H_3S becomes superconducting at $203K$ under high pressure [a green plot in Fig. 1.1] [15]. In 2020, superconductivity at $288K$ under high pressure in CH_8S has been discovered. The transition temperature has exceeded $0°C$ for the first time [16].

1.2 BCS theory

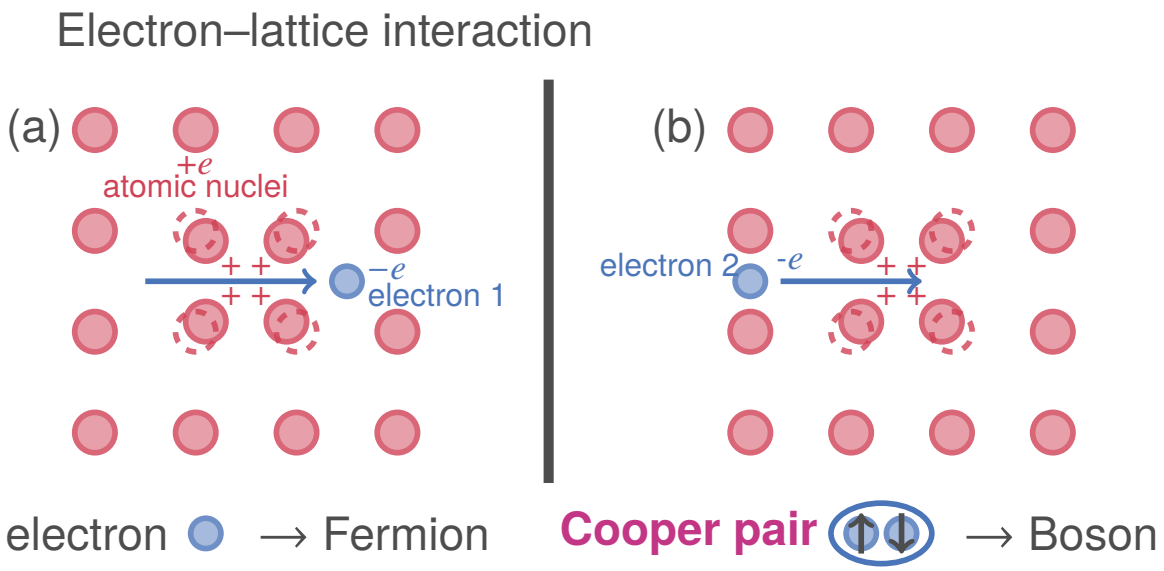

Figure 1.2: Illustration of electron–lattice interaction. Two electrons are attracted through lattice vibrations to form a Cooper pair. (a) One electron distorts the lattice and (b) another is attracted.

Electron–lattice interaction generates a couple of electrons (Cooper pair) causing superconductivity. Let us consider where electrons are moving on the lattice as shown in Fig. 1.2. When

an electron passed among the lattices, a Coulomb acts between the atomic nuclei and an electron, and distorts the lattices [Fig. 1.2 (a)]. Here, the velocity of the lattice distortion (10^2 m/s) is much slower than that of electrons (10^6 m/s). Because the area around the distorted lattice is more positively charged than the other lattices, another electron is attracted by the Coulomb force [Fig. 1.2 (b)]. Thus, it is explained how an attractive force acts between two electrons to form a Cooper pair.

1.3 Unconventional superconductors

There are superconductors with points in which the superconducting gap closes (nodes) in **k** space [Fig. 1.3 (c)–(d)] while the most typical superconductor (s-wave superconductor) has an isotropic gap [Fig. 1.3 (a)]. These are called unconventional superconductors, and classified into p-wave [Fig. 1.3 (c)], d-wave [Fig. 1.3 (b)], f-wave [Fig. 1.3 (d)], etc., depending on how the superconducting gap is open.

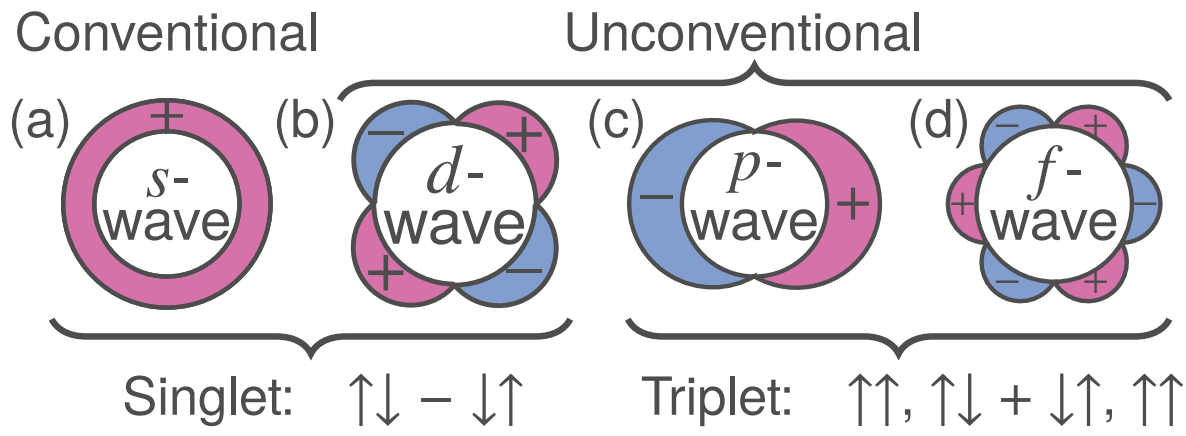

Figure 1.3: Symmetries of superconductivity. (a) s-wave, (b) d-wave, (c) p-wave, and (d) f-wave superconductors. s-wave and d-wave (p-wave and f-wave) are classified into spin-singlet (triplet) superconductors

These unconventional superconductors are not able to be explained by BCS theory describing the property of conventional s-wave superconductors. Copper oxide superconductors [11] such as $YB_2Cu_3O_7$ show high transition temperature [12] above $30K$, which is the limit in the BCS theory. It has been clarified that they have d-wave symmetry from the characteristic surface states and transport phenomena. Spin-triplet superconductors such as p-waves and f-waves

exhibit upper critical magnetic field exceeding Pauli limit the BCS theory estimates.

The pair potential of superconductivity is expressed as follows:

$$\hat{\Delta}(\mathbf{k}) = \begin{bmatrix} \Delta_{\uparrow\uparrow} & \Delta_{\uparrow\downarrow} \\ \Delta_{\downarrow\uparrow} & \Delta_{\downarrow\downarrow} \end{bmatrix}. \tag{1.1}$$

Because spin-singlet (spin-triplet) pair potential satisfies $\Delta_{\sigma\sigma'} = -\Delta_{\sigma'\sigma}$ ($\Delta_{\sigma\sigma'} = \Delta_{\sigma'\sigma}$), the pair potential with spin-singlet and triplet symmetries are obtained as

$$\begin{aligned} \hat{\Delta}_{\text{singlet}}(\mathbf{k}) &= \begin{bmatrix} 0 & \Delta_{\uparrow\downarrow} \\ -\Delta_{\uparrow\downarrow} & 0 \end{bmatrix} \\ \hat{\Delta}_{\text{triplet}}(\mathbf{k}) &= \begin{bmatrix} \Delta_{\uparrow\uparrow} & \Delta_{\uparrow\downarrow} \\ \Delta_{\uparrow\downarrow} & \Delta_{\downarrow\downarrow} \end{bmatrix}. \end{aligned} \tag{1.2}$$

With these relationship in Eq. (1.2), the pair potential shown in Eq. (1.1) is decomposed into spin-singlet and triplet components

$$\hat{\Delta}(\mathbf{k}) = \underbrace{\varphi(\mathbf{k})(i\sigma_y)}_{\text{singlet}} + \underbrace{(\mathbf{d}(\mathbf{k}) \cdot \boldsymbol{\sigma})i\sigma_y}_{\text{triplet}}. \tag{1.3}$$

where $\boldsymbol{\sigma}$ represents Pauli matrices. The spin-triplet pairing are defined by the vector structure, so called $\mathbf{d}$ vector, as

$$\hat{\Delta}_{\text{triplet}}(\mathbf{k}) = (\mathbf{d}(\mathbf{k}) \cdot \boldsymbol{\sigma})i\sigma_y \tag{1.4}$$

$$\Leftrightarrow \mathbf{d}(\mathbf{k}) = \left[\frac{\Delta_{\downarrow\downarrow} - \Delta_{\uparrow\uparrow}}{2}, \frac{\Delta_{\downarrow\downarrow} + \Delta_{\uparrow\uparrow}}{2i}, \Delta_{\uparrow\downarrow} \right]^{\top}. \tag{1.5}$$

The spin direction of a Cooper pair is orthogonal to the $\mathbf{d}$ vector.

The matrix

$$\begin{aligned}\hat{\Delta}_{\text{triplet}}\hat{\Delta}_{\text{triplet}}^{\dagger} &= (\mathbf{d}\cdot\boldsymbol{\sigma})i\sigma_y\left[-i\sigma_y(\mathbf{d}^*\cdot\boldsymbol{\sigma})\right] \\ &= \begin{bmatrix} |\mathbf{d}|^2 + [i\mathbf{d}\times\mathbf{d}^*]_z & [i\mathbf{d}\times\mathbf{d}^*]_x - i[i\mathbf{d}\times\mathbf{d}^*]_y \\ [i\mathbf{d}\times\mathbf{d}^*]_x + i[i\mathbf{d}\times\mathbf{d}]_y & |\mathbf{d}|^2 - [i\mathbf{d}\times\mathbf{d}^*]_z \end{bmatrix} \\ &= |\mathbf{d}|^2\sigma_0 + (i\mathbf{d}\times\mathbf{d}^*)\cdot\boldsymbol{\sigma} \end{aligned} \tag{1.6}$$

evaluates the magnitude of the spin-triplet pair potential [17]. The cross vector $i\mathbf{d}\times\mathbf{d}^*$ is proportional to the spin polarization $\langle\sigma\rangle$ of the spin-triplet Cooper pair. It can be understood from $[i\mathbf{d}\times\mathbf{d}^*]_z = (|\Delta_{\uparrow\uparrow}|^2 - |\Delta_{\downarrow\downarrow}|^2)/2$. The superconductivity with $i\mathbf{d}\times\mathbf{d}^* = 0$ ($\neq 0$) is called a unitary (nonunitary) state because $\Delta_{\text{triplet}}/|\mathbf{d}|$ is a unitary (nonunitary) matrix.

Substances exhibiting spin-triplet superconductivity have been actively searched, recently. For example, Sr_2RuO_4 [18] has been considered to host the spin-triplet p-wave superconductivity by experiments such as NMR (Nuclear Magnetic Resonance) [19] and neutron scattering [20]. However, the symmetry has not been determined owing to several experiments denying the spin-triplet state [21, 22]. Other spin-triplet candidate materials are uranium-based superconductors (UPt_3 [23], UCoGe [24], UTe_2 [25], ...). These substances are considered to have f-wave symmetry. Furthermore, in these substances, the superconducting states coexist with or are adjacent to the ferromagnetic one. From this point of view, it has been pointed out that the expression of the uranium-based superconductivity is due to ferromagnetic fluctuations. Although it is difficult to handle uranium-based superconductors, these candidate materials are attracting the most attention. Except for superconductivity, it has been shown that He_3 [26] realizes a spin-triplet p-wave superfluid state.

1.4 Andreev bound states

In a normal metal/superconductor junction, an electron incident from the normal metal reflects a hole [Fig. 1.4 (a)]. The phenomenon is called Andreev reflection. The normal reflection also occurs in which an electron is reflected as an electron. In the junction, the

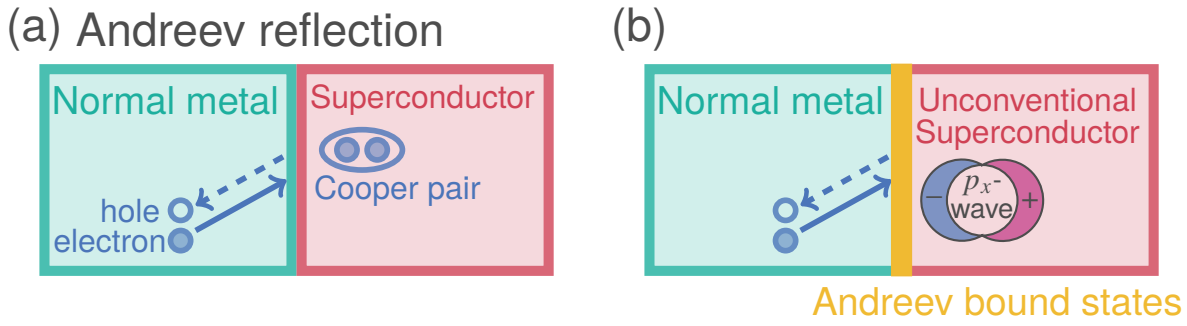

Figure 1.4: (a) Andreev reflection in a normal metal/superconductor junction. (b) Andreev bound states are generated in a normal metal/unconventional superconductor junction, where the pair potential changes its sign in the direction perpendicular to the interface.

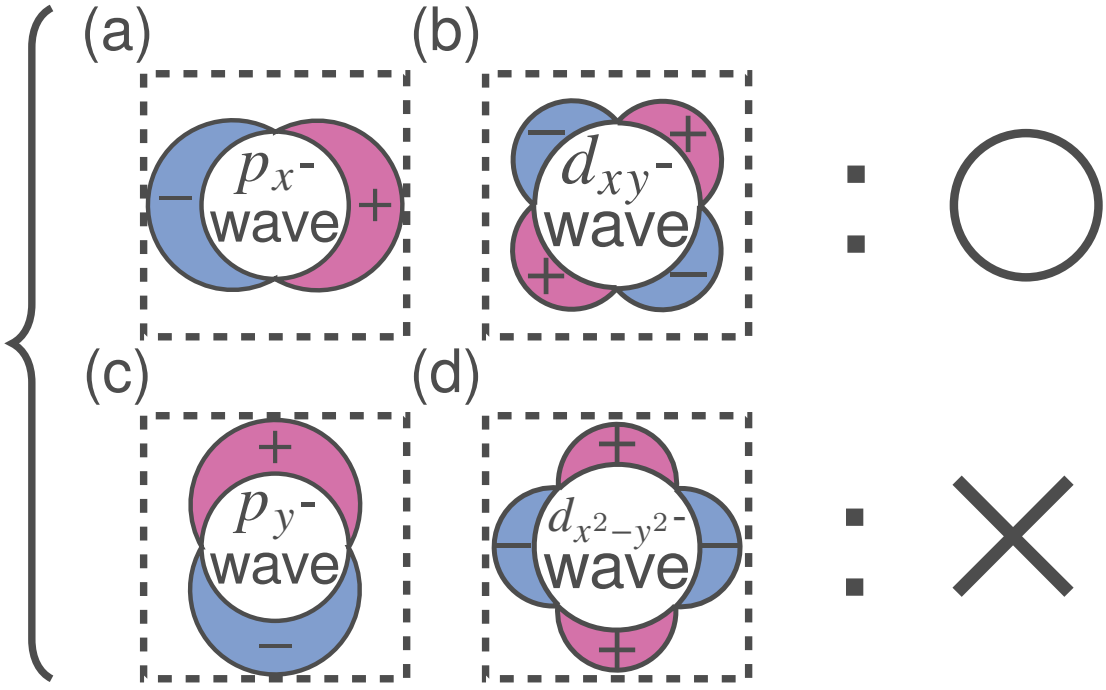

Figure 1.5: Symmetries of superconductor and Andreev bound states. (a) p_x- and (b) d_{xy}-wave superconductor generate Andreev bound states while (c) p_y- and (d) $d_{x^2-y^2}$-wave superconductors do not.

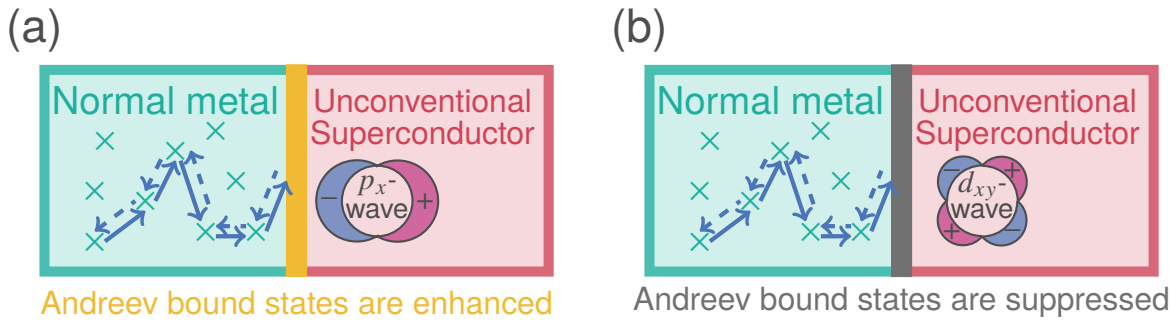

Figure 1.6: (a) p_x-wave and (b) d_{xy}-wave superconductors attached to a normal metal with impurities. Andreev bound states being generated from spin-triplet superconductivity are robust against impurities.

incident electron near the Fermi surface cannot enter because of the superconducting gap. The electron goes through the superconductor as a Cooper.

In a normal metal/unconventional superconductor, in-gap states called Andreev bound states are generated at the interface [Fig. 1.4 (b)]. To create the Andreev bound states, the pair potential must change the sign in the direction perpendicular to the junction interface. Therefore, the Andreev bound states appear in p_x- [Fig. 1.5 (a)] and d_{xy}-ones [Fig. 1.5 (b)] although the bound states do not in s- and p_y- [Fig. 1.5 (c)], and $d_{x^2-y^2}$-waves [Fig. 1.5 (d)]. The large barrier at the interface of the junction strengthens the Andreev bound states.

When the normal metal contains impurities, the incident electron in the metal is scattered. The hole being reflected at the interface traces the path of the incident electron as shown in Fig. 1.6. The impurities in the normal metal enhance the interference between electrons and holes. The enhancement of this interference strengthens the Andreev bound states in the junction of p_x-wave superconductor [Fig. 1.6 (a)] although it suppresses the bound states in that of d_{xy}-wave [Fig. 1.6 (b)]. This is due to the difference between the spin-singlet and triplet. Strengthening the Andreev bound states is explained in the anomalous proximity effect by odd-frequency Cooper pairs [See Sec. 1.7].

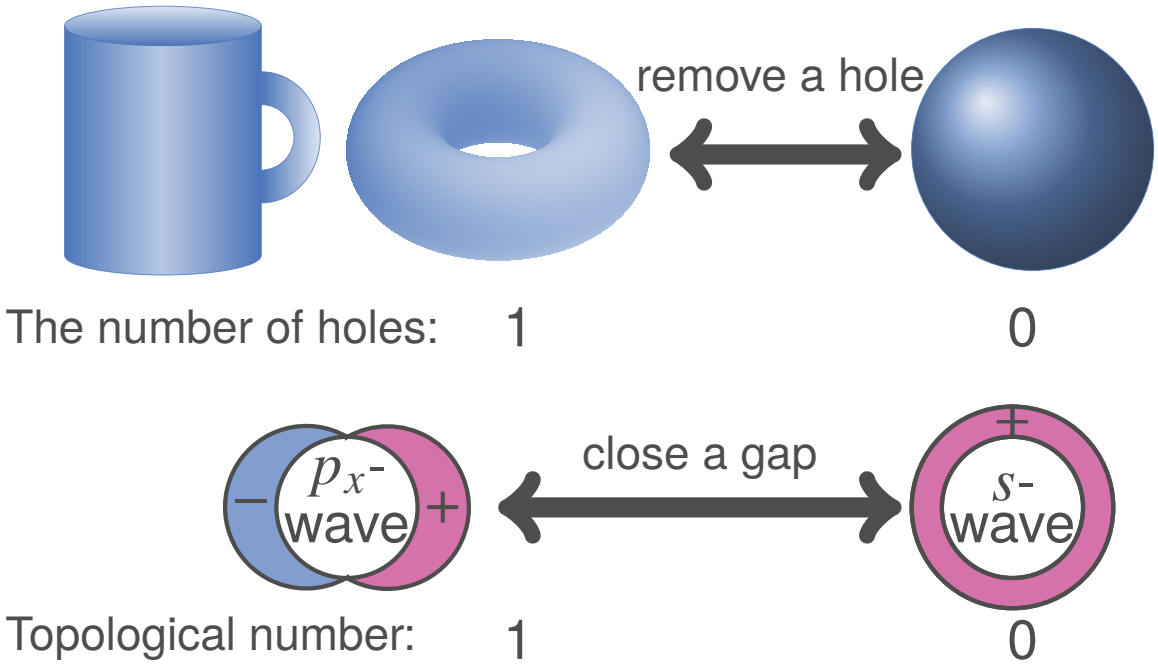

Figure 1.7: (a) The number of holes distinguishes between mugs, donuts, and balls topologically. (b) topological numbers classify superconductivity.

1.5 Topological superconductors

Topology classifies shapes, and their properties are preserved by continuous transformation. For example, the number of holes distinguishes topologically distinguishes mugs, donuts, and balls [Fig. 1.7 (a)]. A mug has the same number of holes (one) as a donut and can be transformed into each other continuously. On the other hand, the number of holes in a donut is different from that in a ball. The donut cannot be transformed into the ball continuously with keeping the number of holes.

Topological superconductivity is classified by topological numbers. The topological number in a topological superconductor is a nonzero integer while that in a trivial superconductor is zero. The topological superconductor cannot change to the trivial one without closing its gap.

The trivial superconductor has an energy gap both in the bulk and the edge. On the other hand, in the topological superconductor, in-gap states at the edge exist although a superconducting gap opens in the bulk. The closure of the energy gap is due to changing the topological number changes between the bulk and the vacuum. This means that the topological number in the bulk makes it possible to predict the edge state of the system. This relationship is called bulk-

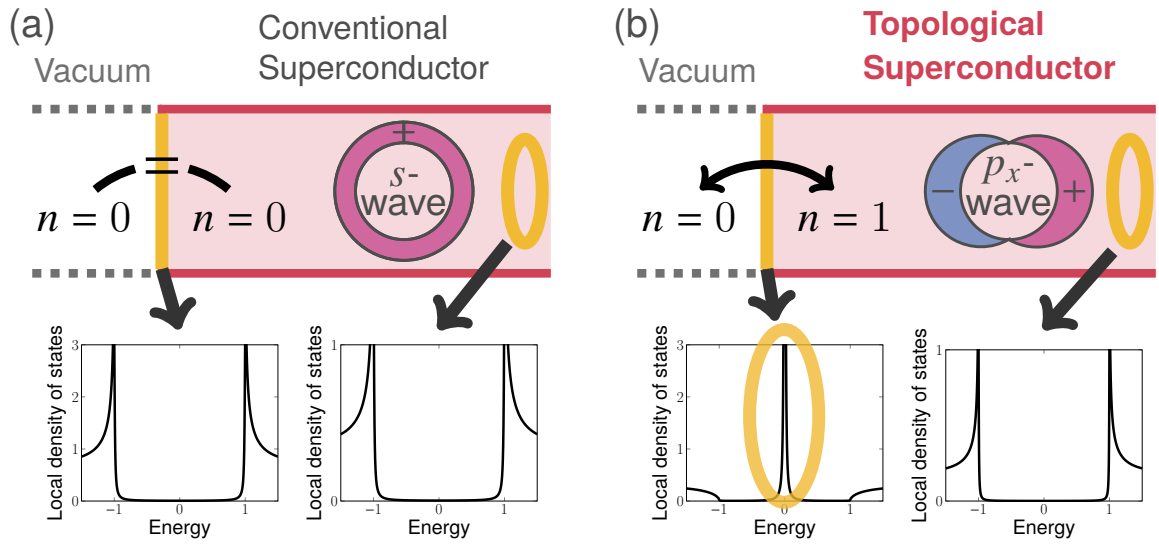

Figure 1.8: Bulk-boundary correspondence in a trivial and (b) topological superconductor. The topological number being defined in the bulk enables us to predict the existence of the edge states.

boundary correspondence, and is the most important concept in understanding the topological superconductivity[27].

1.6 Majorana fermions

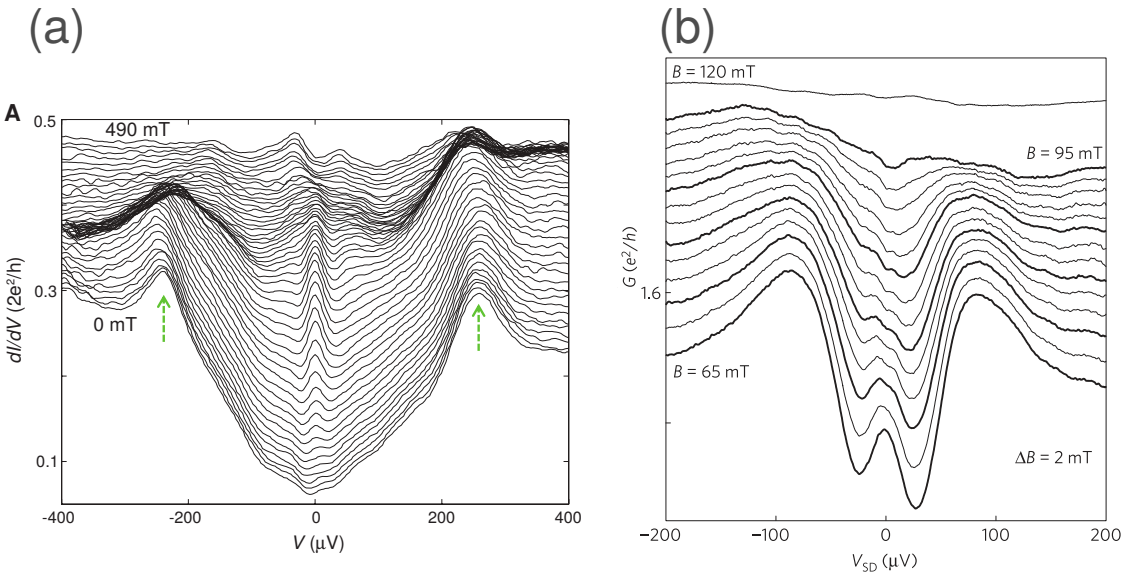

Figure 1.9: Zero-energy peaks of the differential conductance in (a) a NbTiN-InSb nanowire [28] and (b) an Al-InAs nanowire [29].

Majorana fermion is a quasiparticle with no distinction between creation and annihilation.

The quasiparticle satisfies

$$\gamma = \gamma^\dagger \tag{1.7}$$

where γ and $\gamma^\dagger$ represent the annihilation and creation operators, respectively. The Majorana fermion appears as zero-energy states on the edge of a topological superconductor. The zero-energy states have been experimentally observed in a NbTiN-InSb nanowire [Fig. 1.9 (a)] and an Al-InAs nanowire [Fig. 1.9 (b)], a kind of topological superconductor [28, 29]. The Majorana fermion is expected as a qubit that is robust against disorder [30].

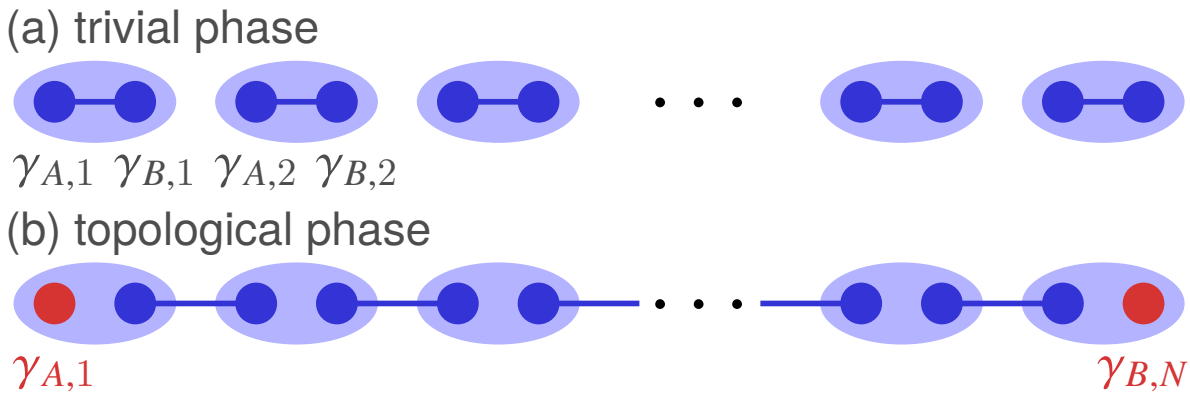

Figure 1.10: Special stuations in a Kitaev chain (a) trivial phase for $t = \Delta = 0$ and $\mu < 0$, (b) topological phase for $t = \Delta$ and $\mu = 0$.

A Kiaev chain [2], a spinless p-wave superconductor, is useful for explaining the Majorana fermion. The Hamiltonian of the Kitaev chain is expressed by

$$H = -\frac{t}{2}\sum_j \left(c_j^\dagger + c_{j+1}^\dagger\right) - \mu \sum_j \left(c_j^\dagger c_j - \frac{1}{2}\right) + \sum_j \left(\frac{\Delta}{2} c_j^\dagger c_{j+1}^\dagger + \text{H.c.}\right), \tag{1.8}$$

where c_j ($c_j^\dagger$) at the site j, t, μ, and Δ means an annihilation (a creation) operator, hopping, chemical potential, and pair potential, respectively. H.c. stands for Hermitian conjugate. We assume that the pair potential is real.

The operators, satisfying the Majorana condition [Eq. (1.7)], are defined as

$$\gamma_{A,j} = \frac{c_j - c_j^\dagger}{2i}, \quad \gamma_{B,j} = \frac{c_j + c_j^\dagger}{2}. \tag{1.9}$$

$\gamma_{A,j} = \gamma_{A,j}^{\dagger}$ and $\gamma_{B,j} = \gamma_{B,j}^{\dagger}$ are easily confirmed. With the anticommutation relation $\{\gamma_{\alpha,j}, \gamma_{\alpha',j'}\} = 2\delta_{\alpha\alpha'}\delta_{jj'}$, Eq. (1.8) is transformed as

$$H = \frac{i\mu}{2}\gamma_{A,j}\gamma_{B,j} + \frac{i}{4}\left[(\Delta + t)\gamma_{A,j+1}\gamma_{B,j} + (\Delta - t)\gamma_{B,j+1}\gamma_{A,j}\right]. \tag{1.10}$$

We consider special situations in the system with N sites. For $t = \Delta = 0$ and $\mu < 0$,

$$H = -\frac{i|\mu|}{2}\sum_{j}^{N}\gamma_{A,j}\gamma_{B,j}. \tag{1.11}$$

This means that A and B at the same site are paired, and the system is topologically trivial [Fig. 1.10 (a)]. For $t = \Delta$ and $\mu = 0$,

$$H = \frac{-it}{4}\sum_{j}^{N-1}\gamma_{B,j}\gamma_{A,j+1}. \tag{1.12}$$

This denotes pairings between A and B on adjacent sites. Here, $\gamma_{A,1}$ and $\gamma_{B,N}$ represent isolated Majorana fermions at each edge [Fig. 1.10 (b)]. This situation is located in a topological phase where Majorana fermions are completely localized at the edges.

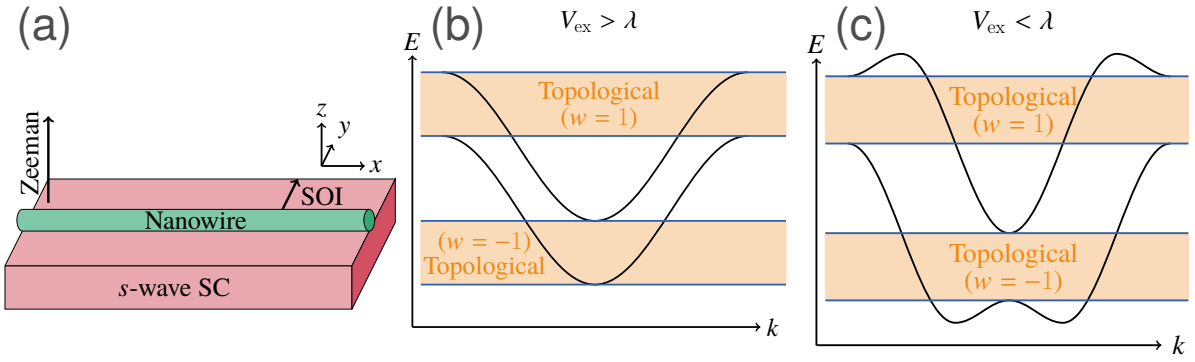

Figure 1.11: (a) A sketch of a Rashba superconducting nanowire. Dispersion in normal states of a Rashba nanowire for (a) $\lambda < V_{ex}$ and (b) $V_{ex} = \lambda$. λ: spin-orbit coupling, V_{ex}: Zeeman field, w: winding number (topological number).

A Rashba superconducting nanowire, similar to the Kitaev chain, is a feasible model. In this system, a semiconducting nanowire with strong Rashba spin-orbit coupling and applied magnetic fields is in proximity to a s-wave superconductor [31, 32] as shown in Fig. 1.11(a). This system becomes equal to a p-wave superconductor at low energies [3]. A system with

	$\omega \to -\omega$	$\sigma \leftrightarrow \sigma'$	$p \to -p$
ESE	even(+)	singlet	even
ETO	even	triplet	odd
OTE	odd(−)	triplet	even
OSO	odd	singlet	odd

Figure 1.12: Symmetries of Cooper pairs including odd-freqency dependence. Red (blue) text means odd- (even-) functions. Conventional classification is highlighted in gray.

Majorana fermions being constructed from s-wave has been originally proposed in superfluids of cold atoms [33, 34].

The Hamiltonian

$$\begin{aligned}\mathcal{H} = &-t\sum_{j,\alpha}\left(c^{\dagger}_{j+1,\alpha}c_{j,\alpha} + c^{\dagger}_{j,\alpha}c_{j+1,\alpha}\right) + \sum_{j,\alpha,\beta} c^{\dagger}_{j,\alpha}\left(-\mu\hat{\sigma}_0 - V_{\mathrm{ex}}\hat{\sigma}_3\right)_{\alpha,\beta} c_{j,\beta} \\ &+ i\frac{\lambda}{2}\sum_{j,\alpha,\beta}\left[c^{\dagger}_{j+1,\alpha}\left(\hat{\sigma}_2\right)_{\alpha,\beta} c_{j,\beta} - c^{\dagger}_{j,\alpha}\left(\hat{\sigma}_2\right)_{\alpha,\beta} c_{j+1,\beta}\right] + \sum_{j}\left(\Delta c^{\dagger}_{j,\uparrow}c^{\dagger}_{j,\downarrow} + \mathrm{H.c.}\right), \end{aligned} \tag{1.13}$$

describes the Rashba superconducting nanowire with spin α (β), Rashba spin-orbit coupling λ, and Zeeman fields V_{ex}. The system takes the topological phase for $\sqrt{\mu^2 + \Delta^2} < V_{\mathrm{ex}}$. The magnitude relationship between the magnetic field and the spin-orbit coupling changes greatly the shape of the energy band in the normal state ($\Delta = 0$) of the system [Fig. 1.11 (b) and Fig. 1.11 (c)].

1.7 Odd-frequency Cooper pairs

Odd-frequency Cooper pairs are a special couple of two electrons. In general, pair function $F_{\sigma\sigma'}$ describing a Cooper pair obeys Fermi–Dirac statistics

$$F_{\sigma\sigma'}(\mathbf{p}) = -F_{\sigma'\sigma}(-\mathbf{p}) \tag{1.14}$$

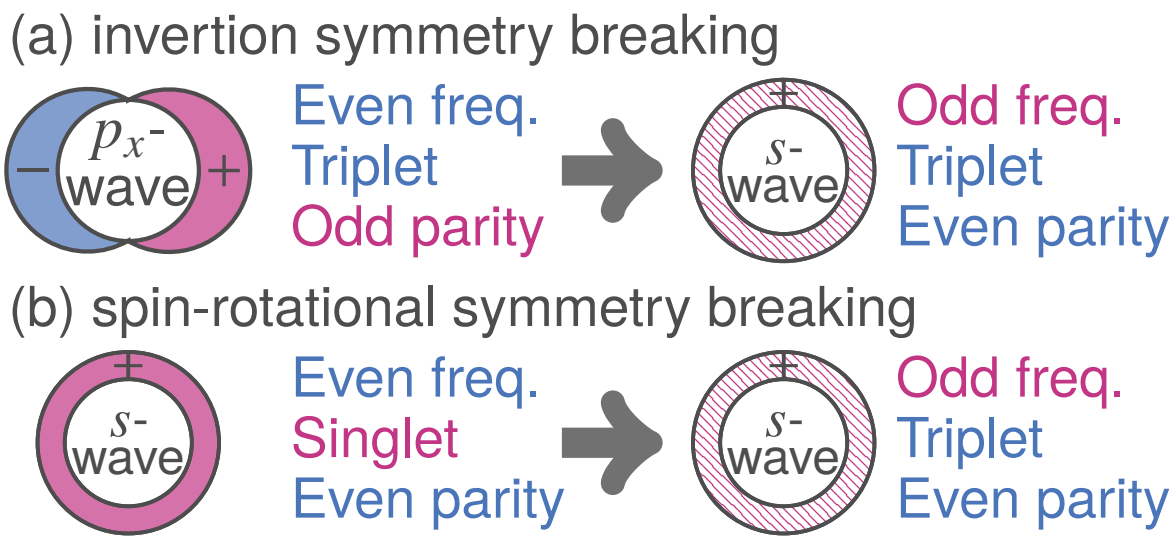

Figure 1.13: Odd-freq spin-triplet even-parity s-wave Cooper pairs are generated from eve-frequency Coper pairs by (a) inversion symmetry breaking and (b) spin-rotational symmetry breaking.

with the spin σ and momentum $\mathbf{p}$. Here, we assume that the pair function is limited to even-frequency dependence. Conventionally, the symmetries of Cooper pairs are classified into spin-singlet even-parity and spin-triplet odd-parity pairings [Fig. 1.12]. When we limit to one-dimensional systems, spin-singlet even-parity and spin-triplet odd-parity correspond to s-wave and p-wave pairings, respectively.

We are also able to consider frequency degrees of freedom ω in Eq. (1.14) as follows

$$F_{\sigma\sigma'}(\mathbf{p},\omega) = -F_{\sigma'\sigma}(-\mathbf{p},-\omega) \tag{1.15}$$

This relaxing the limitation of even-frequency dependence enables odd-frequency Cooper pairs to exist. For example, odd-frequency spin-triplet even-parity and odd-frequency spin-singlet odd-parity pairings are possible [35, 36] as shown in Fig. 1.12. The odd-frequency pairing means that two electrons form a Cooper pair at different times. Although this fact is difficult for us to imagine intuitively, the odd-frequency pairings have been theoretically shown to exist as pair amplitudes.

These odd-frequency Cooper pairs are difficult to exist in the bulk of a single-band superconductor. They are secondarily generated from conventional even-frequency Cooper pairs. Symmetry breaking plays an important role in the generation of the odd-frequency Cooper pairs.

The symmetry breaking involves inversion symmetry breaking (constructing edge, surface, and junction) and spin-rotational symmetry breaking (applying magnetic fields) [Fig. 1.13]. For example, because inversion symmetry breaking changes the parity, odd-frequency spin-triplet even-parity pairing is generated from even-frequency spin-triplet odd-parity pairing [Fig. 1.13 (a)]. Also, spin rotational symmetry breaking generates odd-frequency spin-triplet even-parity pairing from even-frequency spin-singlet even-parity pairing [Fig. 1.13 (b)].

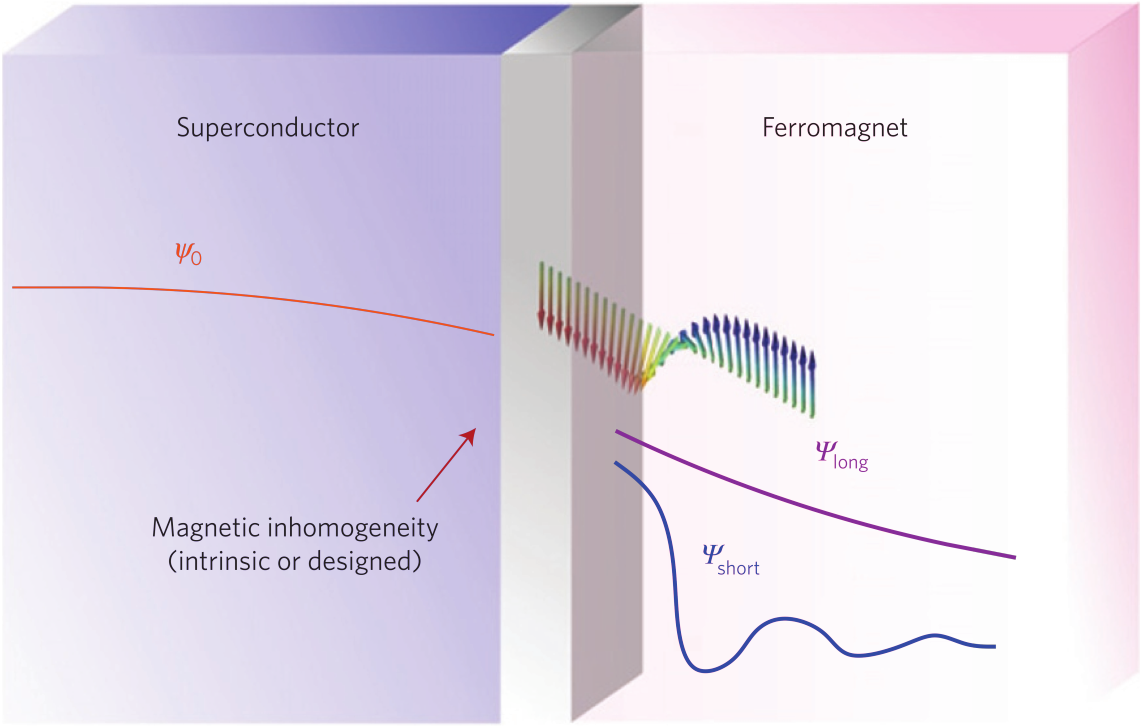

Figure 1.14: Depiction of the long-range proximity effect in a superconductor and ferromagnet junction [37].

The odd-frequency pairing causes strange transport phenomena and magnetic responses. For example, they includes long-range proximity effect [40, 37, 41], anomalous proximity effect [42, 43, 44], and paramagnetic responses [41, 39]. In a ferromagnet / *s*-wave superconductor junction, when the spin direction of a Cooper pair is parallel to that of the ferromagnet, it can penetrate into the ferromagnet over the long distance [Fig. 1.14]. On the other hand, a Cooper pair with the different spin direction from that of the ferromagnet is broken by the magnetization of it. This long-range proximity effect is due to the **SPIN-TRIPLET** property of the odd-frequency s-wave Cooper pairs. The proximity effect is useful as a filter that selects the spin direction of a Cooper pair owing to the difference of penetration depth [37].

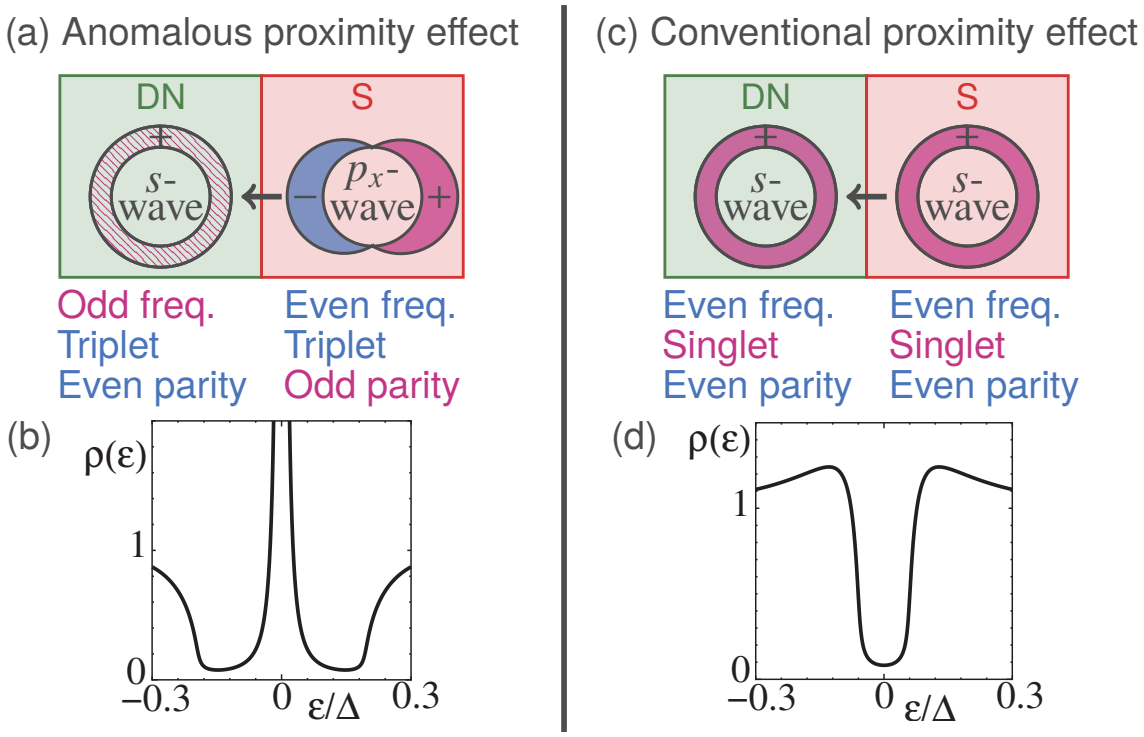

Figure 1.15: In (a) anomalous proximity effect, odd-frequency spin-triplet s-wave pairs penetrate into a diffusive normal metal (DN) from a spin-triplet superconductor (S). (b) The local density of states has a zero-energy peak [38]. In (c) conventional proximity effect, even-frequency spin-singlet even-parity s-wave pairs penetrate into DN with keeping the symmetry. (d) The local density of states has a gap-like structure [38].

In a diffusive normal metal attached to a spin-triplet superconductor [Fig. 1.15 (a)], a peak of the local density of states [Fig. 1.15 (b)] and a quantized differential conductance appears at zero energy (bias voltage) [42]. This phenomenon, so-called the anomalous proximity effect, is in contrast to the conventional proximity effect [Fig. 1.15 (c)], which exhibits gap structure [Fig. 1.15 (d)] near zero energy in a diffusive normal metal attached to s-wave superconductor Figs. 1.15 (a) and 1.15 (b). The zero-energy states are robust against impurities in the diffusive normal metal. This is because a pair function of an odd-frequency **S-WAVE** Cooper pair does not change its sign in space. Whereas, Cooper pairs with the sign change, for example, p-wave, d-wave, . . . , are broken by the impurities because of canceling the pair function.

The anomalous proximity effect helps us distinguish the symmetry of superconductors, theoretically. For example, in a diffusive normal metal / p_x-wave superconductor junction, odd-frequency spin-triplet s-wave Cooper pairs are generated from even-frequency spin-triplet p_x-wave Cooper pairs by translational symmetry breaking [38]. The generated odd-frequency Cooper pairs cause a zero-energy peak of the local density states; the anomalous proximity effect

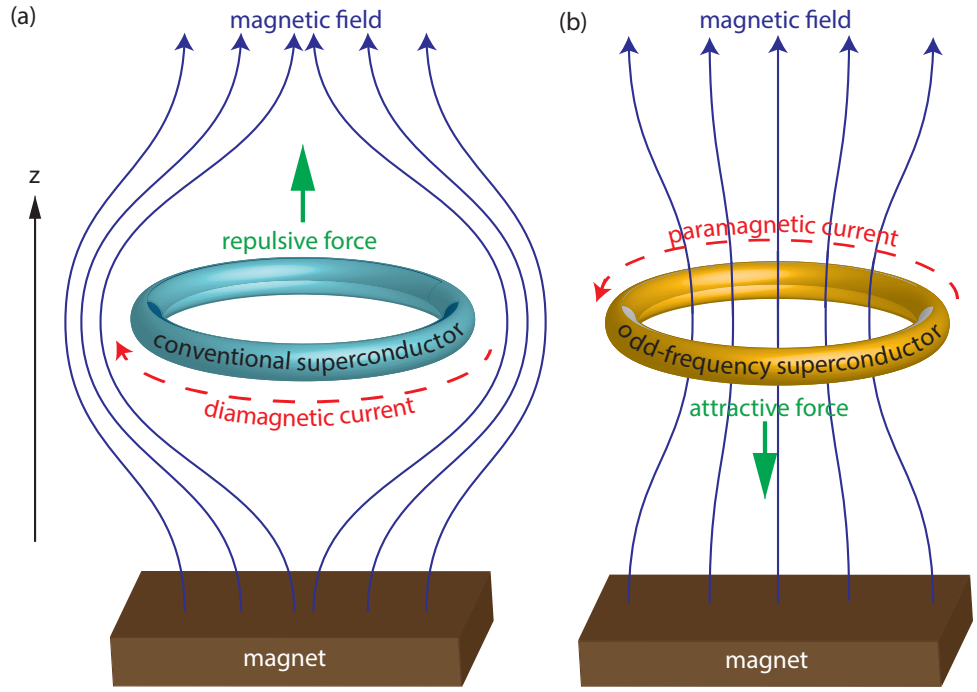

Figure 1.16: (a) diamagnetic response of conventional superconducting ring and (b) paramagnetic response of odd-frequency superconducting ring [39].

occurs. On the other hand, in a diffusive normal metal / $d_{x^2-y^2}$-wave superconductor junction, odd-frequency spin-singlet p_y-wave Cooper pairs are generated from even-frequency spin-singlet $d_{x^2-y^2}$ Cooper pairs by translational symmetry breaking. The generated odd-frequency Cooper pairs, however, are broken by the impurities because of the sign change of the pair function; the anomalous proximity effect does not occur. This means that the anomalous proximity effect makes it possible to distinguish between p-wave and d-wave superconductors.

The odd-frequency Cooper pairs also cause a strange magnetic response. Conventionally, a superconductor excludes the applied magnetic field below the lower critical. This phenomenon, the so-called Meissner effect, is similar to a diamagnetic response. Furthermore, the Meissner effect is one of the definitions of superconductivity. In contrast, systems in which odd-frequency Cooper pairs are dominant attract the applied magnetic field. For instance, these systems include small topological superconducting disks and rings [45, 46, 39].

Chapter 2

Odd-frequency Cooper pairs and proximity effect in a Kitaev chain junction including a topological critical point

2.1 Introduction

It has been shown that the odd-frequency Cooper pair pair amplitude related to the Majorana fermion is inversely proportional to the frequency, recently [4]. This chapter focuses on this odd-frequency Cooper pairs causing the proximity effect. The existence of the zero-energy surface Andreev bound states enhances the odd-frequency pairing in junctions of spin-singlet d-wave or spin-triplet p-wave superconductor [48, 49, 50, 51, 52, 38, 53]. However, the odd-frequency spin-triplet s-wave pairs, being generated at the edge of spin-triplet p-wave or f-wave superconductors, can penetrate into the normal metal with impurities [5, 42, 43, 44, 54]. The phenomenon is the anomalous proximity effect. This effect creates a zero-energy peak of the local density of states in the normal metal with impurities and a quantized zero-bias conductance [42, 43, 44, 54]. This is different from the conventional proximity effect in a spin-singlet s-wave

This chapter is based on Phys. Rev. B 101, 024509 (2020) and arXiv:1809.09324 (2020) [1, 47]

superconductor junction [55].

No anomalous proximity effects have been observed experimentally yet. A diffusive normal metal/p-wave superconductor junction is the simplest system to investigate this effect [42, 43, 44]. No candidate substance has confirmed the p-wave superconductivity.

Therefore, methods for creating p-wave superconductivity form s-wave have been studied [33, 34, 31, 32]. A semiconducting nanowire including Rashba spin-orbit coupling and Zeeman fields attached to the s-wave superconductor is the most famous method [31, 32]. In addition, the low-energy excitation in the superconducting nanowire is equivalent to that in the p-wave superconductor [3]. The zero-energy peaks of the local density of states have been observed in several experiments, [28, 29].

Quasiclassical approximations are useful for studying the proximity effect analytically [56, 57, 58]. This approximation substitutes Fermi wavenumber k_{F} for the wavenumber near the Fermi surface. When the energy is sufficiently greater than the pair potential, this approximation holds. The quasiclassical approximation is effective in investigating the surface Andreev bound states that appear in unconventional superconductors [48, 49, 50, 51, 52]. Moreover, this approximation is also used to explain the anomalous proximity effect [42, 43, 44].

There are, however, situations where this approximation is not available. It is possible to reach the situation by manipulating parameters in a p-wave superconductor system. Specifically, the situation is a topological phase around a topological critical point.

The most efficient way is to use a model of spinless p-wave superconductor, the so-called Kitaev chain, to investigate the vicinity of the topological critical point [2]. By manipulating the chemical potential, it is possible to transition between the topological and non-topological phases. Since the topological phase around the topological critical point can exist in the real model [29], it makes sense to investigate this situation. In this chapter, by using recursive Green's function [6], we demonstrate the behavior of odd-frequency Cooper pairs in the Kitaev chain in the regime where the quasiclassical approximation becomes invalid.

We first investigate the relationship between Majorana fermions and odd-frequency Cooper pairs in the semi-infinite Kitaev chain. We compare the spatial dependence of the odd-frequency pair amplitude and that of the local density of states at zero frequency in the regime containing

the topological critical point. Here, it has been already known that the zero-energy density of states corresponding to the Majorana fermion is strongly related to the odd-frequency pair amplitude [3]. We discover a strange behavior of odd-frequency spreading towards the bulk at the topological critical point. Moreover, the behavior is consistent with the spatial dependence of the zero-energy density of states.

We next investigate the anomalous proximity effect of the Kitaev chain attached to a diffusive normal metal. Particularly, we compare the odd-frequency spin-triplet s-wave pair amplitude robust against impurities to the even-frequency spin-triplet p-wave pair potential inheriting the pair potential. We show that the odd-frequency pair amplitude being enhanced in the topological phase decrease sharply around the topological critical point.

Also, we focus on the local density of states and zero-bias conductance in the normal metal containing impurities. In the topological regime, the local density of states has a zero-energy peak and a quantized zero-bias conductance peak. Both the local density of states and the differential conductance have sharp peaks being derived from the zero-energy states. We discuss changes in peak width with respect to the length of the diffusive normal metal and the strength of impurity scattering. The zero-bias conductance is not quantized while the zero-energy states exist at the topological critical point. Finally, To distinguish between the topological and metal-insulator transition in the Kitaev chain, we investigate the spatial dependence of the even-frequency spin-singlet s-wave pair amplitude in the junction.

Section 2.2 begins with an explanation of the Kitaev chain. We introduce the recursive Green's function method in Sec. 2.3 We discuss the behavior of the odd-frequency pair amplitude in the semi-infinite Kitaev chain and its junction in Secs. 2.4–2.5.

2.2 Kitaev chain

The Kitaev chain that describes a one-dimensional spinless p-wave is expressed as follows:

$$\mathcal{H} = -t \sum_j \left(c_j^\dagger c_{j+1} + c_{j+1}^\dagger c_j \right) - \mu \sum_j c_j^\dagger c_j + \sum_j \left(\Delta c_j^\dagger c_{j+1}^\dagger + \text{H.c.} \right). \tag{2.1}$$

The role of the parameters is the same as Eq. (1.8) Since we are considering completely spin-polarized states $|\uparrow\uparrow\rangle$, the spin degree of freedom is ignored. The topological state of the Kitaev chain is explained by the energy dispersion with zero pair potential [Fig. 2.1].

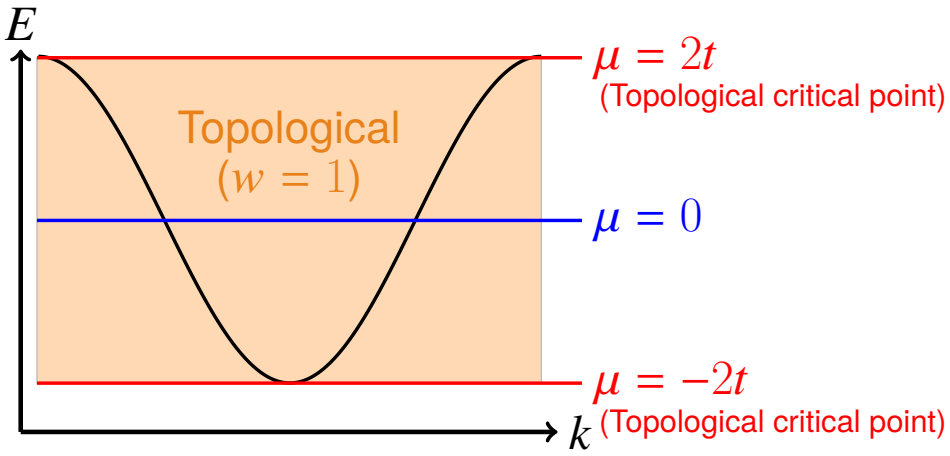

Figure 2.1: Energy dispersion for the Kitaev chain with zero pair potential. It takes a topological phase when the Fermi surface is present ($|\mu| < 2t$). At the topological critical point, μ is located at the edge of the energy band. The winding number becomes one in the topological phase. [1]

The Fermi energy crosses the energy band in the topological phase. The non-topological states of the Kitaev chain mean insulators. In this chapter, we call the transition point from the topological to the non-topological phase the topological critical point ($\mu = \pm 2t$).

The topological states of the Kitaev chain are explained by the winding number, a kind of topological invariant:

$$w = \frac{-1}{4\pi i}\int_{-\pi}^{\pi} \mathrm{Tr}\left[\Gamma H^{-1}(k)\partial_k H(k)\right] \mathrm{d}k = \begin{cases} 1 & (|\mu| < 2t) \\ 0 & (|\mu| > 2t) \end{cases}, \tag{2.2}$$

with the chiral operator $\Gamma = \tau_x$ anticommutative with the Hamiltonian. Here, τ_x is a Pauli matrix. The Hamiltonian $H(k)$ in $\mathbf{k}$ space is obtained by Fourier transforming the Hamiltonian in real space and expressing it in a quadratic form $\mathcal{H} = (1/2)\sum_k [c_k^\dagger, c_{-k}] H(k) [c_k, c_{-k}^\dagger]^{\mathrm{T}}$ with wavenumber k. In the topological phase, the winding number becomes 1 while 0 in the non-topological phase. The definition of the winding number is not allowed at the topological critical point where the superconducting gap closes. Therefore, the winding number does not change continuously from the topological phase to the non-topological phase.

2.3 Green's function method

This section shows how to calculate the odd-frequency pair amplitude and the local density of states from Hamiltonian through Green's function. The retarded and advanced Green's functions are defined as [59]

$$\begin{aligned}\check{G}^{R(A)}(E,j,j') &= \left\{\left[(E+(-)i\delta_\epsilon)\,I-H\right]^{-1}\right\}_{j,j'} \\ &= \begin{bmatrix} G^{R(A)}_{j,j'}(E) & F^{R(A)}_{j,j'}(E) \\ \tilde{F}^{R(A)}_{j,j'}(E) & \tilde{G}^{R(A)}_{j,j'}(E)\end{bmatrix},\end{aligned} \tag{2.3}$$

with the energy E, an infinitesimal positive number δ_ϵ, an identity matrix I. The Green's function in Eq. (2.3) allows the calculation of the odd- and even-frequency pair amplitude, the local density of states, and the differential conductance. The retarded Green's function given by Eq. (2.3) expresses the local density of states as follows:

$$\rho(E,j) = -\frac{1}{\pi}\mathrm{Im}\left[G^R_{j,j}(E)\right]. \tag{2.4}$$

The differential conductance in the Kitaev chain junction is obtained by the Lee–Fisher formula [60]:

$$G_{\mathrm{NS}}(E,j) = \frac{t^2e^2}{h}\mathrm{Tr}\left[\frac{\tau_0+\tau_z}{2}(-\bar{G}_{j,j+1}\bar{G}_{j,j+1} - \bar{G}_{j+1,j}\bar{G}_{j+1,j} + \bar{G}_{j,j}\bar{G}_{j+1,j+1} + \bar{G}_{j+1,j+1}\bar{G}_{j,j})\right], \tag{2.5}$$

with $\bar{G}_{j,j'} = (G^A_{j,j'} - G^R_{j,j'})/2i$.

The Matsubara Green's function being obtained by the frequency replacement $E+(-)i\delta \to i\omega_n$ in Eq. (2.3) is useful for calculating the pair amplitude. The pair amplitude representing the correlation of two electrons satisfy the Fermi–Dirac statistics:

$$\tilde{F}_{jj'\sigma\sigma'}(i\omega_n) = -\tilde{F}_{j'j\sigma'\sigma}(-i\omega_n), \tag{2.6}$$

with the spin σ and σ' two electrons in a Cooper pair. This statistic limits the symmetry of

Cooper pairs to the following four types: even-frequency spin-singlet even-parity (ESE), odd-frequency spin-triplet even-parity (OTE) [35], even-frequency spin-triplet odd-parity (ETO), and odd-frequency spin-singlet odd-parity (OSO) [36]. Since no magnetic field is applied in this chapter, the Cooper pairs existing in the Kitaev chain system are odd-frequency spin-triplet even-parity and even-frequency spin-triplet odd-parity. The pair amplitudes in the Kitaev chain systems are described by

$$f^{\mathrm{OTE}}(j) = \frac{1}{2}\left[\tilde{F}_{j,j}(i\omega_n) - \tilde{F}_{j,j}(-i\omega_n)\right], \tag{2.7}$$

$$f^{\mathrm{ETO}}(j) = \frac{1}{2}\left[\frac{\tilde{F}_{j+1,j}(i\omega_n) - \tilde{F}_{j,j+1}(i\omega_n)}{2} + \frac{\tilde{F}_{j+1,j}(-i\omega_n) - \tilde{F}_{j,j+1}(-i\omega_n)}{2}\right]. \tag{2.8}$$

We also focus on the even-frequency spin-singlet even-parity pairing in a s-wave superconductor junction. The pair amplitude is expressed as follows:

$$f^{\mathrm{ESE}}_{\uparrow\downarrow-\downarrow\uparrow}(j) = \frac{1}{2}\left[\tilde{F}_{j,j,\uparrow,\downarrow}(i\omega_n) + \tilde{F}_{j,j,\uparrow,\downarrow}(-i\omega_n)\right] \tag{2.9}$$

in consideration of the spin degree of freedom.

2.4 Semi-infinite Kitaev chain

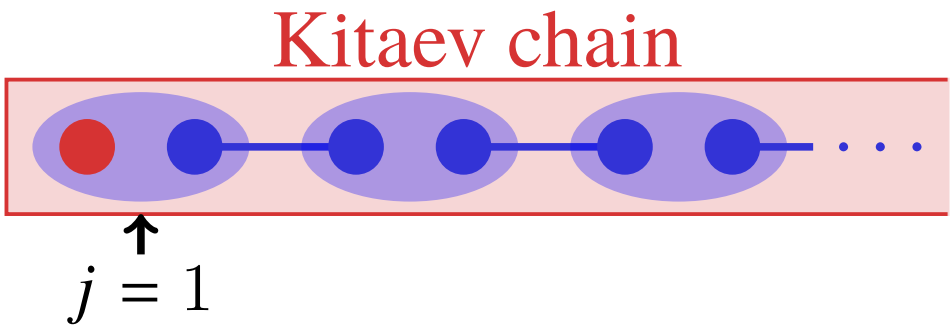

Figure 2.2: Illustration of a semi-infinite Kitaev chain. j: site. [1]

From the viewpoint of the spatial dependence, we examine the odd-frequency pair amplitude and zero-energy states in a semi-infinite Kitaev chain as shown in Fig. 2.2. The relationship between Majorana fermions and odd-frequency Cooper pairs has been investigated by comparing

Green's functions [3]. No attention, however, has been paid to the similarity of the spatial dependence between them. By the recursive Green's function, we compare the spatial dependence of odd-frequency pair amplitude to that of zero-energy states [see App. 2.8.1 with detail].

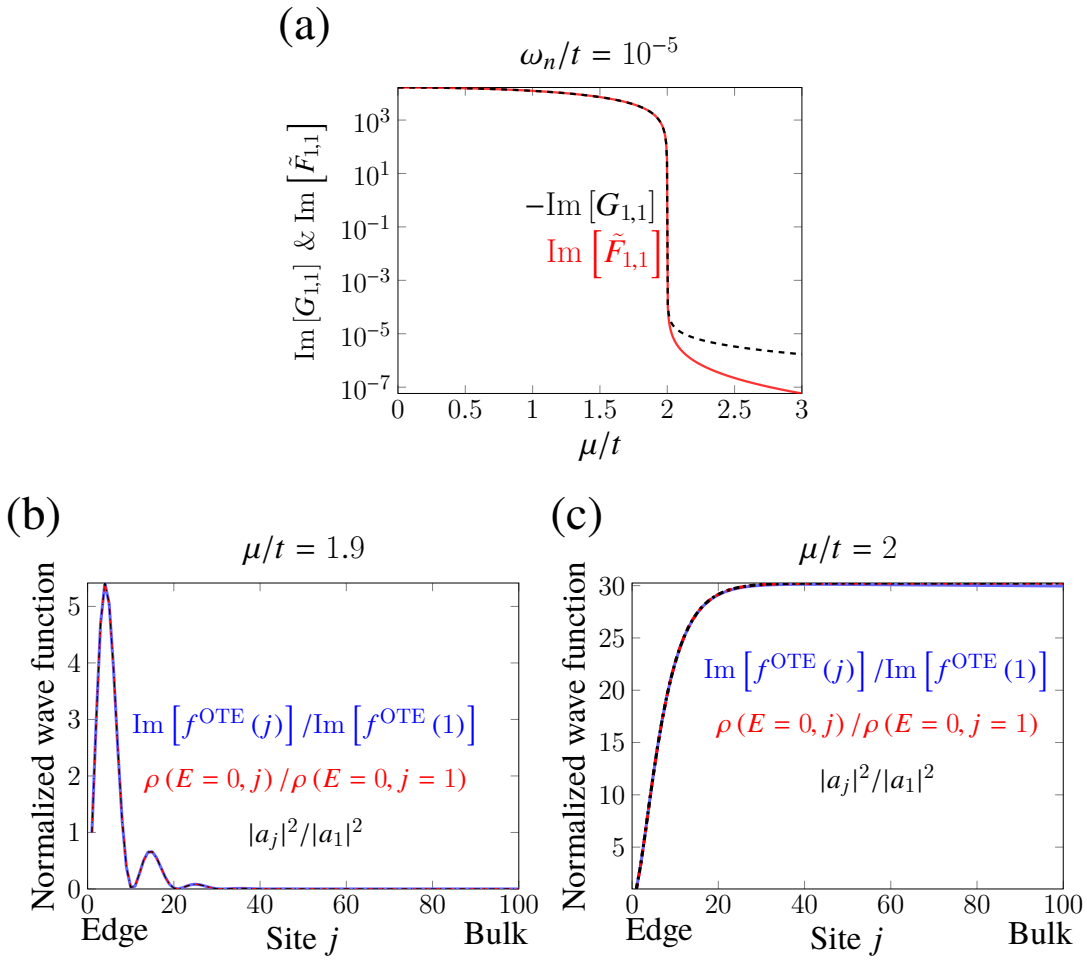

Figure 2.3: (a) Comparison of the normal Green's function $-\mathrm{Im}[G_{1,1}]$ and the anomalous Green's function $\mathrm{Im}[\tilde{F}_{1,1}]$ at the edge $j = 1$ of the system. The horizontal axis represents the chemical potential. ω_n: Matsubara frequency. $\mathrm{Im}[\tilde{F}_{1,1}]$: the odd-frequency pair amplitude. $\omega_n/t = 10^{-5}$. In the topological phase $|\mu| < 2t$, $-\mathrm{Im}[G_{1,1}]$ corresponds to the zero-energy states being derived from Majorana fermions. Comparison of the odd-frequency pair amplitude $\mathrm{Im}[f^{\mathrm{OTE}}(j)]$, the zero-energy local density of states $\rho(E = 0, j)$, and the probability density of Majorana wave function $|a_j|^2$ for (b) $\mu/t = 1.9$ (topological phase) and (c) $\mu/t = 2$ (topological critical point). $\omega_n/t = 10^{-5}$, $\delta_\epsilon/t = 10^{-5}$. We calculate the three values being normalized by the values at the edge $j = 1$ of the semi-infinite Kitaev chain. $\Delta/t = 0.1$. [1]

We plot the normal and anomalous Green's function as a function of the chemical potential μ in Fig. 2.3(a). The normal $-\mathrm{Im}[G_{1,1}]$ and $\mathrm{Im}[F_{1,1}]$ anomalous Green's function are related to the zero-energy local density of states and the odd-frequency pair amplitude being derived from the Majorana fermion, respectively. For the low frequency $\omega_n/t = 10^{-5}$, their values are

equal to each other in the topological phase [Fig. 2.3 (a)]. Their relative error for $\mu = 0$ becomes about 10^{-9}. These Green's function $-\mathrm{Im}[G_{1,1}]$ and $\mathrm{Im}[F_{1,1}]$ being maximized for $\mu = 0$, is suppressed as the chemical potential increases. Near the topological critical point $\mu = 2t$, their values decrease sharply. These Green's functions become almost zero ($-\mathrm{Im}[G_{1,1}] \sim 10^{-5}$ and $\mathrm{Im}[F_{1,1}] \sim 10^{-7}$) in the non-topological regime.

For $\Delta = t$, the similarity of the Green's functions in the low frequency shown in Fig. 2.3 can be shown analytically.

$$\lim_{\omega_n \to 0} \left\{ \mathrm{Im}\left[G_{1,1}\right] + \mathrm{Im}\left[\tilde{F}_{1,1}\right] \right\} \simeq \lim_{\omega_n \to 0} \begin{cases} \frac{-\omega_n}{\omega_n^2 + 4t^2} & \text{(topological)} \\ \frac{-\omega_n}{\omega_n^2 + \mu^2} & \text{(non-topological)} \end{cases} = 0. \tag{2.10}$$

[Detailed calculations are written in App. 2.9]. Equation (2.10) shows that $\mathrm{Im}[G_{1,1}] + \mathrm{Im}[\tilde{F}_{1,1}]$ depends on the chemical potential μ in the non-topological phase, whereas on hopping t in the topological phase, at the low frequency. As the chemical potential moves away from the topological critical point toward the non-topological phase, $\mathrm{Im}[G_{1,1}] + \mathrm{Im}[\tilde{F}_{1,1}]$ quickly converges to zero.

The Majorana wave function in the semi-infinite Kitaev chain is expressed as follows [61]:

$$a_j = a_1 C^{j-1} \left\{ \cos\left[\beta(j-1)\right] + \frac{1}{\tan\beta} \sin\left[\beta(j-1)\right] \right\}, \tag{2.11}$$

with $\beta = \arctan\left(\sqrt{4t^2 - 4\Delta^2 - \mu^2}/\mu\right)$ and $C = \sqrt{t - \Delta}/\sqrt{t + \Delta}$. Figures 2.3 (b) and (c) show the comparison of the odd-frequency pair amplitude $\mathrm{Im}[f^{\mathrm{OTE}}(j)]$ [Eq. (2.7)], the zero-energy local density of states $\rho(E = 0, j)$ [Eq. (2.4)], and the probability density of Majorana wave function $|a_j|^2$. These normalized values are plotted as a function of the site j.

In the topological phase, the spatial dependence of the three values is equal to each other as shown in Fig. 2.3 (b). The spatial vibrations are derived from Friedel oscillations whose wavelength is inversely proportional to k_{F}. When this vibration appears, $(\mu/2)^2 + \Delta^2 < t^2$ is satisfied [61]. Even at the topological critical point, the spatial dependence of these three values is equal to each other [Fig. 2.3(c)]. Their spatial dependent features are, however, dramatically different from that in the topological phase [Fig. 2.3(b)]. In the region close to the bulk ($j > 40$),

they become constant without vibration.

It has been known that the odd-frequency pair amplitude is localized at the edge. At the topological critical point, it is, however, surprising that the odd-frequency pair amplitude spreads toward the bulk of the Kitaev chain [Fig. 2.3(c)]. Our finding shows the possibility of realizing odd-frequency superconductivity in the bulk of the semi-infinite system at the topological critical point.

Analytically, we confirm the existence of the odd-frequency pair amplitude in the bulk. In the low-frequency limit and for $0 < \Delta < t$ and $|\mu| \leq 2t$, the odd-frequency pair amplitude as a function of site j is written by

$$\mathrm{Im}\left[f^{\mathrm{OTE}}(j)\right] = \mathrm{Im}\left[f^{\mathrm{OTE}}(1)\right] C^{2j-2} \left|\cos\left[\beta(j-1)\right] + \frac{1}{\tan\beta}\sin\left[\beta(j-1)\right]\right|^2 . \tag{2.12}$$

being based on the Majorana wave function in Eq. (2.11)

We limit the parameters as $j \gg 1$, $\Delta/t = \alpha$ $(0 < \alpha < 1)$, and $\mu/t = 2$. The spatial dependence of the odd-frequency pair amplitude is obtained as follows:

$$\frac{\mathrm{Im}\left[f^{\mathrm{OTE}}(j)\right]}{\mathrm{Im}\left[f^{\mathrm{OTE}}(1)\right]} \simeq \left(\frac{1+\alpha}{2\alpha}\right)^2 , \tag{2.13}$$

with $\beta = \arctan(i\alpha)$. This equation shows that the odd-frequency pair amplitude converges to a constant value near the bulk of the system at the topological critical point. For $\alpha = 0.1$, $\mathrm{Im}[f^{\mathrm{OTE}}(j)]/\mathrm{Im}[f^{\mathrm{OTE}}(1)]$ becomes 30.25, which is equal to the plot at $j = 100$ in Fig. 2.3(c). Our findings overturn the fact that odd-frequency Cooper pairs are localized at the edge of the system.

2.5 Kitaev chain junction

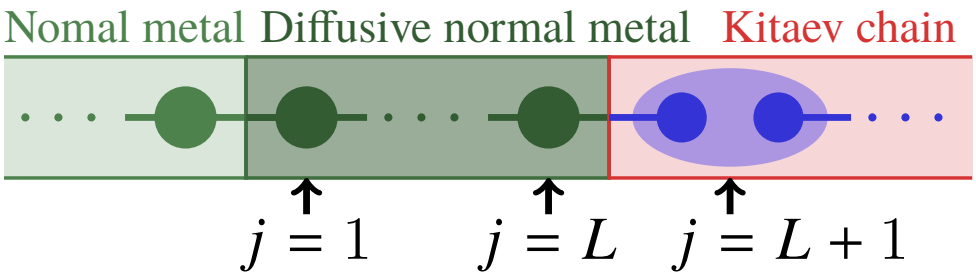

Figure 2.4: Illustration of a normal metal/diffusive normal metal/Kitaev chain junction. j: site, L: the length of the diffusive normal metal. [1]

We examine the proximity effect in a Kitaev chain junction as drawn in Fig. 2.4. The normal metal/diffusive normal metal/Kitaev chain junction is represented by the Hamiltonian:

$$\begin{aligned}\mathcal{H} = &-t\sum_{j}\left(c_j^\dagger c_{j+1} + c_{j+1}^\dagger c_j\right) - \mu_{\mathrm{N}}\sum_{j\le L} c_j^\dagger c_j - \mu\sum_{L+1\le j} c_j^\dagger c_j \\ &+ \sum_{L+1\le j}\left(\Delta c_j^\dagger c_{j+1}^\dagger + \mathrm{H.c.}\right) + \sum_{1\le j\le L} V_j c_j^\dagger c_j, \end{aligned} \tag{2.14}$$

with the random potential $V_j \in [-W, W]$, the length of the diffusive normal metal L, the chemical potential μ_{N} in normal region $j \le L$

Numerically, we demonstrate the pair amplitude as a function of the site including topological critical point. In the topological phase far from the topological critical point, a quasiclassical approximation holds and $k_F\xi \ge 1$. To connect with the observables in the experiment, we also investigate the local density of states in the diffusive normal metal region and the differential conductance The recursive Green's function method [6] is useful for calculating these values numerically [The specific formulation is shown in App. 2.8.1]. These calculations are averaged with the 10^5 impurity samples.

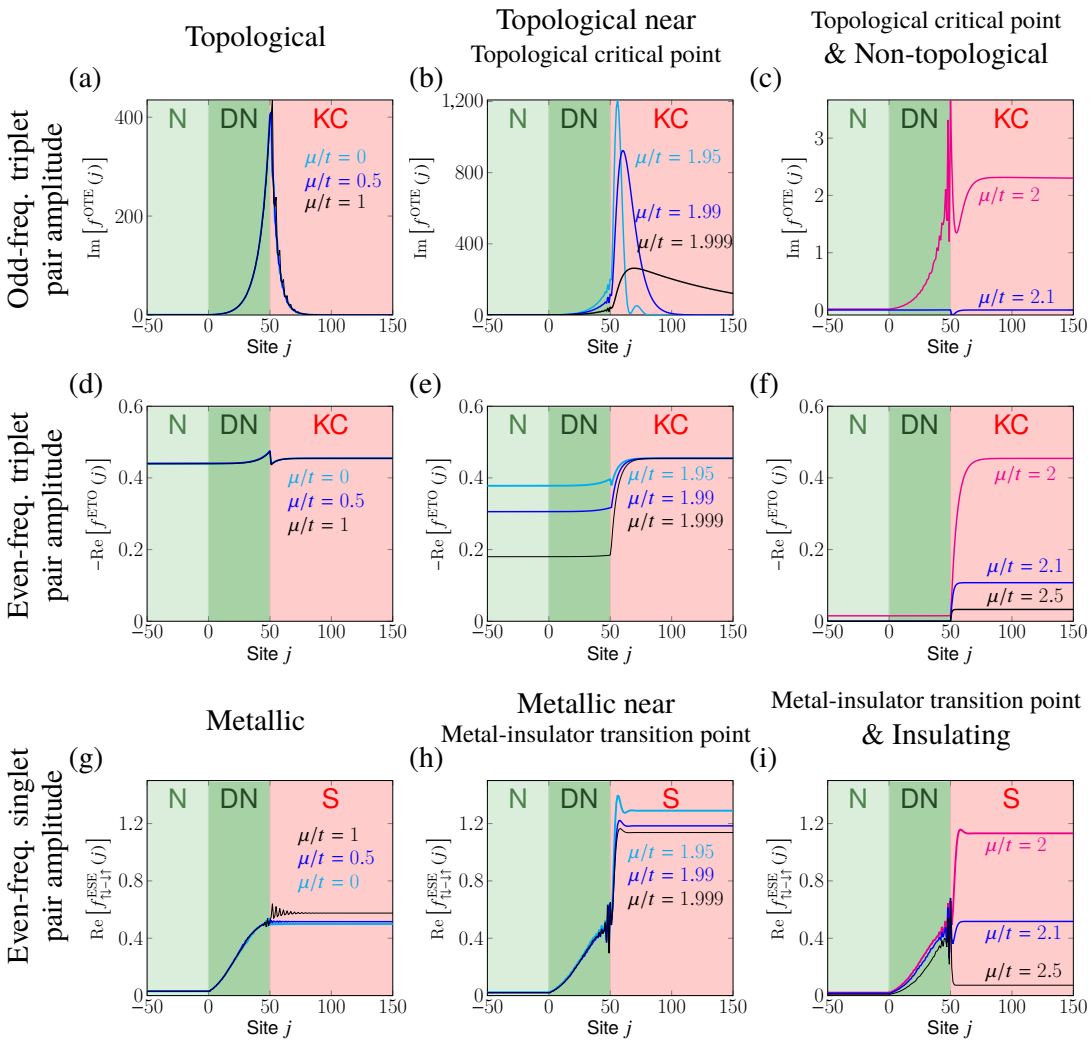

Figure 2.5: (a)–(c) The odd-frequency spin-triplet even-parity f^{OTE} and (d)–(f) even-parity spin-triplet odd-parity f^{ETO} pair amplitude as a function of the site j in the normal metal (N)/diffusive normal metal (DN)/Kitaev chain (KC) junction. (g)–(i) the even-frequency spin-singlet even-parity pair amplitude $f^{\mathrm{ESE}}_{\uparrow\downarrow-\downarrow\uparrow}$ as a function of the site j in the normal metal/diffusive normal metal/s-wave superconductor (S) junction. We select the parameters as $\mu_{\mathrm{N}}/t = 0.5$, $\Delta/t = 0.1$, $\omega_n/t = 10^{-5}$, $L = 50$, and $W/t = 3$. (a) (d) $\mu/t = 0$, 0.5, 1 for the topological phase, (b) (e) $\mu/t = 1.95$, 1.99, 1.999 for the topological phase near the topological critical point, (c) (f) $\mu/t = 2$ at the topological critical point and $\mu = 2.1$, 2.5 for the non-topological phase. (g) $\mu/t = 0$, 0.5, 1 for the metallic phase, (h) $\mu/t = 1.95$, 1.99, 1.999 for the metallic phase near the metal–insulator transition point. (i) $\mu/t = 2$ at the metal–insulator transition point and $\mu/t = 2.1$, 2.5 for the insulating phase. [1]

Additionally, we describe the odd-frequency spin-singlet even-parity pair amplitude in a normal metal/diffusive normal metal/s-wave superconductor junction. This system is expressed by substituting $\sum_\sigma c^\dagger_\sigma c_\sigma$ and $c^\dagger_{j,\uparrow} c^\dagger_{j,\downarrow}$ for $c^\dagger c$ and $c^\dagger_j c^\dagger_{j+1}$, respectively, in the Hamiltonian [Eq. (2.14)]. In this system, the s-wave superconductor region becomes the metallic (insulating) phase for $|\mu| < 2t$ ($|\mu| > 2t$). Therefore, the topological critical point in the Kitaev chain

corresponds to the metal–insulator transition point in the s-wave superconductor.

First, we describe the pair amplitude as a function of the site in the Kitaev chain junction [Fig. 2.5]. At the interface between the diffusive normal metal and the Kitaev chain, the odd-frequency pair amplitude hosts a sharp peak in the topological phase far from the topological critical point, as shown in Fig. 2.5(a). The peak height is 10^8 times larger than the value at $j = 150$. In the Kitaev chain region ($L + 1 \leq j$), the odd-frequency pair amplitude vibrates. As explained in the semi-infinite system [Sec. 2.4], this vibration is also derived from Friedel oscillations. On the contrary, the pair amplitude penetrating into the diffusive normal metal does not vibrate [Fig. 2.5(a)].

The even-frequency pair amplitude has no vibration in the Kitaev chain region in the topological phase far from the topological critical point [Fig. 2.5(d)]. The pair amplitude 0.44 at $j = 25$ is smaller than the odd-frequency pair amplitude 19.28. Our results show that this proximity effect is dominated by the odd-frequency Cooper pairs.

We next focus on the topological phase near the topological critical point. The odd-frequency pair amplitude decreases and the wavelength of the vibration in the Kitaev chain increases [Fig. 2.5(b)] as the chemical potential increases. The odd-frequency pair amplitude is reduced, dramatically. The peak height becomes 1.4% of that for $\mu/t = 1.999$. As shown in Fig. 2.5(c), however, the proximity effect into the diffusive normal metal is still caused. On the other hand, even-frequency spin-triplet pair amplitude barely penetrates into the diffusive normal metal [Fig. 2.5(f)]. In the Kitaev chain region, the odd-frequency spin-triplet even-parity and even-frequency spin-triplet odd-parity pair amplitudes are mixed at the topological critical point [Fig. 2.5(f)].

The odd-frequency pair amplitude is reduced to $\sim 10^{-3}$ in the non-topological phase. Also, the even-frequency pair amplitude decreases in the non-topological phase as the chemical potential increases. However, the pair amplitude is still nonzero in the Kitaev chain region Fig. 2.5(f). In the topological phase and at the topological critical point, the even-frequency pair amplitude in the Kitaev chain region hardly changes with the increase of the chemical potential Figs. 2.5(d)–2.5(f).

To distinguish between the topological and metal–insulator transitions, we plot the even-

frequency spin-singlet even-parity pair amplitude as a function of the site j in the normal metal/diffusive normal metal/s-wave superconductor junction in Figs. 2.5(g)–2.5(i). In the metallic phase far from the metal–insulator transition point, the even-frequency pair amplitude vibrates rapidly in the s-wave superconductor and enters into the diffusive normal metal without vibrations, as shown in Fig. 2.5(g). As shown in [Fig. 2.5(h)], the pair amplitude oscillates at the boundary between the diffusive normal metal and Kitaev chain, and its wavelength becomes long in the s-wave superconductor near the metal–insulator transition point. Owing to the zero Fermi wavenumber, the oscillation of the even-frequency pair amplitude in the s-wave superconductor is removed at the metal–insulator transition point [Fig. 2.5(i)]. The even-frequency pair amplitude in the s-wave superconductor decreases as the chemical potential increases. Similar to the even-frequency spin-triplet odd-parity pair amplitude in the Kitaev chain junction shown in Fig. 2.5(i), the pair amplitude keeps the nonzero value. Even in the insulator phase, the even-frequency spin-singlet even-parity pair amplitude enters into the diffusive normal metal unlike the even-frequency spin-triplet odd-parity in the Kitaev chain junction.

To provide a summary of the proximity effect, the behavior of the odd-frequency spin-triplet even-parity pair amplitude is far from that of the even-frequency spin-triplet odd-parity pair amplitude. In the topological phase, the odd-frequency pair amplitude, localized at the interface between the diffusive normal metal and the Kitaev chain, decreases dramatically at the topological critical point. The odd-frequency pair amplitude is almost eliminated in the non-topological phase while the even-frequency spin-singlet even-parity pair amplitude remains in the Insulating phase in the s-wave superconductor junction. Therefore, we can emphasize that the odd-frequency pair amplitude is suppressed by the topological transition of the Kitaev chain. This is due to the existence of Majorana fermions accompanied by the odd-frequency pair amplitude in the topological phase.

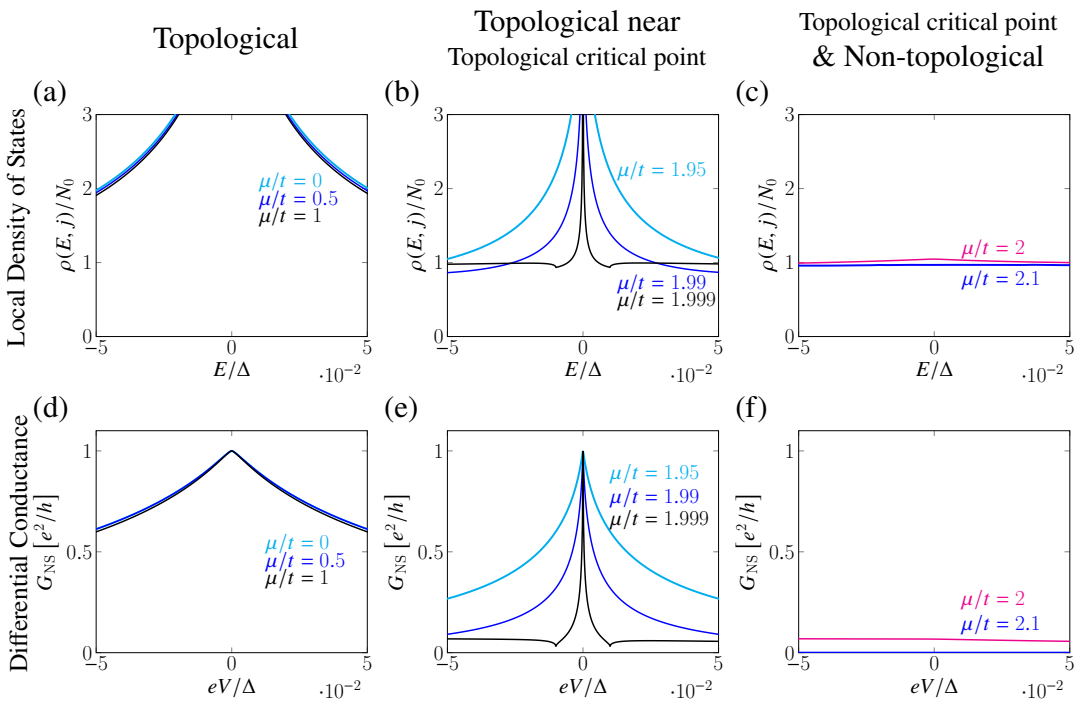

Figure 2.6: (a)–(c) the local density of states as a function of the energy, and (d)–(f) the differential conductance ($j = -10$) as a function of the bias voltage eV, in the Kitaev chain junction. Parameters are selected as $\Delta/t = 0.1$, $\mu_{\rm N}/t = 0.5$, $W/t = 1$, $L = 20$, $\delta_\epsilon/t = 10^{-8}$, (a) $j = 10$, and (b) $j = -10$. The Kitaev chain belongs to (a)(d) the topological phase for $\mu/t = 0$, 0.5, 1, to (b)(e) the topological phase near the topological critical point for $\mu/t = 1.95$, 1.99, 1.999, and to (c)(f) the topological critical point and non-topological phase for $\mu/t = 2$ and $\mu = 2.1$. [1]

In order to connect the odd-frequency pair amplitude to the physical quantities in the experiment, we show the local density of states and the differential conductance in Fig. 2.6. Figures 2.6(a)–(c) show the local density of states $\rho\left(E, j\right)/N_0$ in Eq. (2.4) at $j = 10$ (the diffusive normal metal region) in the normal metal/diffusive normal metal/Kitaev chain junction. The local density of states is normalized by that at the Fermi energy in the infinite system of the clean normal metal. The zero-energy peak of the local density of states is generated in the topological phase [5], as shown in Fig. 2.6 (a). The peak is due to the Majorana fermion enhancing the odd-frequency pair amplitude in Fig. 2.5(a). As shown in Fig. 2.6 (b), the height of the peak becomes smaller and the width of the peak is narrower with the increase of the chemical potential. At the topological critical point, the local density of states at zero energy, however, remains as depicted in Fig. 2.6 (c). The zero-energy states are linked to the presence of the odd-frequency pair amplitude [a red plot in Fig. 2.5(c)]. This correspondence has been shown by the quasiclassical approximation [62]. The zero-energy states disappear in the non-topological

phase as shown in Fig. 2.6 (c). The disappearance of the zero-energy states is connected with the suppression of the odd-frequency pair amplitude [a blue plot in Fig. 2.5 (c)].

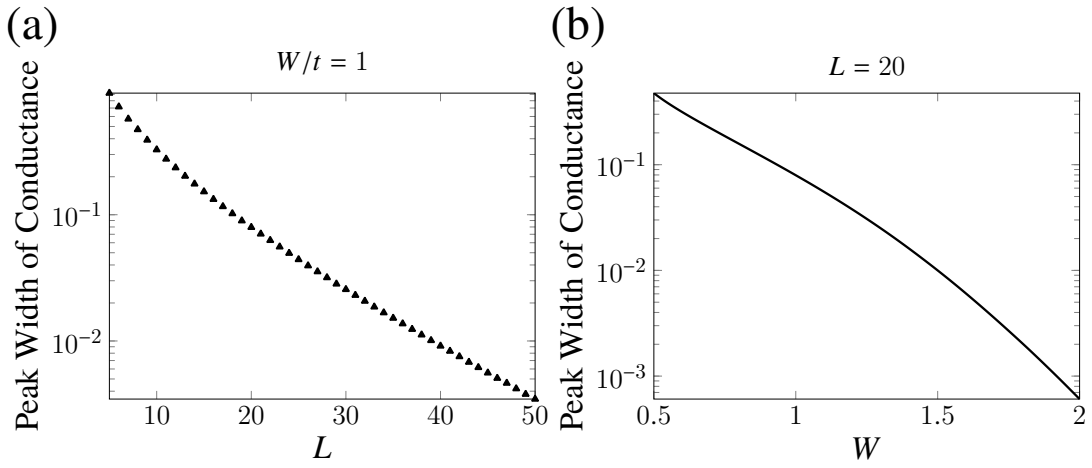

Figure 2.7: The peak width of differential conductance in the normal metal/diffusive normal metal/Kitaev chain junction for (a) the length of the diffusive normal metal L and (b) the strength of the impurities W. The peak width is defined by half-width at half maximum. Parameters are selected as $\Delta/t = 0.1$, $\mu_{\rm N}/t = 0.5$, $\mu = \mu_{\rm N}/t = 0$, $\delta_\epsilon/t = 10^{-8}$, $j = -10$, (a) $W/t = 1$, and (b) $L = 20$. [1]

We plot the differential conductance as a function of the bias voltage in the normal metal/diffusive normal metal/Kitaev chain junction in Figs. 2.6 (d)–2.6 (f) Figures 2.6 (d), 2.6(e), and Fig. 2.6(f) describe plots in the topological phase, that in the topological phase near the topological critical point, and that in the non-topological phase, respectively. Owing to the zero-energy surface Andreev bound states and the chiral symmetry, the zero-bias conductance peak is quantized [54] in the topological phase, as shown in Fig. 2.6 (e). The peak width decreases with the increase of the chemical potential [Fig. 2.6 (e)]. Because the zero-bias conductance peak is not limited to the quantized value in the absence of a gap [54], the quantization is removed at the topological critical point [Fig. 2.6(f)]. The peak of the conductance disappears in the non-topological phase [Fig. 2.6(f)]. To realize the perfect resonance nature at $eV = 0$ more clearly, The standard deviation is also plotted in App. 2.10 to investigate the effect of the impurities on the zero-bias conductance peak.

We focus on the effect of the impurities on the peak width of the conductance. The peak width is about the Thouless energy and is reduced by the impurities [63]. We plot the peak width of the conductance as the half-width at half maximum in Fig. 2.7. The detailed calculation to

obtain the half-width at half maximum is written in App. 2.8.2. The peak width as a function of the length of the diffusive normal metal L and the strength of the impurities W is described in Fig. 2.7(a) and Fig. 2.7(b), respectively. Figures 2.7 (a) and 2.7 (b) show the peak width of differential conductance $\propto \exp(c_1 L + c_2 W)$ with $c_1 < 0$ and $c_2 < 0$. The result indicates that the impurities highlight the peculiarity of the conductance at zero-bias voltage. Also, the peak width of the zero-energy local density of states is shown in App. 2.10.

Table 2.1: Summary of proximity effect in the Kitaev chain junction. We show the presence ○ or absence × of the proximity effect, the oscillation, the zero-energy peak of the local density of states, and the quantization of the zero-bias conductance peak in each phase. △ indicates that there is no resonance due to the impurities, but the proximity effect occurs and the zero-energy peak exists. ◎ represents the strong resonance due to the impurities. [1]

	Odd-frequency spin-triplet even-parity		Even-frequency spin-triplet odd-parity		Zero-energy peak of the local density of states	Zero-bias conductance peak	
Phase	Penetration	Spatial oscillation	Penetration	Spatial oscillation		Quantization	Width
Topological	◎	×	○	×	○	○	wide
Topological near topological critical point	◎	○	○	×	○	○	narrow
Topological critical point	○	○	△	×	△	×	×
Non-topological	×	×	×	×	×	×	×

Table 2.2: Summary of the proximity effect in the s-wave superconductor junction. We show the presence ○ or absence × of the proximity effect, the oscillation, the zero-energy peak of the local density of states, and the zero-bias conductance peak in each phase. [1]

	Even-frequency spin-singlet even-parity		Zero-energy peak of the local density of states	Zero-bias conductance peak
Phase	Penetration	Spatial oscillation		
Metallic	○	×	×	×
Metallic near metal-insulator transition point	○	○	×	×
Metal-insulator transition point	○	○	×	×
Insulating	○	○	×	×

Our results about the proximity effect in the Kitaev chain and s-wave superconductor junction are summarized in Table 2.1 and Table 2.2, respectively.

2.6 Conclusion

In this chapter, we investigate the odd-frequency pair amplitude as a function of the site in the Kitaev chain systems. In the semi-infinite Kitaev chain, the odd-frequency pair amplitude being localized at the edge is suppressed at the topological critical point. We have shown that, unlike the case of the topological phase, the odd-frequency pair amplitude spatially spreads towards the bulk of the semi-infinite system at the topological critical point. Also, we have found that the normal Green's function being related to the zero-energy states is equal to the anomalous Green's function corresponding to the odd-frequency pair amplitude, numerically and analytically. Our results have confirmed that the Majorana fermion and the odd-frequency Cooper pairs have a one-to-one correspondence in the low-frequency limit.

Additionally, we discuss the proximity effect in the Kitaev chain attached to the diffusive normal metal. The odd-frequency pair amplitude being enhanced at the interface between the diffusive normal metal and Kitaev chain in the topological phase is reduced near the topological critical point. The odd-frequency spin-triplet even-parity pair amplitude behaves quite differently from the even-frequency spin-triplet odd-parity pair amplitude. The absence of the zero-energy states being generated by Majorana fermion reduces the odd-frequency pair amplitude at the topological critical point. The odd-frequency Cooper pairs, however, cause the proximity effect even at the topological critical point. Furthermore, the zero-energy peak of the local density of states and the zero-bias conductance peak of being quantized exist in the topological phase. The zero-energy peak of the local density of states becomes reduced and the zero-bias peak of the conductance is removed at the topological critical point.

We have examined the proximity effect in the Kitaev chain systems. Our work leads to research in more experimental systems including Rashba superconducting nanowire similar to the Kitaev chain.

2.7 Derivation of Majorana wave function

We describe the derivation [61] of the Majorana wave function used in Eq. (2.11), Sec. 2.4. The Majorana wave function in the semi-infinite Kitaev chain has been expressed, analyti-

cally [61]. The semi-infinite Kitaev chain is represented by the Hamiltonian:

$$\mathcal{H} = -t \sum_{j>0} \left(c_j^\dagger c_{j+1} + c_{j+1}^\dagger c_j \right) - \mu \sum_{j>0} \left(c_j^\dagger c_j - \frac{1}{2} \right) + \sum_{j>0} \left(\Delta c_j^\dagger c_{j+1}^\dagger + \text{H.c.} \right). \tag{2.15}$$

The Majorana operators

$$\hat{a}_j = c_j + c_j^\dagger, \quad \hat{b}_j = i(c_j^\dagger - c_j), \tag{2.16}$$

rewrite the Hamiltonian [Eq. (2.15)] as

$$\mathcal{H}_M = -\frac{i}{2} \sum_{j>0} \left[(t - \Delta)\, \hat{a}_j \hat{b}_{j+1} - (t + \Delta)\, \hat{b}_j \hat{a}_{j+1} \right] - \frac{i\mu}{2} \sum_{j>0} \hat{a}_j \hat{b}_j. \tag{2.17}$$

By using Heisenberg equation $[\hat{b}_j, \mathcal{H}] = 0$, we obtain the relation of Majorana wave function:

$$(t + \Delta)\, a_{j+1} + (t - \Delta)\, a_{j-1} + \mu a_j = 0, \tag{2.18}$$

with the Majorana wave function a_j instead of the Majorana operator $\hat{a}_j$. By applying Z-transform

$$\mathcal{Z}\left[a_j\right] \equiv \sum_{j=1}^{\infty} z^{-j} a_j, \tag{2.19}$$

$$\mathcal{Z}\left[a_{j+1}\right] = z\mathcal{Z}\left[a_j\right] - a_1, \tag{2.20}$$

$$\mathcal{Z}\left[a_{j-1}\right] = z^{-1}\mathcal{Z}\left[a_j\right], \tag{2.21}$$

to the relation Eq. (2.18),

$$\mathcal{Z}\left[a_j\right] = \frac{a_1 z^2}{z^2 + \frac{\mu}{t+\Delta} z + \frac{t-\Delta}{t+\Delta}}. \tag{2.22}$$

is obtained. The Majorana wave function

$$a_j = a_1 C^{j-1} \left\{ \cos\left[\beta(j-1)\right] + \frac{1}{\tan\beta} \sin\left[\beta(j-1)\right] \right\}, \tag{2.23}$$

with $\beta = \arctan(\sqrt{4t^2 - 4\Delta^2 - \mu^2}/\mu)$, $C = \sqrt{t-\Delta}/\sqrt{t+\Delta}$, and $\Delta \in (0, t)$, is derived by the inverse transformation to Eq. (2.22),

2.8 Numerical calculation

2.8.1 Recursive Green's function method

The recursive Green's function method [6] is useful for calculating the pair amplitude, the local density of states, and the differential conductance numerically faster in Secs. 2.4 and 2.5. The Green's function in a finite system is defined as follows: The definition of the Green's function in the N site system is written by

$$G = (zI - H)^{-1}, \tag{2.24}$$

with an identity matrix I, the Hamiltonian H, and the degree of freedom f ($f = 2$ for the Kitaev chain). Here, $z, H, G \in \mathbb{C}^{fN \times fN}$. In the Kitaev chain, $f = 2$ holds. Frequency z is classified as follows:

$$z = \begin{cases} i\omega_n & \text{(Matsubara Green's function)} \\ E - i\delta_\epsilon & \text{(advanced Green's function)} \\ E + i\delta_\epsilon & \text{(retarded Green's function)} \end{cases}, \tag{2.25}$$

with Matsubara frequency ω_n, energy E, and an infinitesimal positive number δ_ϵ. The Hamiltonian is represented by block matrices as

$$H = \begin{bmatrix} \check{u} & \check{t} & & & O \\ \check{t}^\dagger & \check{u} & \check{t} & & \\ & \check{t}^\dagger & \ddots & \ddots & \\ & & \ddots & \ddots & \check{t} \\ O & & & \check{t}^\dagger & \check{u} \end{bmatrix}, \tag{2.26}$$

with a zero matrix O and $\check{}$ standing for a 2×2 matrix. Also, we write the Green's function of the Hamiltonian [Eq. (2.26)] as follows: Similarly, the Green's function is written by

$$G = \begin{bmatrix} \check{G}^{(N)}_{1,1} & \check{G}^{(N)}_{1,2} & \cdots & G^{(N)}_{1,N} \\ \check{G}^{(N)}_{2,1} & \check{G}^{(N)}_{2,2} & & \vdots \\ \vdots & & \ddots & \vdots \\ \check{G}^{(N)}_{N,1} & \cdots & \cdots & \check{G}^{(N)}_{N,N} \end{bmatrix}, \tag{2.27}$$

where the superscript (N) of $\check{G}^{(N)}_{i,j}$ means the N site system.

$$\check{G}^{(i+1)}_{i+1,i+1} = \left(\check{z} - \check{u} - \check{t}^{\dagger} \check{G}^{(i)}_{i,i} \check{t} \right)^{-1}, \tag{2.28}$$

is the most basic relation in the recursive Green's function method. When the Eq. (2.28) is applied repeatedly and the initial value $\check{G}^{(1)}_{1,1} = (\check{z} - \check{u})^{-1}$ is used,

$$\check{G}^{(i+1)}_{1,1} = (\check{z} - \check{u} - \check{t} \check{G}^{(i)}_{1,1} \check{t}^{\dagger})^{-1} \tag{2.29}$$

holds.

We derive the relation in Eq. (2.28). We separate the Hamiltonian into four matrices as

$$H = \left[\begin{array}{c|c} H_A & H_B \\ \hline H_C & H_D \end{array}\right], \tag{2.30}$$

with

$$H_A = \begin{bmatrix} \check{u} & \check{t} & & & O \\ \check{t}^\dagger & \check{u} & \check{t} & & \\ & \check{t}^\dagger & \ddots & \ddots & \\ & & \ddots & \ddots & \check{t} \\ O & & & \check{t}^\dagger & \check{u} \end{bmatrix}, \tag{2.31}$$

$$H_B = \begin{bmatrix} \check{O} \\ \check{O} \\ \vdots \\ \check{t} \end{bmatrix}, \tag{2.32}$$

$$H_C = \begin{bmatrix} \check{O} & \check{O} & \cdots & \check{t}^\dagger \end{bmatrix}, \tag{2.33}$$

$$H_D = \begin{bmatrix} \check{u} \end{bmatrix}. \tag{2.34}$$

With the inverse matrix formula for the block matrix, the Green's function is transformed as

$$\begin{aligned} G &= (zI - H)^{-1} \\ &= \left[\begin{array}{c|c} zI_A - H_A & -H_B \\ \hline -H_C & zI_D - H_D \end{array}\right]^{-1}, \end{aligned} \tag{2.35}$$

with identity matrices I_A and I_D with the same size as H_A and H_D, respectively. The Green's

function can be specifically expressed as below:

$$
\begin{aligned}
G &= \left[\begin{array}{c|c} A & B \\ \hline C & D \end{array}\right]^{-1} \\
&= \left[\begin{array}{c|c} A^{-1} + A^{-1}BS^{-1}CA^{-1} & -A^{-1}BS^{-1} \\ \hline -S^{-1}CA^{-1} & S^{-1} \end{array}\right] \\
&= \left[\begin{array}{ccc|c} \check{G}^{(N)}_{1,1} & \check{G}^{(N)}_{1,2} & \cdots & \check{G}^{(N)}_{1,N} \\ \check{G}^{(N)}_{2,1} & \check{G}^{(N)}_{2,2} & & \vdots \\ \vdots & & \ddots & \vdots \\ \hline \check{G}^{(N)}_{N,1} & \cdots & \cdots & \check{G}^{(N)}_{N,N} \end{array}\right].
\end{aligned}
\tag{2.36}
$$

with $A = zI_A - H_A$, $B = -H_B$, $C = -H_C$, $D = zI_D - H_D$, and $S = D - CA^{-1}B$. Therefore, the recurrence relation Eq. (2.28) Thus, the recurrence relation in Eq. (2.28)

$$
\begin{aligned}
\check{G}^{(N)}_{N,N} &= \left(D - CA^{-1}B\right)^{-1} \\
&= \left(\check{z} - \check{u} - \check{t}^{\dagger}\check{G}^{(N-1)}_{N-1,N-1}\check{t}\right)^{-1}.
\end{aligned}
\tag{2.37}
$$

is derived.

We explain the connection between $\check{G}^{(N)}_{1,1}$ and $\check{G}^{(M)}_{M,M}$. The Green's function after the connection is represented by

$$
G = \begin{bmatrix} \ddots & & \\ & \check{G}^{(M+N)}_{M,M} & \check{G}^{(M+N)}_{M,M+1} \\ & \check{G}^{(M+N)}_{M+1,M} & \check{G}^{(M+N)}_{M+1,M+1} \\ & & \ddots \end{bmatrix}.
\tag{2.38}
$$

The Green's functions at the connected site are established as

$$\check{G}^{(M+N)}_{M,M} = \left[\left(\check{G}^{(M)}_{M,M}\right)^{-1} - \check{t}\check{G}^{(N)}_{1,1}\check{t}^{\dagger}\right]^{-1}, \tag{2.39}$$

$$\check{G}^{(M+N)}_{M+1,M+1} = \left[\left(\check{G}^{(N)}_{1,1}\right)^{-1} - \check{t}^{\dagger}\check{G}^{(M)}_{M,M}\check{t}\right]^{-1}, \tag{2.40}$$

$$\check{G}^{(M+N)}_{M,M+1} = \check{G}^{(M+N)}_{M,M}\check{t}\check{G}^{(N)}_{1,1}, \tag{2.41}$$

$$\check{G}^{(M+N)}_{M+1,M} = \check{G}^{(N)}_{1,1}\check{t}^{\dagger}\check{G}^{(M+N)}_{M,M}. \tag{2.42}$$

with a hopping matrix $\check{t}$ between connected sites.

We describe the Möbius transformation to calculate the Green's function in the semi-infinite system. We explain the left-hand Möbius transformation among the left-hand and right-hand Möbius transformations The left-hand transformation is defined as

$$\begin{bmatrix} A & B \\ C & D \end{bmatrix} \bullet Y \equiv (AY + B)(CY + D)^{-1}, \tag{2.43}$$

with $A, B, C, D, Y \in \mathbb{C}^{N\times N}$. For Möbius transformation, the relation

$$E \bullet \left(F \bullet Y\right) = (EF) \bullet Y, \tag{2.44}$$

with $E, F \in \mathbb{C}^{2N\times 2N}$ holds.

By using Möbius transformation, the relation Eq. (2.37) is arranged as below:

$$\begin{aligned}
\check{G}^{(N)}_{N,N} &= \left(\check{z} - \check{u} - \check{t}^{\dagger}\check{G}^{(N-1)}_{N-1,N-1}\check{t}\right)^{-1} \\
&= \check{t}^{-1}\left[(\check{z} - \check{u})\check{t}^{-1} - \check{t}^{\dagger}\check{G}^{(N-1)}_{N-1,N-1}\right]^{-1} \\
&= \begin{bmatrix} \check{O} & \check{t}^{-1} \\ -\check{t}^{\dagger} & (\check{z} - \check{u})\check{t}^{-1} \end{bmatrix} \bullet \check{G}^{(N-1)}_{N-1,N-1},
\end{aligned} \tag{2.45}$$

where we substitute $A = \check{O}$, $B = \check{t}^{-1}$, $C = -\check{t}^{\dagger}$, $D = (\check{z} - \check{u})\check{t}^{-1}$, and $Y = \check{G}^{(N-1)}_{N-1,N-1}$ in Eq. (2.43).

The left matrix of the Möbius transformation written in Eq. (2.45) is defined as

$$X = \begin{bmatrix} \check{O} & \check{t}^{-1} \\ -\check{t}^{\dagger} & (\check{z} - \check{u})\check{t}^{-1} \end{bmatrix}. \tag{2.46}$$

By using the Möbius transformation repeatedly in Eq. (2.45), $\check{G}^{(N)}_{N,N}$ follows

$$\begin{aligned} \check{G}^{(N)}_{N,N} &= X \bullet \check{G}^{(N-1)}_{N-1,N-1} \\ &= X \bullet (X \bullet \check{G}^{(N-2)}_{N-2,N-2}) \\ &\vdots \\ &= X^{N-1} \bullet \check{G}^{(1)}_{1,1}. \end{aligned} \tag{2.47}$$

The matrix X is diagonalized as

$$X = Q \begin{bmatrix} \check{\Lambda}_1 & \\ & \check{\Lambda}_2 \end{bmatrix} Q^{-1}, \tag{2.48}$$

$$\check{\Lambda}_1 = \begin{bmatrix} \lambda_1 & \\ & \lambda_2 \end{bmatrix}, \quad \check{\Lambda}_2 = \begin{bmatrix} \lambda_3 & \\ & \lambda_4 \end{bmatrix}, \tag{2.49}$$

with the eigenvalues λ_1, λ_2, λ_3, and λ_4 satisfying $|\lambda_1| < |\lambda_2| < |\lambda_3| < |\lambda_4|$. The infinitesimal imaginary number being added to energy eliminates the degeneracies of eigenvalues. With Eqs. (2.44), (2.47), and (2.48), $\check{G}^{(N)}_{N,N}$ is transformed as

$$\begin{aligned} \check{G}^{(N)}_{N,N} &= Q \begin{bmatrix} \check{\Lambda}_1^{N-1} & \\ & \check{\Lambda}_2^{N-1} \end{bmatrix} Q^{-1} \bullet \check{G}^{(1)}_{1,1} \\ &= Q \bullet \left\{ \begin{bmatrix} \check{\Lambda}_1^{N-1} & \\ & \check{\Lambda}_2^{N-1} \end{bmatrix} \bullet \left(Q^{-1} \bullet \check{G}^{(1)}_{1,1} \right) \right\}. \end{aligned} \tag{2.50}$$

By substituting $A = \check{\Lambda}_1^{N-1}$, $B = \check{O}$, $C = \check{O}$, $D = \check{\Lambda}_2^{N-1}$, and $Y = Q^{-1} \bullet \check{G}^{(1)}_{1,1}$ in Eq. (2.44), $\check{G}^{(N)}_{N,N}$

becomes

$$\check{G}^{(N)}_{N,N} = Q_{\bullet}\left[\check{\Lambda}_1^{N-1} Y \left(\check{\Lambda}_2^{N-1}\right)^{-1}\right]. \tag{2.51}$$

When we assume

$$Y = \begin{bmatrix} a & b \\ c & d \end{bmatrix}, \tag{2.52}$$

$$\begin{aligned} \lim_{N\to\infty} \check{\Lambda}_1^{N-1} Y \left(\check{\Lambda}_2^{N-1}\right)^{-1} &= \lim_{N\to\infty} \begin{bmatrix} \left(\frac{\lambda_1}{\lambda_2}\right)^{N-1} a & \left(\frac{\lambda_1}{\lambda_4}\right)^{N-1} b \\ \left(\frac{\lambda_2}{\lambda_3}\right)^{N-1} c & \left(\frac{\lambda_2}{\lambda_4}\right)^{N-1} d \end{bmatrix} \\ &= \check{O} \end{aligned} \tag{2.53}$$

is shown. In the infinite limit of the system size, the Green's function at the right edge of the semi-infinite system is obtained by

$$\begin{aligned} \check{G}^{\infty}_{L} &= Q_{\bullet}\check{O} \\ &= \check{Q}_{12}\check{Q}_{22}^{-1} \end{aligned} \tag{2.54}$$

from Eq. (2.51). We can obtain the Green's function $\check{G}^{\infty}_{R}$ at the left edge of the semi-infinite system by replacing t ($t^{\dagger}$) with $t^{\dagger}$ (t) in Eq. (2.46). The Green's function at the required site is calculated by using Eqs. 2.28, (2.29), (2.39)-(2.42).

2.8.2 Calculation of peak width

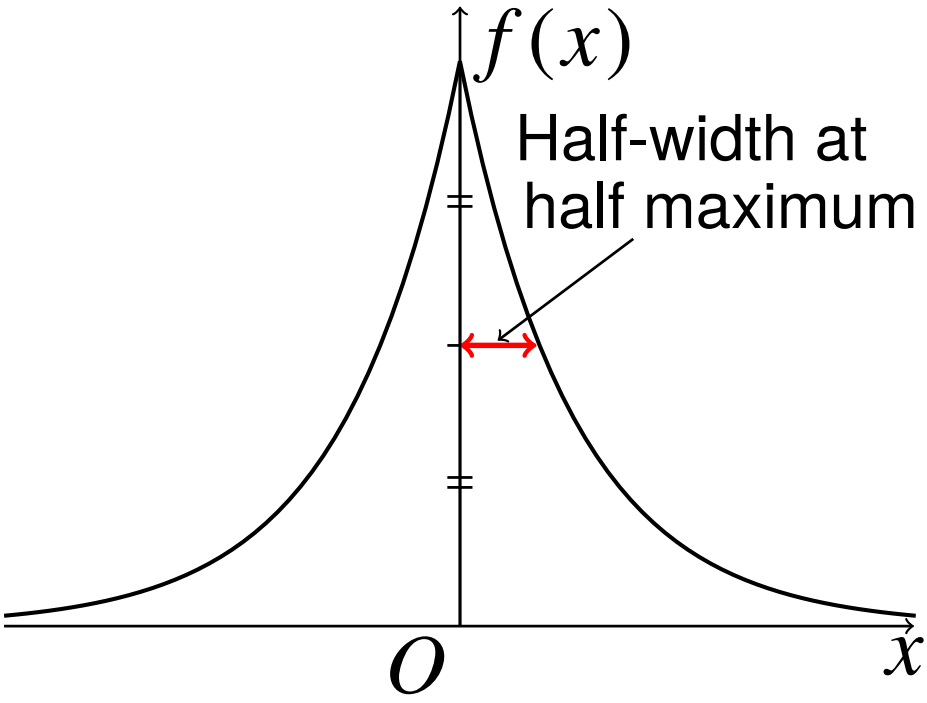

Figure 2.8: The peak width is defined by the half-width at half maximum. [1]

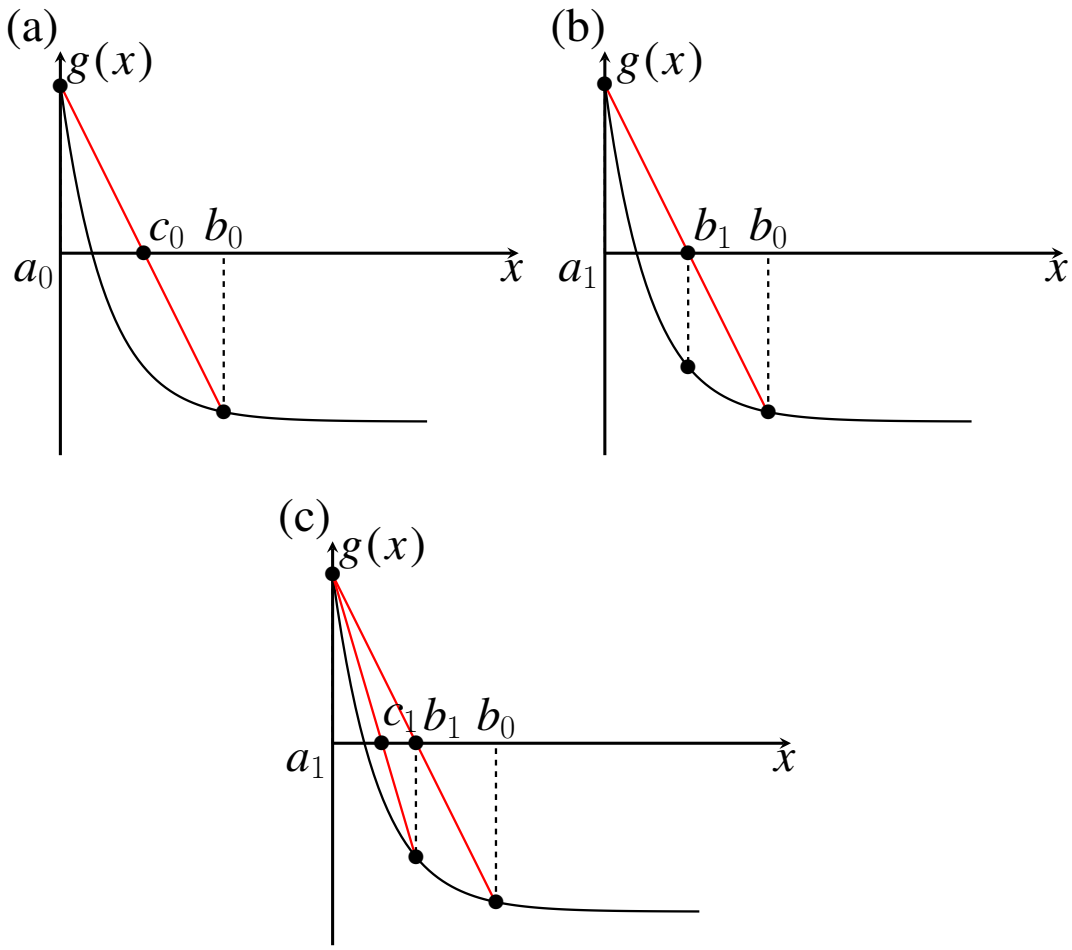

Figure 2.9: The method for obtaining the peak width by the false position method. [1]

We explain the method for obtaining the peak width being calculated in Fig. 2.7, Sec. 2.5. As shown in Fig. 2.8, the peak width is defined as half-width at half maximum. The recursive Green's function enables to get the output $f(x)$ from the input x:

$$x = \begin{cases} E/\Delta & \text{(for the local density of states)} \\ eV/\Delta & \text{(for conductance)} \end{cases}, \tag{2.55}$$

$$f(x) = \begin{cases} \rho(E, j)/N_0 & \text{(for the local density of states)} \\ G_{\mathrm{NS}}[e^2/h] & \text{(for conductance)} \end{cases}. \tag{2.56}$$

It is, however, difficult to calculate $f(x)$, analytically. Therefore, the half-width at half maximum is calculated, numerically. We search for the solution of

$$f(x) = \frac{1}{2} f(0). \tag{2.57}$$

This is equivalent to solving $g(x) = 0$ shown below:

$$g(x) \equiv f(x) - \frac{1}{2} f(0). \tag{2.58}$$

The half-width at half maximum is obtained by using the false position method Algorithm 1 and solving $g(x) = 0$.

Algorithm 1 False position method [1]

Initial value: a_0,b_0, Solution: $c \in [a_0, b_0]$
for $k = 0, 1, 2, \ldots$ **do**
    $c_k = \frac{a_k g(b_k) - b_k g(a_k)}{g(b_k) - g(a_k)}$;
    if $g(b_k)g(c_k) < 0$ **then**
        $a_{k+1} = c_k$;
        $b_{k+1} = b_k$;
    else
        $b_{k+1} = c_k$;
        $a_{k+1} = a_k$;
    end if
    if $|g(c_k)| < \delta$ **or** $|a_{k+1} - b_{k+1}| < \epsilon$ **then**
        break
        $c_k \to c$;
    end if
end for

We describe the false position method being depicted in Fig. 2.9. We first set the initial values a_0, b_0 where the solution of $g(x) = 0$ is contained in $[a_0, b_0]$. As shown in Fig. 2.9 (a), we define c_0 as the intersection of the line $(a_0, g(0))$–$(b_0, g(b_0))$ and the x-axis [Fig. 2.9(a)]. For $g(a_0)g(c_0) < 0$, we select $a_1 = a_0$ and $b_1 = c_0$ because one solution exists in in $[a_0, c_0]$ [Fig. 2.9 (b)]. For $g(c_0)g(b_0) < 0$, we select $a_1 = c_0$, $b_1 = b_0$ because one solution exists in $[c_0, b_0]$. As depicted in Fig. 2.9 (c), we next define the intersection of $(a_1, g(a_1))$ and $(b_1, g(b_1))$ as c_1 By repeating the above operation until the convergence condition is satisfied, the solution is obtained as the half-width of half maximum. Specifically, we select the parameters as $a_0 = 0$,

$b_0 = 1$, $\delta = 10^{-12}$, and $\epsilon = 10^{-14}$.

2.9 Analytical approach for Green's function

For $\Delta = t$, We derive the Green's function similarity [Eq. (2.10)]

$$-\mathrm{Im}\left[G_{1,1}\right] = \mathrm{Im}\left[\tilde{F}_{1,1}\right],$$

written in Sec. 2.4. We use the recurrence relation shown in Eq. (2.29)

$$\check{G}_{i+1}^{(i+1)} = \left(\check{z} - \check{u} - \check{t}\check{G}_i^{(i)}\check{t}^{\dagger}\right)^{-1}, \tag{2.59}$$

with

$$\check{z} = \begin{bmatrix} i\omega_n & 0 \\ 0 & i\omega_n \end{bmatrix}, \quad \check{u} = \begin{bmatrix} -\mu & 0 \\ 0 & \mu \end{bmatrix}, \tag{2.60}$$

$$\check{t} = \begin{bmatrix} -t & \Delta \\ -\Delta & t \end{bmatrix} = t \begin{bmatrix} -1 & 1 \\ -1 & 1 \end{bmatrix}. \tag{2.61}$$

We substitute $\check{G}_i$ and $\check{v}$ for $\check{G}_{1,1}^{(i)}$ and $\check{z} - \check{u}$, respectively. Because of the singularity of $\check{t}$, the matrix X in Eq. (2.46) cannot be diagonalized to obtain the Green's function at the edge of the semi-infinite system. The Green's function $\check{G}_{i+1}$ satisfying Eq. (2.59) is transformed as follows:

$$\begin{aligned} \check{G}_{i+1} &= \left(\check{v} - \check{t}\check{G}_i\check{t}^{\dagger}\right)^{-1} \\ &= \begin{bmatrix} v_{11} - g_i & -g_i \\ -g_i & v_{22} - g_i \end{bmatrix}^{-1} \\ &= \frac{1}{v_{11}v_{22} - (v_{11} + v_{22})g_i} \begin{bmatrix} v_{22} - g_i & g_i \\ g_i & v_{11} - g_i \end{bmatrix}, \end{aligned} \tag{2.62}$$

with g_i

$$g_i \equiv t^2 \left[\left(\check{G}_i \right)_{11} - \left(\check{G}_i \right)_{12} - \left(\check{G}_i \right)_{21} + \left(\check{G}_i \right)_{22} \right]. \tag{2.63}$$

g_{i+1} is expressed by v as follows:

$$\begin{aligned} \frac{g_{i+1}}{t^2} &= \frac{v_{11} + v_{22} - 4g_i}{v_{11}v_{22} - (v_{11} + v_{22})\, g_i} \\ &= \frac{1}{v_{11} + v_{22}} \left\{ 4 + \frac{(v_{11} - v_{22})^2}{v_{11}v_{22} - (v_{11} + v_{22})\, g_i} \right\}. \end{aligned} \tag{2.64}$$

We separate situations into $\mu = 0$ and $\mu \neq 0$.

Equation (2.64) is simplified for $\mu = 0$ as

$$g_i = g_\infty = \frac{2t^2}{i\omega_n}. \tag{2.65}$$

In the infinite limit of the system size, Eq. (2.62) satisfies

$$\begin{aligned} \check{G}_\infty &= \frac{1}{z_{11}z_{22} - (z_{11} + z_{22})\, g_\infty} \begin{bmatrix} z_{22} - g_\infty & g_\infty \\ g_\infty & z_{11} - g_\infty \end{bmatrix} \\ &= \frac{1}{i\omega_n(\omega_n^2 + 4t^2)} \begin{bmatrix} \omega_n^2 + 2t^2 & -2t^2 \\ -2t^2 & \omega_n^2 + 2t^2 \end{bmatrix} \end{aligned} \tag{2.66}$$

where $-\mathrm{Im}[(\check{G}_\infty)_{11}] \to \infty$ and $-\mathrm{Im}[(\check{G}_\infty)_{11}] \to \infty$ in the low frequency limit $\omega_n \to 0$. By focusing on Eq. (2.66), the relation of the Green's function is shown as

$$\begin{aligned} &\lim_{\omega_n \to 0} \left\{ \mathrm{Im}\left[G_{1,1} \right] + \mathrm{Im}\left[\tilde{F}_{1,1} \right] \right\} \\ &= \lim_{\omega_n \to 0} \left\{ \mathrm{Im}\left[\left(\check{G}_\infty \right)_{11} \right] + \mathrm{Im}\left[\left(\check{G}_\infty \right)_{21} \right] \right\} \\ &= \lim_{\omega_n \to 0} \frac{-\omega_n}{\omega_n^2 + 4t^2} \\ &= 0, \\ &\Leftrightarrow - \lim_{\omega_n \to 0} \left\{ \mathrm{Im}\left[G_{1,1} \right] \right\} = \lim_{\omega_n \to 0} \left\{ \mathrm{Im}\left[\tilde{F}_{1,1} \right] \right\}. \end{aligned} \tag{2.67}$$

For $\mu \neq 0$, denoting α and β as We redefine α and β for $\mu \neq 0$ as follows:

$$\begin{aligned}\alpha &= v_{11} + v_{22} \\ &= 2i\omega_n, \end{aligned} \tag{2.68}$$

$$\begin{aligned}\beta &= v_{11}v_{22} \\ &= -\omega_n^2 - \mu^2. \end{aligned} \tag{2.69}$$

In the infinite limit of the system size, g_∞ [Eq. (2.64)] is written by

$$\begin{aligned}\frac{g_\infty}{t^2} &= \frac{\alpha - 4g_\infty}{\beta - \alpha g_\infty}, \\ \Leftrightarrow g_\infty &= \frac{\beta + 4t^2 \pm \sqrt{\left(\beta + 4t^2\right)^2 - 4\alpha^2 t^2}}{2\alpha}. \end{aligned} \tag{2.70}$$

By using Eq. (2.62), $\check{G}_\infty$ is expressed by

$$\check{G}_\infty = \frac{1}{-\omega_n^2 - \mu^2 - \alpha g_\infty} \begin{bmatrix} i\omega_n - \mu - g_\infty & g_\infty \\ g_\infty & i\omega_n + \mu - g_\infty \end{bmatrix}. \tag{2.71}$$

By assuming the plus sign in Eq. (2.70) and using Eqs. 2.68–(2.70), two types of the Green's function $\lim_{\omega_n \to 0} \alpha g_\infty$ and $\lim_{\omega_n \to 0} \mathrm{Im}\left[g_\infty\right]$ are obtained as below:

$$\begin{aligned}\lim_{\omega_n \to 0} \alpha g_\infty &= \lim_{\omega_n \to 0} \frac{1}{2} \left\{ -\omega_n^2 - \mu^2 + 4t^2 + \sqrt{\left(-\omega_n^2 - \mu^2 + 4t^2\right)^2 + 16\omega_n^2 t^2} \right\} \\ &= \begin{cases} 0 & \text{(Non-topological)} \\ -\mu^2 + 4t^2 & \text{(Topological)} \end{cases}, \end{aligned} \tag{2.72}$$

$$\begin{aligned}\lim_{\omega_n \to 0} \mathrm{Im}\left[g_\infty\right] &= \lim_{\omega_n \to 0} -\frac{1}{4} \left[-\omega_n - \frac{\mu^2 - 4t^2}{\omega_n} + \sqrt{\left(-\omega_n - \frac{\mu^2 - 4t^2}{\omega_n} \right)^2 + 16t^2} \right] \\ &\simeq \lim_{\omega_n \to 0} \frac{1}{4} \left(\frac{\mu^2 - 4t^2}{\omega_n} - \frac{|\mu^2 - 4t^2|}{\omega_n} \right) \\ &= \begin{cases} 0 & \text{(Non-topological)} \\ -\infty & \text{(Topological)} \end{cases}. \end{aligned} \tag{2.73}$$

Equations 2.71–(2.73) provide

$$
\begin{aligned}
-\lim_{\omega_n\to 0}\mathrm{Im}\left[\left(\check{G}_\infty\right)_{11}\right] &= \lim_{\omega_n\to 0}\frac{\omega_n-\mathrm{Im}\left[g_\infty\right]}{\omega_n^2+\mu^2+\alpha g_\infty} \\
&= \begin{cases} 0 & \text{(Non-topological)} \\ \infty & \text{(Topological)} \end{cases}, \qquad (2.74)\\
\lim_{\omega_n\to 0}\mathrm{Im}\left[\left(\check{G}_\infty\right)_{21}\right] &= \lim_{\omega_n\to 0}\frac{\mathrm{Im}\left[g_\infty\right]}{-\omega_n^2-\mu^2-\alpha g_\infty} \\
&= \begin{cases} 0 & \text{(Non-topological)} \\ \infty & \text{(Topological)} \end{cases}. \qquad (2.75)
\end{aligned}
$$

The fact, that the Majorana fermion exists in the topological phase and does not appear in the non-topological phase, corresponds to Eq. (2.74). Similarly, we next assume the minus sign in Eq. (2.70). Then, we obtain

$$
\begin{aligned}
-\lim_{\omega_n\to 0}\mathrm{Im}\left[\left(\check{G}_\infty\right)_{11}\right] &= \begin{cases} \infty & \text{(Non-topological)} \\ 0 & \text{(Topological)} \end{cases}, \qquad (2.76)\\
\lim_{\omega_n\to 0}\mathrm{Im}\left[\left(\check{G}_\infty\right)_{21}\right] &= \begin{cases} \infty & \text{(Non-topological)} \\ 0 & \text{(Topological)} \end{cases}. \qquad (2.77)
\end{aligned}
$$

The fact, that the Majorana fermion exists in the topological phase, conflicts with Eq. (2.76). Therefore, it is correct to choose the plus sign in Eq. (2.70). With Eqs. 2.72, (2.74), and (2.75), the similarity of the Green's function is proved as

$$
\begin{aligned}
&\lim_{\omega_n\to 0}\left\{\mathrm{Im}\left[G_{1,1}\right]+\mathrm{Im}\left[\tilde{F}_{1,1}\right]\right\} \\
&\quad= \lim_{\omega_n\to 0}\left\{\mathrm{Im}\left[\left(\check{G}_\infty\right)_{11}\right]+\mathrm{Im}\left[\left(\check{G}_\infty\right)_{21}\right]\right\} \\
&\quad= \lim_{\omega_n\to 0}\begin{cases} \frac{-\omega_n}{\omega_n^2+\mu^2} & \text{(Non-topological)} \\ \frac{-\omega_n}{\omega_n^2+4t^2} & \text{(Topological)} \end{cases} \\
&\quad= 0, \qquad (2.78)\\
&\Leftrightarrow -\lim_{\omega_n\to 0}\left\{\mathrm{Im}\left[G_{1,1}\right]\right\} = \lim_{\omega_n\to 0}\left\{\mathrm{Im}\left[\tilde{F}_{1,1}\right]\right\}. \qquad (2.79)
\end{aligned}
$$

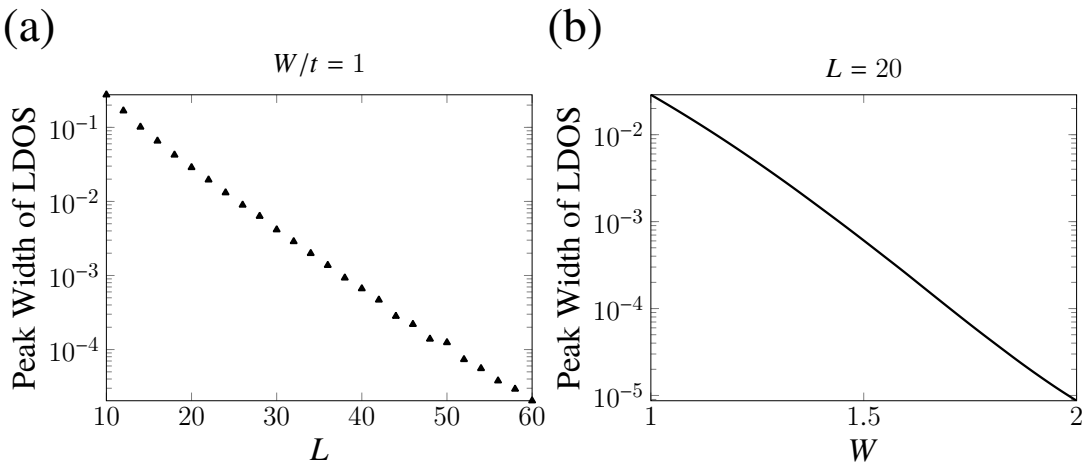

Figure 2.10: The peak width of the local density of states at zero energy for (a) the length of the diffusive normal metal L and (b) the strength of the impurities W in the normal metal/diffusive normal metal/Kitaev chain junction. $\mu_{\mathrm{N}} = \mu = 0$, $\Delta/t = 0.1$, $\delta_\epsilon/t = 10^{-8}$, $j = L/2$, (a) $W = 1$, and (b) $L = 20$. [1]

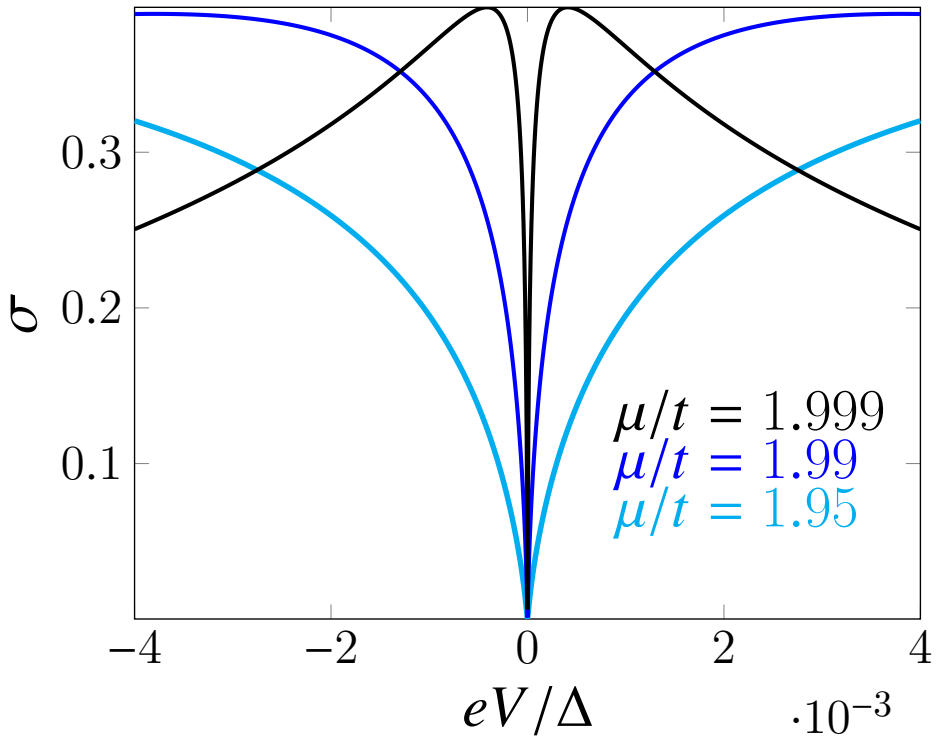

Figure 2.11: Standard deviation σ of differential conductance for the bias voltage eV in the normal metal/diffusive normal metal/Kitaev chain junction. $\Delta/t = 0.1$, $\mu_{\mathrm{N}}/t = 0.5$, $W/t = 1$, $j = -10$, and $\delta_\epsilon/t = 10^{-8}$. We focus on the topological phase for $\mu = 1.99, 1.95, 1.999$. [1]

2.10 differential conductance in a Kitaev chain junction

In this section, we investigate the effect of the impurities on the local density of states and the differential conductance in the normal metal/diffusive normal metal/Kitaev chain junction shown in Sec. 2.5. Similar to the peak width of the conductance, we plot the half-width at half maximum of the local density of states as a function of the length of the diffusive normal metal L and the strength of the impurities W in Figs. 2.10 (a)–2.10 (b). As a result, we find the following behavior of the peak width of the local density of states $\propto \exp(c_1 L + c_2 W)$ with $c_1 < 0$ and $c_2 < 0$.

To show the robustness of the zero-bias conductance, we plot the standard deviation of differential conductance $G_{\rm NS}$ being defined by

$$\sigma = \sqrt{\frac{1}{r_{\rm max}} \sum_{l=1}^{r_{\rm max}} \left[G_{\rm NS}^{(l)} - G_{\rm NS}^{(\rm avg.)} \right]^2}, \tag{2.80}$$

with the differential conductance $G_{\rm NS}^{l}$ being calculated for the lth time and the average conductance $G_{\rm NS}^{(\rm avg.)}$ being calculated by different impurities. For $\mu = 1.95$, 1.99, and 1.999, the standard deviation of the conductance is plotted in Fig. 2.11. There is almost no variation in the conductance at zero-bias voltage. The result shows that the proximity of the zero-energy states is robust against impurities [64]. Thus, we support the robustness of the zero-bias conductance against impurities, numerically.

Chapter 3

Odd-frequency Cooper pairs in a p-wave superconductor with multiple Majorana fermions

3.1 Introduction

The number of Majorana fermions, corresponding to the winding number, that can exist at each edge of the Kitaev chain is one. Considering higher-order hopping and magnetic fields in a p-wave superconductor with spin degrees of freedom allows us to access topological phases with multiple Majorana fermions [8, 65]. There is a one-to-one correspondence between the Majorana fermions and the odd-frequency Cooper pairs [66, 3, 4, 1]. Specifically, in the low-frequency limit, the amplitude of the normal Green's function (corresponding to the Majorana fermions) is equal to that of the anomalous Green's function (the odd-frequency pair amplitude) [3, 4, 1]. The odd-frequency pair amplitude, accompanying the Majorana fermions, has a $1/\omega$ dependence, where ω is frequency [4]. In addition, the sum of the odd-frequency pair amplitude is related to the winding number that is extended to a finite frequency in a limited semi-infinite system with chiral symmetry: spectral bulk-boundary correspondence [4, 67].

This chapter is based on arxiv:2112.01009 (2021) [7]

This chapter aims to distinguish the number of Majorana fermions in terms of the odd-frequency Cooper pairs and to elucidate the spatial dependence and spin structure of the odd-frequency pair amplitude, in the p-wave superconductor with the multiple Majorana fermions. In the semi-infinite system with the multiple Majorana fermions, it is not easy to distinguish the topological phases with the different topological numbers (winding number) by focusing on the local density of states at the edge. This is because these Majorana fermions appear as the same zero-energy states. Therefore, we have concentrated on the odd-frequency Coper pairs that have been useful for understanding the topological properties and transport phenomena of the Kitaev chain [1, 68].

First, we investigate the system size dependence of the odd-frequency pair amplitude with and without magnetic fields that break chiral symmetry. The system size dependence provides three pieces of information: the parity of the number of the Majorana fermions at the edge, the number of low-energy modes corresponding to the Majorana fermions with different localization lengths, and the fingerprints of the Majorana fermions. Also, we present the spatial dependence of the odd-frequency $\mathbf{f}$ vector representing odd-frequency pair amplitude and the spin structure of odd-frequency Cooper pairs. Here, the vector is defined by imitating the $\mathbf{d}$ vector that characterizes spin-triplet superconductivity. We find the following two results. The vector is fixed in the same direction in any topological phase. The spin direction of odd-frequency Cooper pairs tends to point toward the direction of the magnetic fields. Our findings show that odd-frequency Cooper pairs can be an indicator for the detection of multiple Majorana fermions and the distinction among topological phases.

This chapter is organized as follows. In Sec. 3.2, we introduce the model of a p-wave superconductor with multiple Majorana fermions. In Sec. 3.3, we explain how to calculate odd-frequency pair amplitude from Green's function. Then, we provide the system size dependence of low energy mode corresponding Majorana fermions and odd-frequency pair amplitude in Sec. 3.4. In addition, we present the spatial dependence of the odd-frequency $\mathbf{f}$ vector representing odd-frequency pair amplitude and the spin structure of odd-frequency Cooper pairs in Sec. 3.5. In Sec. 3.6, we discuss a model for detecting evidence of the multiple Majorana fermions. Finally, We conclude our work in Sec. 3.7.

3.2 A p-wave superconductor with multiple Majorana fermions

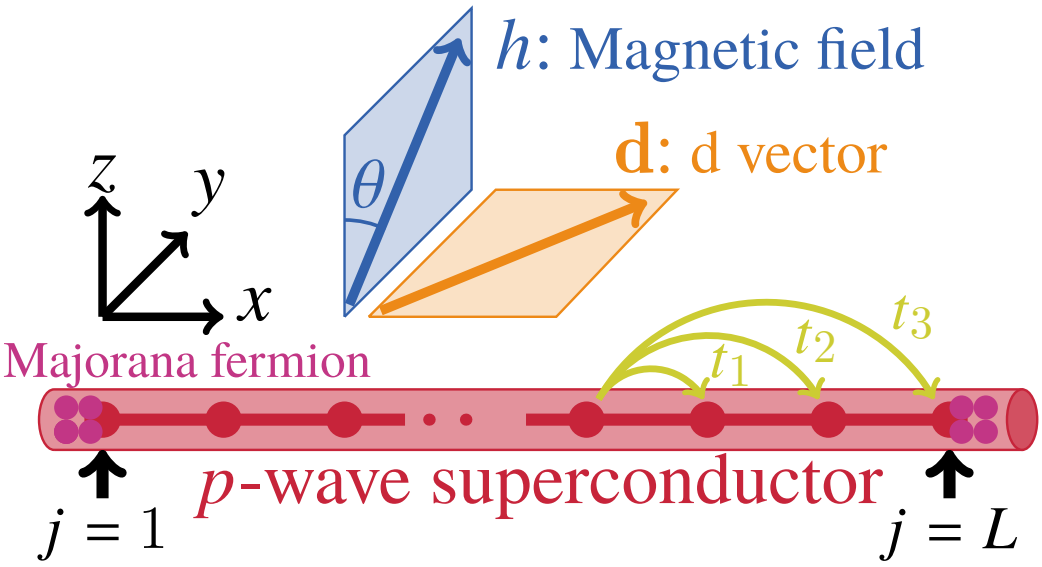

Figure 3.1: A Sketch of a p-wave superconductor (red tube) with magnetic fields. The superconductor lies in x direction. The magnetic fields (d vector) are applied in the y-z (x-y) plane. Hopping is considered up to the third nearest neighbor sites: (t_1, t_2, t_3). j: site, L: the number of sites in the system. [7]

As the model for investigating the multiple Majorana phases, we introduce a p-wave superconductor with magnetic fields [8] shown in Fig. 3.1.

The Hamiltonian of the system on the lattice is written as

$$\mathcal{H} = \mathcal{H}_{\mathrm{N}} + \mathcal{H}_{\mathbf{h}} + \mathcal{H}_{\mathrm{S}}, \tag{3.1}$$

$$\begin{aligned}
\mathcal{H}_{\mathrm{N}} &= -\mu \sum_{j,\sigma} \left(c^{\dagger}_{j,\sigma} c_{j,\sigma} \right) - \sum_{j,\sigma,\nu} t_{\nu} \left(c^{\dagger}_{j,\sigma} c_{j+\nu,\sigma} + c^{\dagger}_{j+\nu,\sigma} c_{j,\sigma} \right), \\
\mathcal{H}_{\mathbf{h}} &= - \sum_{j,\sigma,\sigma'} (\mathbf{h} \cdot \boldsymbol{\sigma})_{\sigma,\sigma'} c^{\dagger}_{j,\sigma} c_{j,\sigma'}, \\
\mathcal{H}_{\mathrm{S}} &= \sum_{j,\sigma} \left[\Delta_{\sigma\sigma} c^{\dagger}_{j,\sigma} c^{\dagger}_{j+1,\sigma} + \mathrm{H.c.} \right].
\end{aligned} \tag{3.2}$$

where $c_{j,\sigma}$, μ, t_{ν}, $\mathbf{h} = (h_x, h_y, h_z) = (0, h\sin\theta, h\cos\theta)$, and $\Delta_{\sigma,\sigma}$ ($\in \mathbb{R}$, assume spin-polarized case: the component $d_z = 0$ of $\mathbf{d}$ vector) denote the annihilation operator with a spin σ at a site $j \in [1, L]$, chemical potential, the ν-th ($\nu = 1, 2, 3$) nearest-neighbor hopping, Zeeman

potential, and pair potential, respectively [8]. H.c. means Hermitian conjugate and $\boldsymbol{\sigma}$ are Pauli matrices.

The Hamiltonian of the system with L sites can be expressed in the block matrix form as

$$H = \begin{bmatrix} \hat{u} & \hat{t}_1 & \hat{t}_2 & \hat{t}_3 & O & \cdots \\ \hat{t}_1^\dagger & \hat{u} & \hat{t}_1 & \hat{t}_2 & \hat{t}_3 & \\ \hat{t}_2^\dagger & \hat{t}_1^\dagger & \hat{u} & \hat{t}_1 & \hat{t}_2 & \\ \hat{t}_3^\dagger & \hat{t}_2^\dagger & \hat{t}_1^\dagger & \hat{u} & \hat{t}_1 & \\ O & \hat{t}_3^\dagger & \hat{t}_2^\dagger & \hat{t}_1^\dagger & \hat{u} & \\ \vdots & & & & & \ddots \end{bmatrix}, \tag{3.3}$$

where $\mathcal{H} = (1/2)[C_1^\dagger, C_2^\dagger, \ldots, C_L^\dagger]H[C_1, C_2, \ldots, C_L]^\mathsf{T} - \mu L$ with $C_j = [c_{j\uparrow}, c_{j\downarrow}, c_{j\uparrow}^\dagger, c_{j\downarrow}^\dagger]$,

$$\hat{u} = \begin{bmatrix} -\mu - h_z & ih_y & 0 & 0 \\ -ih_y & -\mu + h_z & 0 & 0 \\ 0 & 0 & \mu + h_z & ih_y \\ 0 & 0 & -ih_y & \mu - h_z \end{bmatrix},$$

$$\hat{t}_1 = \begin{bmatrix} -t_1 & 0 & \Delta_{\uparrow\uparrow} & 0 \\ 0 & -t_1 & 0 & \Delta_{\downarrow\downarrow} \\ -\Delta_{\uparrow\uparrow} & 0 & t_1 & 0 \\ 0 & -\Delta_{\downarrow\downarrow} & 0 & t_1 \end{bmatrix},$$

$$\hat{t}_2 = \begin{bmatrix} -t_2 & 0 & 0 & 0 \\ 0 & -t_2 & 0 & 0 \\ 0 & 0 & t_2 & 0 \\ 0 & 0 & 0 & t_2 \end{bmatrix}, \quad \hat{t}_3 = \begin{bmatrix} -t_3 & 0 & 0 & 0 \\ 0 & -t_3 & 0 & 0 \\ 0 & 0 & t_3 & 0 \\ 0 & 0 & 0 & t_3 \end{bmatrix}. \tag{3.4}$$

By applying Fourier transformation to Eq. (3.1), we get the Hamiltonian in **k** space as

$$\mathcal{H}(k) = \sum_{k,\sigma} \varepsilon(k) c^{\dagger}_{k,\sigma} c_{k,\sigma} - \sum_{k,\sigma,\sigma'} (\mathbf{h}\cdot\boldsymbol{\sigma})_{\sigma,\sigma'} c^{\dagger}_{k,\sigma} c_{k,\sigma'} + \sum_{k,\sigma} [i\Delta_{\sigma\sigma} \sin k c^{\dagger}_{k,\sigma} c^{\dagger}_{-k,\sigma} + \text{H.c.}], \tag{3.5}$$

where k is the wavenumber and $\varepsilon(k) = -\mu - 2t_1 \cos k - 2t_2 \cos 2k - 2t_3 \cos 3k$. Equation (3.5) is rewritten in matrix representation:

$$H(k) = \begin{bmatrix} \varepsilon(k) - h_z & ih_y & 2i\Delta_{\uparrow\uparrow} \sin k & 0 \\ -ih_y & \varepsilon(k) + h_z & 0 & 2i\Delta_{\downarrow\downarrow} \sin k \\ -2i\Delta_{\uparrow\uparrow} \sin k & 0 & -\varepsilon(k) + h_z & ih_y \\ 0 & -2i\Delta_{\downarrow\downarrow} \sin k & -ih_y & -\varepsilon(k) - h_z \end{bmatrix}, \tag{3.6}$$

where $\mathcal{H}(k) = (1/2) \sum_k C^{\dagger}_k H(k) C_k + \text{const.}$ with the base $C_k = [c_{k,\uparrow}, c_{k,\downarrow}, c^{\dagger}_{-k,\uparrow}, c^{\dagger}_{-k,\downarrow}]^{\mathsf{T}}$.

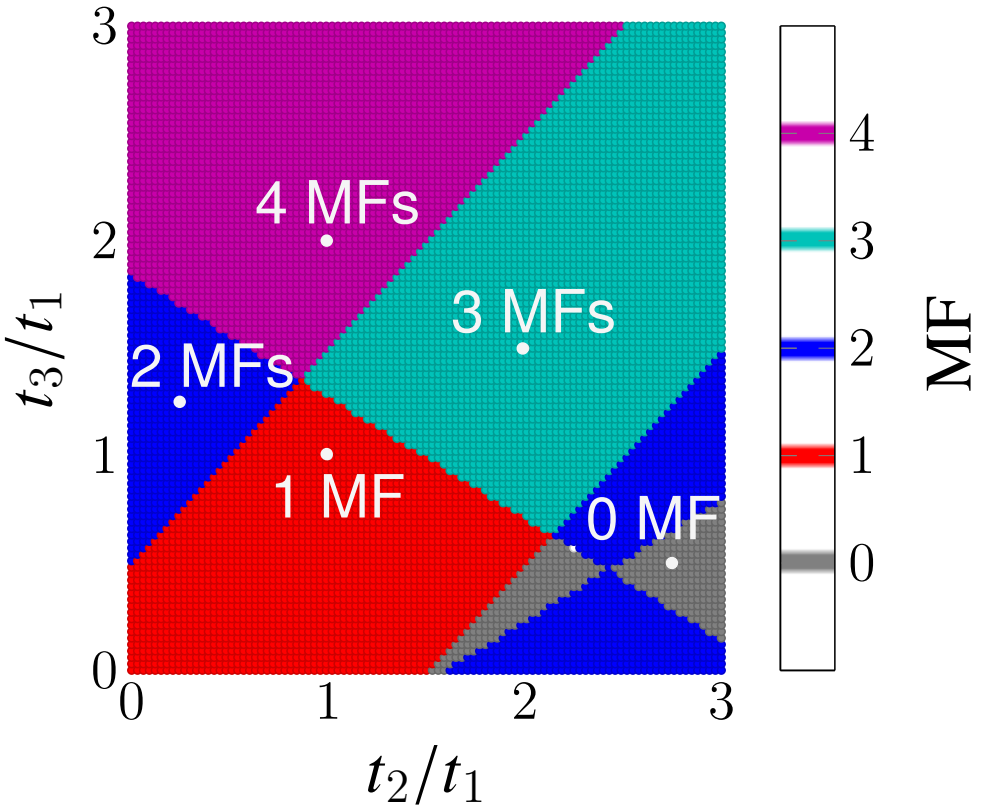

Figure 3.2: A topological phase diagram in the p-wave superconductor with the magnetic fields as a function of t_2 and t_3: $\Delta_{\uparrow\uparrow} = 0.18t_1$, $\Delta_{\downarrow\downarrow} = 1.8t_1$. The topological phases with the multiple Majorana fermions (MFs) ($w > 2$) are available for $t_2, t_3 > t_1$. Parameters: $\theta = \pi/4$, $h/t_1 = 2$, $\mu/t_1 = 1$. [7]

The winding number, telling us the number of the Majorana fermions at the edge of the system, is calculated from the Hamiltonian in **k** space shown in Eq. (3.6):

$$w = \frac{-1}{4\pi i}\int_{-\pi}^{\pi} \mathrm{Tr}\left[\Gamma H^{-1}(k)\partial_k H(k)\right] \mathrm{d}k$$
$$= \begin{cases} 0 & \text{(trivial)} \\ 1, 2, 3, 4 & \text{(topological)}. \end{cases} \tag{3.7}$$

$\Gamma = \tau_x\sigma_z$, defined for $h_x = 0$, means the chiral operator satisfying $\{\Gamma, H(k)\} = 0$. In this system, the topological phase with $w > 2$ can be achieved by controlling the parameters [8] as shown in Fig. 3.2. The **d** vector ($\mathbf{d} = [(\Delta_{\downarrow\downarrow} - \Delta_{\uparrow\uparrow})/2, (\Delta_{\uparrow\uparrow} + \Delta_{\downarrow\downarrow})/2, \Delta_{\uparrow\downarrow}]$), characterizing the spin-triplet pairing, having more than one component and long-distance hoppings (t_2 and t_3) are necessary

conditions to get 3 and 4 MF (Majorana fermion) phases.

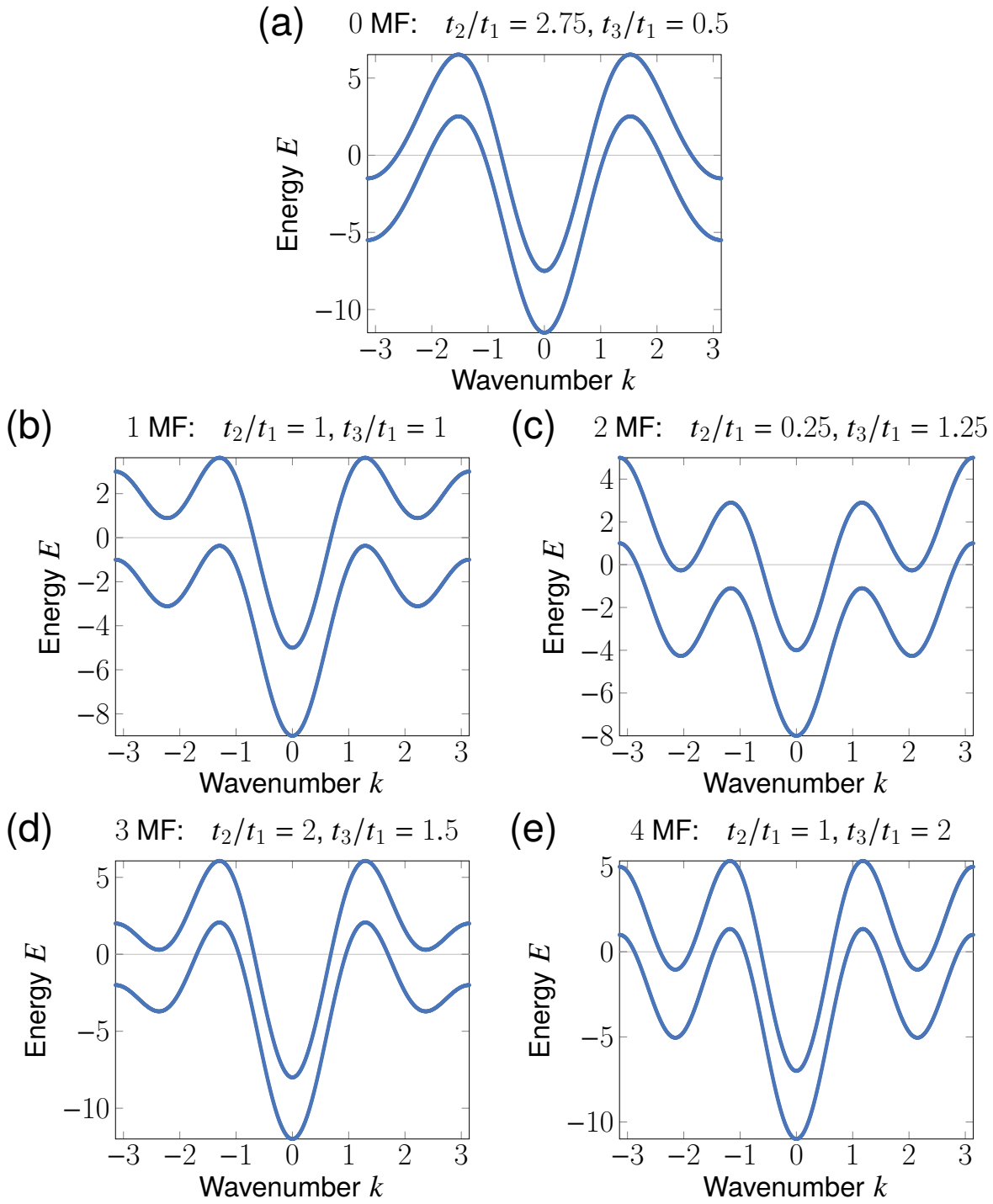

Figure 3.3: (a)–(e) Energy bands of normal states ($\Delta_{\uparrow\uparrow} = \Delta_{\downarrow\downarrow} = 0$) in $\mathbf{k}$ space. (a) 0 MF, (b) 1 MF, (c) 2 MF, (d) 3 MF, (e) 4 MF phases, where MF means the Majorana fermion. Parameters: $\theta = \pi/4$, $h/t_1 = 2$, $\mu/t_1 = 1$. [7]

The importance of long-distance hopping can be understood from the energy dispersion of the normal states in k space. The energy dispersion, shown in Fig. 3.3(a)–3.3(e), is calculated

as $E = \varepsilon(k) \pm h$ by the diagonalization of the upper left 2×2 block matrix in Hamiltonian [Eq. (3.6)]. The number of Fermi points (intersections of energy bands and $E = 0$) is more in the 2, 3, and 4 MF phases [Figs. 3.3(c)–3.3(e)] than in the 1 MF phase [Fig. 3.3(b)], with the exception in the 0 MF phase [Fig. 3.3(a)]. To have several Fermi points, $\varepsilon(k)$ needs to contain high-frequency components such as $\cos 2k$ and $\cos 3k$. Higher-order hoppings t_2 and t_3 are a prerequisite for accessing the 3 MF and 4 MF phases in this system [In the strict sense, higher-order hopping promotes the sign changes in the real and imaginary parts of Eq. (3.21)].

3.3 Calculation of pair amplitude by Green's function

To relate the multiple Majorana fermions and the odd-frequency Cooper pairs, we calculate the ground state energy corresponding to Majorana fermion and the odd-frequency pair amplitude. The ground state energy can be obtained from the diagonalization of the Hamiltonian in the real space H in Eq. (3.3). The odd-frequency pair amplitude is calculated from the Matsubara Green's function. For the large system, we use the recursive Green's function method [6] to calculate the Green's function at the required site numerically.

The Green's function at the site j, j' is defined as

$$\begin{aligned} \hat{G}(i\omega, j, j') &= \left\{ [i\omega I - H]^{-1} \right\}_{j,j'} \\ &= \begin{bmatrix} G_{j,j'}(i\omega) & F_{j,j'}(i\omega) \\ \tilde{F}_{j,j'}(i\omega) & \tilde{G}_{j,j'}(i\omega) \end{bmatrix} \end{aligned} \tag{3.8}$$

where I represents an identity matrix. $G(\tilde{G})[F(\tilde{F})]$ means the normal Green's function in the electron-electron (hole-hole) space [the anomalous Green's function in the electron-hole (hole-electron) space] with the 4×4 sizes, and ω is Matsubara frequency. Each local Green's function can be decomposed into spin components $\uparrow$ and $\downarrow$. For example, the anomalous Green's function is expressed as

$$F_{j,j'} = \begin{bmatrix} F_{j,j',\uparrow,\uparrow} & F_{j,j',\uparrow,\downarrow} \\ F_{j,j',\downarrow,\uparrow} & F_{j,j',\downarrow,\downarrow} \end{bmatrix}, \tag{3.9}$$

and G, $\tilde{G}$, and $\tilde{F}$ are described, similarly.

The Matsubara Green's function shown in Eq. (3.8) gives the odd- (even-) frequency spin-triplet s-wave (p-wave) pair amplitude:

$$\begin{aligned}\mathbf{f^{o(e)}} &= [f_x^{\mathrm{o(e)}}, f_y^{\mathrm{o(e)}}, f_z^{\mathrm{o(e)}}] \\ &= \left[\frac{f_{\downarrow\downarrow}^{\mathrm{o(e)}} - f_{\uparrow\uparrow}^{\mathrm{o(e)}}}{2}, \frac{f_{\uparrow\uparrow}^{\mathrm{o(e)}} + f_{\downarrow\downarrow}^{\mathrm{o(e)}}}{2i}, f_{\uparrow\downarrow}^{\mathrm{o(e)}}\right],\end{aligned} \tag{3.10}$$

$$f_{\sigma\sigma'}^{\mathrm{o}}(j) = \frac{1}{2}\left[F_{j,j,\sigma,\sigma'}(i\omega) - F_{j,j,\sigma,\sigma'}(-i\omega)\right], \tag{3.11}$$

$$\begin{aligned}f_{\sigma\sigma'}^{\mathrm{e}}(j) = \frac{1}{2}\Bigg[&\frac{F_{j,j+1,\sigma,\sigma'}(i\omega) - F_{j+1,j,\sigma,\sigma'}(i\omega)}{2} \\ &+\frac{F_{j,j+1,\sigma,\sigma'}(-i\omega) - F_{j+1,j,\sigma,\sigma'}(-i\omega)}{2}\Bigg].\end{aligned} \tag{3.12}$$

where the superscript $^{\mathrm{o}}$ and $^{\mathrm{e}}$ stand for the "odd" and "even" frequencies, respectively. Note that we only focus on the odd- (even-) frequency spin-triplet s-wave (p-wave) pair amplitude although there are Cooper pairs with other symmetries. Here, we define the odd- and even-frequency pair amplitude as the vector form $\mathbf{f^{o(e)}}$ to discuss the spin state of these Cooper pairs.

To get the Matsubara Green's function in the large finite system efficiently, we use the recurrence relation of the recursive Green's function method [6]. The recurrence relation

increasing sites to the "right" in the recursive Green's function is given by

$$g_{\mathrm{L}}^{(n)} = (\Xi_{\mathrm{L}})^n \bullet g_{\mathrm{L}}^{(0)}, \tag{3.13}$$

$$\Xi_{\mathrm{L}} = \begin{bmatrix} a_{\mathrm{L}} & b_{\mathrm{L}} \\ c_{\mathrm{L}} & d_{\mathrm{L}} \end{bmatrix}, \quad g_{\mathrm{L}}^{(n)} = \begin{bmatrix} G_{n-2,n-2}^{(n)} & G_{n-2,n-1}^{(n)} & G_{n-2,n}^{(n)} \\ G_{n-1,n-2}^{(n)} & G_{n-1,n-1}^{(n)} & G_{n-1,n}^{(n)} \\ G_{n,n-2}^{(n)} & G_{n,n-1}^{(n)} & G_{n,n}^{(n)} \end{bmatrix},$$

$$a_{\mathrm{L}} = \begin{bmatrix} O & \hat{I} & O \\ O & O & \hat{I} \\ O & O & O \end{bmatrix}, \quad b_{\mathrm{L}} = \begin{bmatrix} O & O & O \\ O & O & O \\ \hat{t}_3^{-1} & O & O \end{bmatrix},$$

$$c_{\mathrm{L}} = \begin{bmatrix} O & O & O \\ O & O & O \\ -\hat{t}_3^{\dagger} & -\hat{t}_2^{\dagger} & -\hat{t}_1^{\dagger} \end{bmatrix}, \quad d_{\mathrm{L}} = \begin{bmatrix} -\hat{t}_2\hat{t}_3^{-1} & \hat{I} & O \\ -\hat{t}_1\hat{t}_3^{-1} & O & \hat{I} \\ (i\omega - u)\hat{t}_3^{-1} & O & O \end{bmatrix}, \tag{3.14}$$

where $G_{j,j'}^{(n)}$ means the local Green's function at the j,j' site in the system with n sites. The operator $\bullet$ represents the left-hand Möbius transformation defined as

$$\begin{bmatrix} A & B \\ C & D \end{bmatrix} \bullet Y \equiv (AY + B)(CY + D)^{-1} \tag{3.15}$$

with the square matrix A, B, C, D, and Y with the same size as each other. Similarly, the

recurrence relation increasing sites to the "left" is obtained by

$$g_{\mathrm{R}}^{(n)} = (\Xi_{\mathrm{R}})^n \bullet g_{\mathrm{R}}^{(0)}, \tag{3.16}$$

$$\Xi_{\mathrm{R}} = \begin{bmatrix} a_{\mathrm{R}} & b_{\mathrm{R}} \\ c_{\mathrm{R}} & d_{\mathrm{R}} \end{bmatrix}, \quad g_{\mathrm{R}}^{(n)} = \begin{bmatrix} G_{1,1}^{(n)} & G_{1,2}^{(n)} & G_{1,3}^{(n)} \\ G_{2,1}^{(n)} & G_{2,2}^{(n)} & G_{2,3}^{(n)} \\ G_{3,1}^{(n)} & G_{3,2}^{(n)} & G_{3,3}^{(n)} \end{bmatrix},$$

$$a_{\mathrm{R}} = \begin{bmatrix} 0 & 0 & 0 \\ \hat{I} & 0 & 0 \\ 0 & \hat{I} & 0 \end{bmatrix}, \quad b_{\mathrm{R}} = \begin{bmatrix} 0 & 0 & \hat{t}_3^{\dagger -1} \\ 0 & 0 & 0 \\ 0 & 0 & 0 \end{bmatrix},$$

$$c_{\mathrm{R}} = \begin{bmatrix} -\hat{t}_1 & -\hat{t}_2 & -\hat{t}_3 \\ 0 & 0 & 0 \\ 0 & 0 & 0 \end{bmatrix}, \quad d_{\mathrm{R}} = \begin{bmatrix} 0 & 0 & (i\omega - u)\hat{t}_3^{\dagger -1} \\ \hat{I} & 0 & -\hat{t}_1^{\dagger}\hat{t}_3^{\dagger -1} \\ 0 & \hat{I} & -\hat{t}_2^{\dagger}\hat{t}_3^{\dagger -1} \end{bmatrix}. \tag{3.17}$$

The local Green's function after connecting $g_{\mathrm{L}}^{(m)}$ and $g_{\mathrm{R}}^{(n)}$ is written as follows:

$$\left[g_{\mathrm{M}}^{(m+n)} \right]_{11} = \begin{bmatrix} G_{m-2,m-2}^{(m+n)} & G_{m-2,m-1}^{(m+n)} & G_{m-2,m}^{(m+n)} \\ G_{m-1,m-2}^{(m+n)} & G_{m-1,m-1}^{(m+n)} & G_{m-1,m}^{(m+n)} \\ G_{m,m-2}^{(m+n)} & G_{m,m-1}^{(m+n)} & G_{m,m}^{(m+n)} \end{bmatrix}. \tag{3.18}$$

We can get the local Green's function at the required site in the finite system by combining Eqs. (3.13)(3.16), and (3.18).

3.4 Low energy states and odd-frequency pair amplitude

In this section, we would like to elucidate the property of the Majorana fermion. In the semi-infinite system with the multiple Majorana fermions, it is, however, not easy to distinguish the topological phases with the different topological numbers (winding numbers) by focusing on the local density of states at the edge. This is because the energy states hosting Majorana fermions belong to the same zero energy. Therefore, we have investigated the system size dependence of the low energy spectra and that of the odd-frequency pair amplitude. Moreover, we have added

the perturbation breaking the chiral symmetry which removes the multiple Majorana fermions.

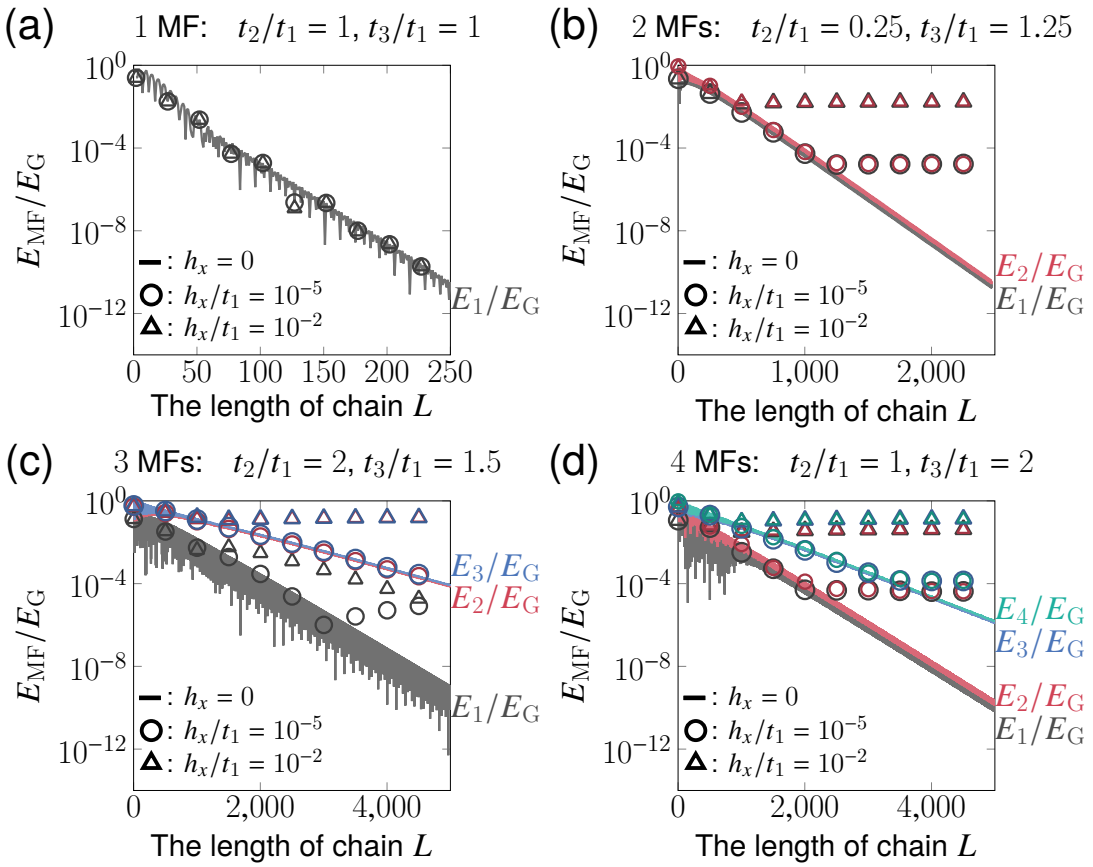

Figure 3.4: (a)–(d) Low energy spectra as a function of L in the (a) 1 MF (b) 2 MF (c) 3 MF (d) 4 MF phases. For $h_x \neq 0$ (◯ and △ plots), the chiral symmetry protecting Majorana fermion is broken. $\Delta_{\uparrow\uparrow} = 0.18t_1$, $\Delta_{\downarrow\downarrow} = 1.8t_1$, $\theta = \pi/4$, $h/t_1 = 2$, $\mu/t_1 = 1$. [7]

To describe the interference of Majorana fermions at both edges, we have shown the spatial dependence of the low energy spectra as a function of the system size in Figs. 3.4(a)–3.4(d). They have been calculated by the diagonalization of the Hamiltonian in the real space in Eq. (3.1). The energy modes are labeled E_1, E_2, E_3, and E_4 in ascending order. These four values of energy correspond to the Majorana fermions, and these energy spectra are normalized by the effective energy gap $E_{\rm G}$ at each system size. For example, in the 1 MF (2 MF) phase, $E_{\rm G}$ is the second (third) smallest energy.

With the chiral symmetry, since multiple Majorana fermions phases can be achieved, the smallest energy modes, related to Majorana fermions, approach zero as the increase with the system size [solid line plots in Figs. 3.4(a)–3.4(d)]. In the 1 MF phase, shown in Fig. 3.4(a), E_1 decreases and approaches zero with an oscillation as the system size increases. In the 2 MF

phase, shown in Fig. 3.4(b), E_1 and E_2 go to zero with degeneracy. These two energy modes are less oscillating. The three energy modes in the 3 MF phases show different behavior compared to the 2 MF phases as shown in Fig. 3.4(c). The energy E_1 approaches zero faster than E_2 and E_3 with the increase of the system size, and it has a large fluctuation while these degenerate E_2 and E_3 have little oscillation. In Fig. 3.4(d), the four energy modes in the 4 MF phase are divided into two ones, and the energy ones E_1 and E_2 are fluctuating for $L < 1000$.

The $\bigcirc$ and $\triangle$ plots in Fig. 3.4 depict the energy spectra as a function of the system size for $h_x/t_1 = 10^{-5}, 10^{-2}$. The nonzero h_x means the perturbation breaking the Majorana fermions which are protected by the chiral symmetry. In the 1 MF phase shown in Fig. 3.4(a), the energy spectrum does not change regardless of the magnitude of the perturbation. In the 2 MF phase, the degenerate energy modes do not go to zero but converge to a nonzero value as shown in Fig. 3.4(b). The converged value is on the order of $E_{\mathrm{MF}}/E_{\mathrm{G}} \sim h_x/t_1$. In the 3 MF phase, when a large perturbation is applied, the two degenerate energy modes become constant with the increase of L [Fig. 3.4(c)]. The nonzero value is about $E_{\mathrm{MF}}/E_{\mathrm{G}} \sim 10h_x/t_1$. Although the other energy mode changes to a gentle slope, it decreases toward zero. Figure 3.4(d), in the 4 MF phase, shows that the four energy modes converge to nonzero values. These converged values are on the order of $E_{\mathrm{MF}}/E_{\mathrm{G}} \sim h_x/t_1$ or $10h_x/t_1$. From these results, it can be seen that it is not easy to detect the zero-energy state in the phase with an even number of Majorana fermions when magnetic fields are unintentionally applied in the x direction that breaks the chiral symmetry.

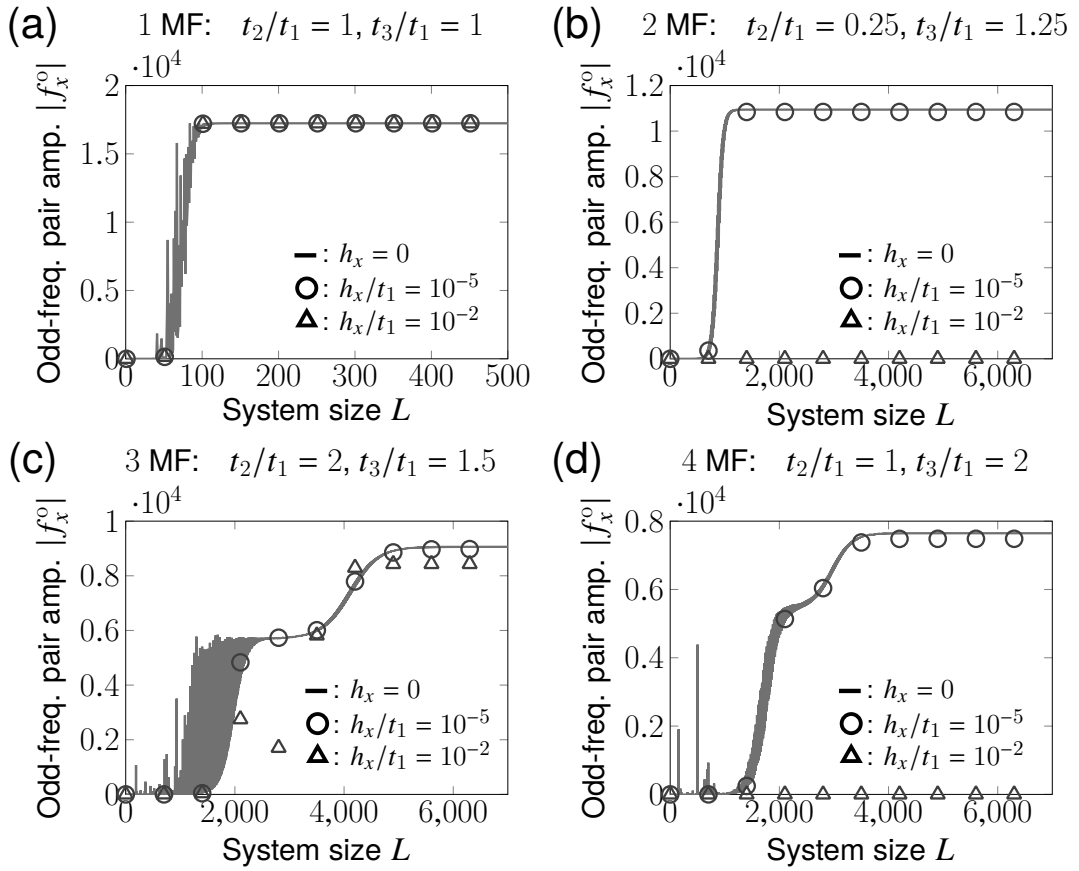

Figure 3.5: The x component of the odd-frequency pair amplitude at the edge $j = 1$ as a function of the system size L in the (a) 1 MF (b) 2MFs (c) 3MFs (d) 4MFs phases. $\theta = \pi/4$, $\Delta_{\uparrow\uparrow} = 0.18t_1$, $\Delta_{\downarrow\downarrow} = 1.8t_1$, $h/t_1 = 2$, $\mu/t_1 = 1$, $\omega/t_1 = 10^{-5}$. For $h_x \neq 0$ (◯ and △ plots), the chiral symmetry protecting Majorana fermions is broken. [7]

To correlate the multiple Majorana fermions and odd-frequency Cooper pairs, we demonstrate the odd-frequency pair amplitude enhanced by Majorana fermions. According to a spectrum bulk boundary correspondence, the x component of the odd-frequency $\mathbf{f}$ vector is closely related to the number of Majorana fermions in this system [Appendix 3.9]. For that reason, we have focused on the x component of the odd-frequency $\mathbf{f}$ vector as a function of the system size in 1, 2, 3, and 4 MF phases [Figs. 3.5(a)–3.5(d)]. These values are calculated by the Matsubara Green's function as written in Eqs. (3.8), (3.11), and (3.16).

We first explain the case where the system has chiral symmetry [the solid lines in Figs. 3.5(a)–3.5(d)], similar to the energy spectra shown in Fig. 3.4. In the 1 MF phase, the odd-frequency pair amplitude increases sharply near $L = 50$ with an irregular oscillation, and saturates for the large L as shown in Fig. 3.5(a). Although the 2 MF case is similar to the 1MF one, the pair amplitude is enhanced with a regular oscillation [Fig. 3.5(b)]. In the 3 MF and 4 MF

cases, these odd-frequency pair amplitudes have two plateaus, and they are fluctuating before the first plateaus as shown in Figs. 3.5(c) and 3.5(d). These two plateaus are corresponding to the two energy modes shown in Figs. 3.4(c) and 3.4(d), and they tell us the existence of multiple Majorana phases.

Additionally, we have investigated the change in the odd-frequency pair amplitude when the chiral symmetry is broken. The ◯ and △ plots in Figs. 3.5(a)–3.5(d) show how the odd-frequency pair amplitude at the edge of the system changes with increasing the system size for $h_x/t_1 = 10^{-5}$ and 10^{-2}, respectively. When the order of the perturbations h_x is similar to that of the Matsubara frequency ω, the single plateaus in the 1 MF and 2 MF phases and the double plateaus in the 3 MF and 4 MF phases are still kept [the ◯ plot in Figs. 3.5(a)–3.5(d)]. Even if small magnetic fields that break chiral symmetry are applied, the odd-frequency pair amplitude at a finite frequency tells us the remnants of the multiple Majorana fermions.

For the large perturbations compared to the Matsubara frequency, the single plateau in the 1 MF phase does not change [the △ plot in Fig. 3.5(a)]. The two plateaus in the 3 MF phase are transformed into one plateau structure [the △ plot in Fig. 3.5(c)]. The odd-frequency pair amplitude, in the even number of Majorana fermions phases, is suppressed, and the single and double plateaus vanish [the △ plot in Figs. 3.5(b) and 3.5(c)]. It is because that the energy modes, enhancing the odd-frequency Cooper pairs, with the same localization length are mixed by the chiral symmetry breaking and the degeneracy at the almost zero energy can be solved [This can be read from Figs. 3.4(c) and 3.4(d)].

3.5 Spatial dependence of odd-frequency pair amplitude

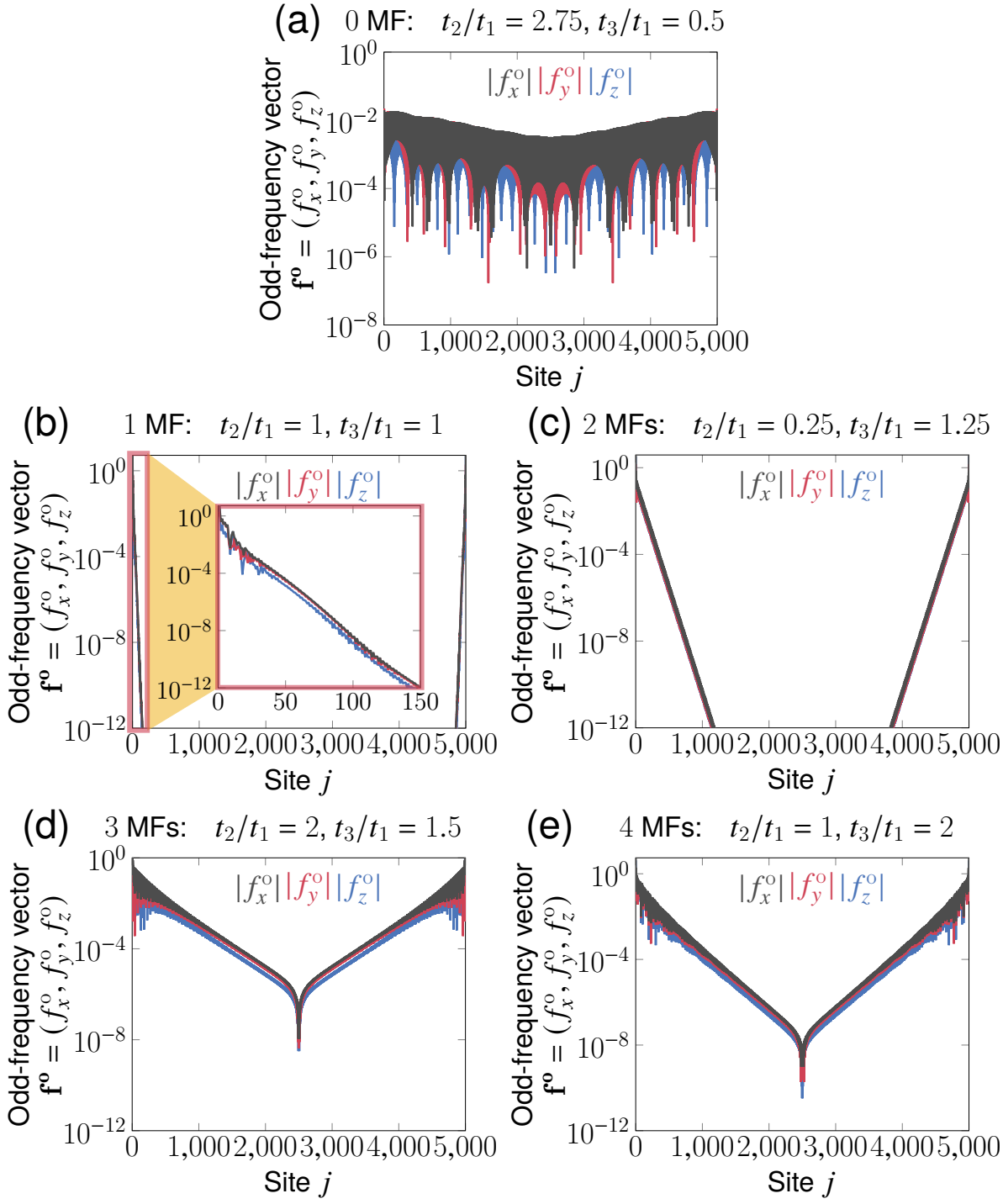

Figure 3.6: The spatial dependence of the odd-frequency $\mathbf{f}$ vector in the (a) 0 MF (b) 1 MF (c) 2 MF (d) 3 MF (e) 4 MF phases. $\theta = \pi/4$, $\Delta_{\uparrow\uparrow}/t_1 = 0.18$, $\Delta_{\downarrow\downarrow}/t_1 = 1.8$, $h/t_1 = 2$, $\mu/t_1 = 1$, $L = 5000$. $\omega/t_1 = E_G/2$: (a) 2.3×10^{-3}, (b) 3.3×10^{-2}, (c) 2.9×10^{-2}, (d) 1.2×10^{-2}, (e) 1.4×10^{-2}. [7]

The next important thing to understand the relationship between the multiple Majorana fermions and odd-frequency Cooper pairs is the spin texture of odd-frequency pair amplitude. To evaluate the spin texture, we define the **f** vector of the odd-frequency pairing as Eq. (3.10), as well as the **d** vector of the spin-triplet superconducting pair potential. In this section, we analyze what kind of spatial dependence the odd-frequency **f** vector has and how the spin texture of it is related to that of the **d** vector.

Figure 3.6 shows the spatial dependence of the odd-frequency vector. It is calculated by the recursive Green's function's formulation [Eqs. (3.13), (3.16), and (3.18)] In the 0 MF phase, the components of the odd-frequency **f** vector are small, and spreads throughout the system with oscillations as shown in Fig. 3.6(a). In the 1 and 2 MF phases, the odd-frequency pair amplitudes are strongly localized at the edge of the system [Figs. 3.6(b) and 3.6(c)]. On the other hand, in the 3 and 4 MF phases, the pair amplitudes have large values with oscillations at the edge, and it spreads toward the center compared to in the 1 and 2 MF phases [Figs. 3.6(d) and 3.6(e)].

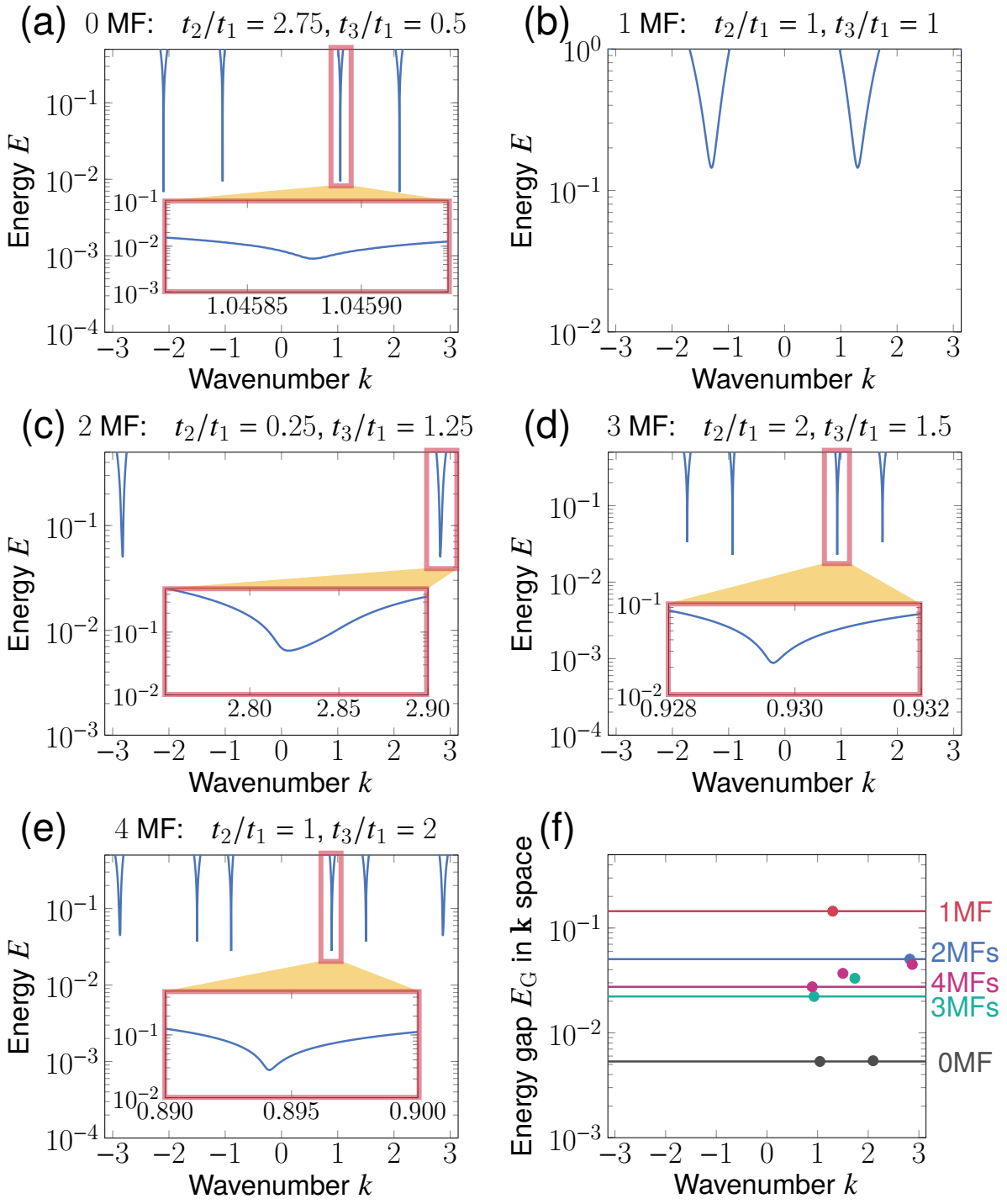

Figure 3.7: Energy bands ($E > 0$) of superconducting states in **k** space. (a) 0 MF, (b) 1 MF, (c) 2 MF, (d) 3 MF, (e) 4 MF phases. (f) The comparison of lowest energy states in each phase. $\theta = \pi/4$, $\Delta_{\uparrow\uparrow}/t_1 = 0.18$, $\Delta_{\downarrow\downarrow}/t_1 = 1.8$, $h/t_1 = 2$, $\mu/t_1 = 1$. [7]

These behaviors of the odd-frequency pair amplitudes can be explained by the magnitude of the superconducting gap in **k** space. This is because the spread of the odd-frequency pair amplitude in a superconducting state is about the coherence length $\xi \propto 1/\Delta$ where Δ means

a superconducting gap. Figures 3.7(a)–3.7(e) depict the electron part ($E > 0$) of energy dispersions in 1–4 MF phases. These energy bands are calculated by the diagonalization of the Hamiltonian [Eq. (3.6)] under a periodic boundary condition. The smallest gaps in the 0, 1, 3, and 4 MF phases are located near $k = 1$ while that in the 2 MF phase be near $k = \pi$. We also show a comparison of the superconducting gap sizes in Fig. 3.7(f). Comparing Figs. 3.6(a)–(e) and Fig. 3.7, we can find that the magnitude of the spread of odd-frequency pair amplitude is in ascending order of the minimum gap.

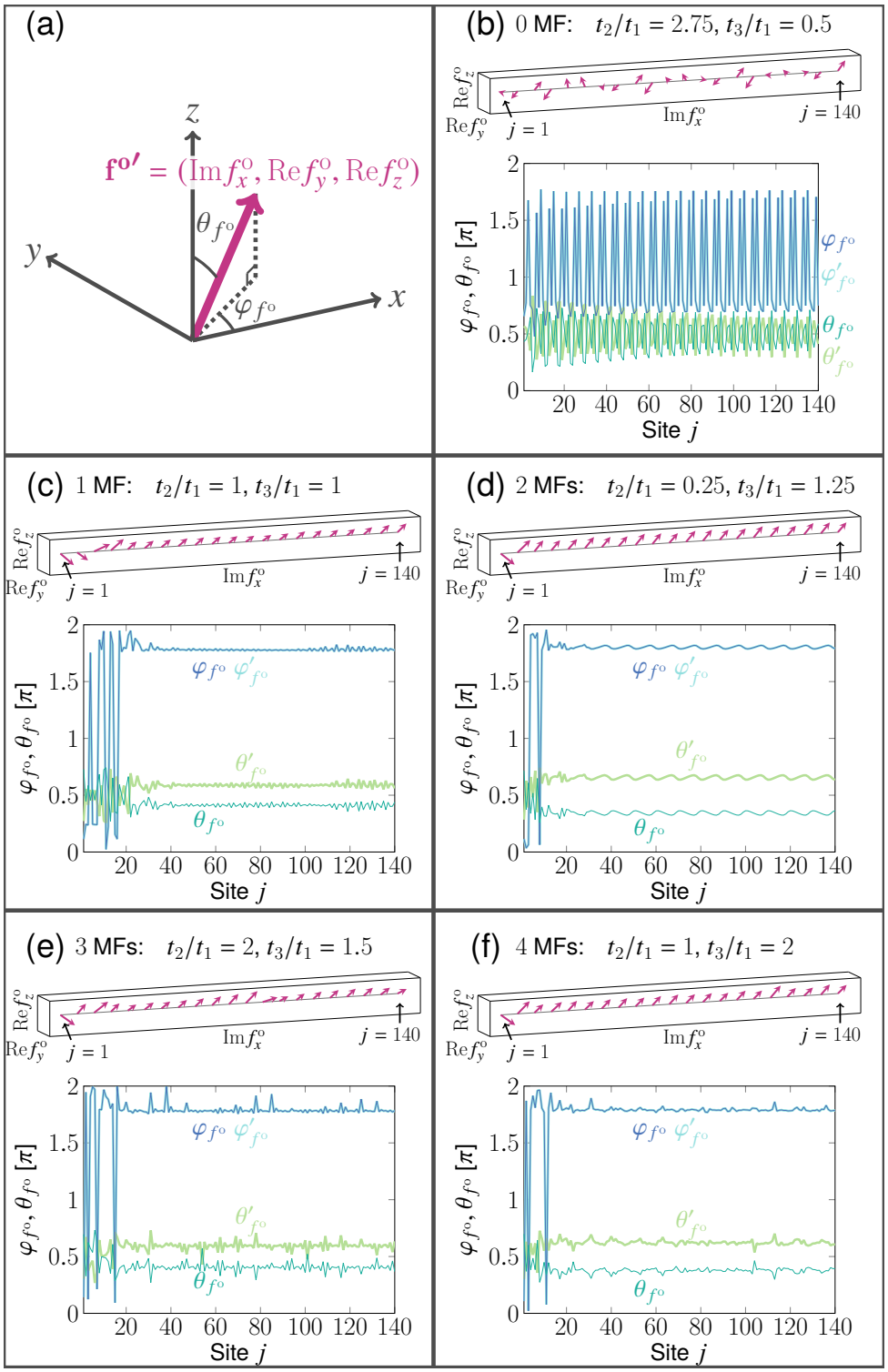

Figure 3.8: The direction of the odd-frequency $\mathbf{f}$ vector: $\mathbf{f}^{o\prime} = [\mathrm{Im}f^o_x, \mathrm{Re}f^o_y, \mathrm{Re}f^o_z] = [\|\mathbf{f}^{o\prime}\| \sin\theta_{f^o} \cos\varphi_{f^o}, \|\mathbf{f}^{o\prime}\| \sin\theta_{f^o} \sin\varphi_{f^o}, \|\mathbf{f}^{o\prime}\| \cos\theta_{f^o}]$ in the (b) 0 MF (c) 1 MF (d) 2 MF (e) 3 MF (f) 4 MF phases. The unit vector $\mathbf{f}^{o\prime}/\|\mathbf{f}^{o\prime}\|$ (upper figure) and the angle of the vector $\varphi_{f^o}, \theta_{f^o}$ (lower figure) are plotted as a function of site j. We focus on near the edge of the system ($j \in [1, 140]$). $\theta = \pi/4$, $\Delta_{\uparrow\uparrow}/t_1 = 0.18$, $\Delta_{\downarrow\downarrow}/t_1 = 1.8$, $h/t_1 = 2$, $\mu/t_1 = 1$, $L = 5000$. $\omega/t_1 = E_G/2$: (a) 2.3×10^{-3}, (b) 3.3×10^{-2}, (c) 2.9×10^{-2}, (d) 1.2×10^{-2}, (e) 1.4×10^{-2}. φ'_{f^o} and θ'_{f^o}: φ_{f^o} and θ_{f^o} when $h_y \to -h_y$. [7]

To see anisotropies of the odd-frequency pair amplitude, we illustrate the direction of the odd-frequency $\mathbf{f}$ vectors $\mathbf{f^{o\prime}} = [\mathrm{Im}f_x^{\mathrm{o}}, \mathrm{Re}f_y^{\mathrm{o}}, \mathrm{Re}f_z^{\mathrm{o}}]$ [Fig. 3.8(a)] normalized by themself, as shown upper panels in Figs. 3.8(b)–3.8(f). Also, we depict the angle of the vectors $\theta_{f^{\mathrm{o}}}$, $\{\tan\theta_{f^{\mathrm{o}}} = \sqrt{(\mathrm{Im}f_x^{\mathrm{o}})^2 + (\mathrm{Re}f_y^{\mathrm{o}})^2}/\mathrm{Re}f_z^{\mathrm{o}}, \theta_{f^{\mathrm{o}}} \in [0,\pi]\}$ and $\varphi_{f^{\mathrm{o}}}$, $\{\tan\varphi_{f^{\mathrm{o}}} = \mathrm{Re}f_y^{\mathrm{o}}/\mathrm{Im}f_x^{\mathrm{o}}, \varphi_{f^{\mathrm{o}}} \in [0,2\pi]\}$ to capture their direction clearly in lower panels in Figs. 3.8(b)–3.8(f). Particularly, we focus on near the edge of the system $j \in [1, 140]$ to correlate the vectors to the edge states. In the trivial (0 MF) phase, the sign of the y and z components changes frequently [Fig. 3.8(b)]. On the other hand, in the topological (1–4 MF) phases, the sign of the x component change near the edge but $\varphi_{f^{\mathrm{o}}}$ and $\theta_{f^{\mathrm{o}}}$ become constant with small oscillations slightly away from the edge [Figs. 3.8(c)–3.8(f)]. Moreover, the odd-frequency $\mathbf{f}$ vector, in each topological phase, points in almost the same direction [This behavior is not seen in the even-frequency $\mathbf{f}$ vectors as shown in Appendix 3.10]. The fixed vectors point slightly positive from the x axis to the y and z axis.

To investigate the effect of the magnetic fields on the orientation of the odd-frequency $\mathbf{f}$ vector, we change the sign of h_y. Here, the sign of h_y does not depend on the winding number [Appendix 3.8]. The angles $\varphi'_{f^{\mathrm{o}}}$ and $\theta'_{f^{\mathrm{o}}}$ represent $\varphi_{f^{\mathrm{o}}}$ and $\theta_{f^{\mathrm{o}}}$ when the sign of h_y is inverted, respectively. As can be seen from Figs. 3.8(b)–3.8(f), $\theta_{f^{\mathrm{o}}}$ becomes $\pi - \theta_{f^{\mathrm{o}}}$ for the sign inversion of h_y while $\varphi_{f^{\mathrm{o}}}$ does not change. In other words, the sign inversion of h_y inverts the sign of f_z^{o}.

It can be understood from the analytical calculation in the bulk that the y component of the magnetic fields affects the z component of the even-frequency $\mathbf{f}$ vector. We calculate even-frequency spin-triplet $\mathbf{f}$ vector in the bulk $*$ as

$$
\begin{aligned}
f_x^{\mathrm{e}} &= \frac{i}{A}\big[(\Delta_{\uparrow\uparrow}+\Delta_{\downarrow\downarrow})h_z^2\sin k + 2(\Delta_{\uparrow\uparrow}-\Delta_{\downarrow\downarrow})\varepsilon h_z \sin k + (\Delta_{\uparrow\uparrow}+\Delta_{\downarrow\downarrow})h_y^2 \sin k \\
&\qquad + (\Delta_{\uparrow\uparrow}+\Delta_{\downarrow\downarrow})\omega^2 \sin k + 4\Delta_{\uparrow\uparrow}\Delta_{\downarrow\downarrow}(\Delta_{\uparrow\uparrow}+\Delta_{\downarrow\downarrow})\sin^3 k + (\Delta_{\uparrow\uparrow}+\Delta_{\downarrow\downarrow})\varepsilon^2 \sin k\big] \\
f_y^{\mathrm{e}} &= \frac{1}{A}\big[(\Delta_{\downarrow\downarrow}-\Delta_{\uparrow\uparrow})h_z^2\sin k - 2(\Delta_{\uparrow\uparrow}+\Delta_{\downarrow\downarrow})\varepsilon h_z \sin k + (\Delta_{\uparrow\uparrow}-\Delta_{\downarrow\downarrow})h_y^2 \sin k \\
&\qquad + (\Delta_{\downarrow\downarrow}-\Delta_{\uparrow\uparrow})\omega^2 \sin k + 4\Delta_{\uparrow\uparrow}\Delta_{\downarrow\downarrow}\sin^3 k + (\Delta_{\downarrow\downarrow}-\Delta_{\uparrow\uparrow})\varepsilon^2 \sin k\big] \\
f_z^{\mathrm{e}} &= \frac{1}{A}\big[2(\Delta_{\uparrow\uparrow}-\Delta_{\downarrow\downarrow})h_y h_z \sin k + 2(\Delta_{\uparrow\uparrow}+\Delta_{\downarrow\downarrow})\varepsilon h_y \sin k\big]
\end{aligned}
\tag{3.19}
$$

$*$odd-frequency spin-triplet pair amplitude does not exist in the bulk

with

$$
\begin{aligned}
A =& h_z^4 + 2\left[h_y^2 + \omega^2 + 2(\Delta_{\uparrow\uparrow}^2 + \Delta_{\downarrow\downarrow}^2)\sin^2 k - \varepsilon^2\right]h_z^2 + 8(\Delta_{\uparrow\uparrow}^2 - \Delta_{\downarrow\downarrow}^2)\varepsilon h_z \sin^2 k + h_y^4 \\
&+ 2(\omega^2 + 4\Delta_{\uparrow\uparrow}\Delta_{\downarrow\downarrow}\sin^2 k - \epsilon^2)h_y^2 + \omega^4 + 2\left[2(\Delta_{\uparrow\uparrow}^2 + \Delta_{\downarrow\downarrow}^2)\sin^2 k + \varepsilon^2\right]\omega^2 \\
&+ 16\Delta_{\uparrow\uparrow}^2\Delta_{\downarrow\downarrow}^2 \sin^4 k + 4(\Delta_{\uparrow\uparrow}^2 + \Delta_{\downarrow\downarrow})\varepsilon^2 \sin^2 k + \epsilon^4
\end{aligned}
$$

by taking the inverse [Eq. (3.8)] of the Hamiltonian [Eq. (3.5)] in **k** space and using Eqs. (3.10) and (3.12). As you can see Eq. (3.19), f_z^{e} is an odd function of h_y while f_x^{e} and f_y^{e} are even functions of it. The sign change of f_z^{o} vector, caused by the operation $h_y \to -h_y$, is inherited from the nature in the bulk. This is because a translational symmetry breaking generates odd-frequency spin-triplet even-party Cooper pairs from even-frequency spin-triplet odd-parity ones.

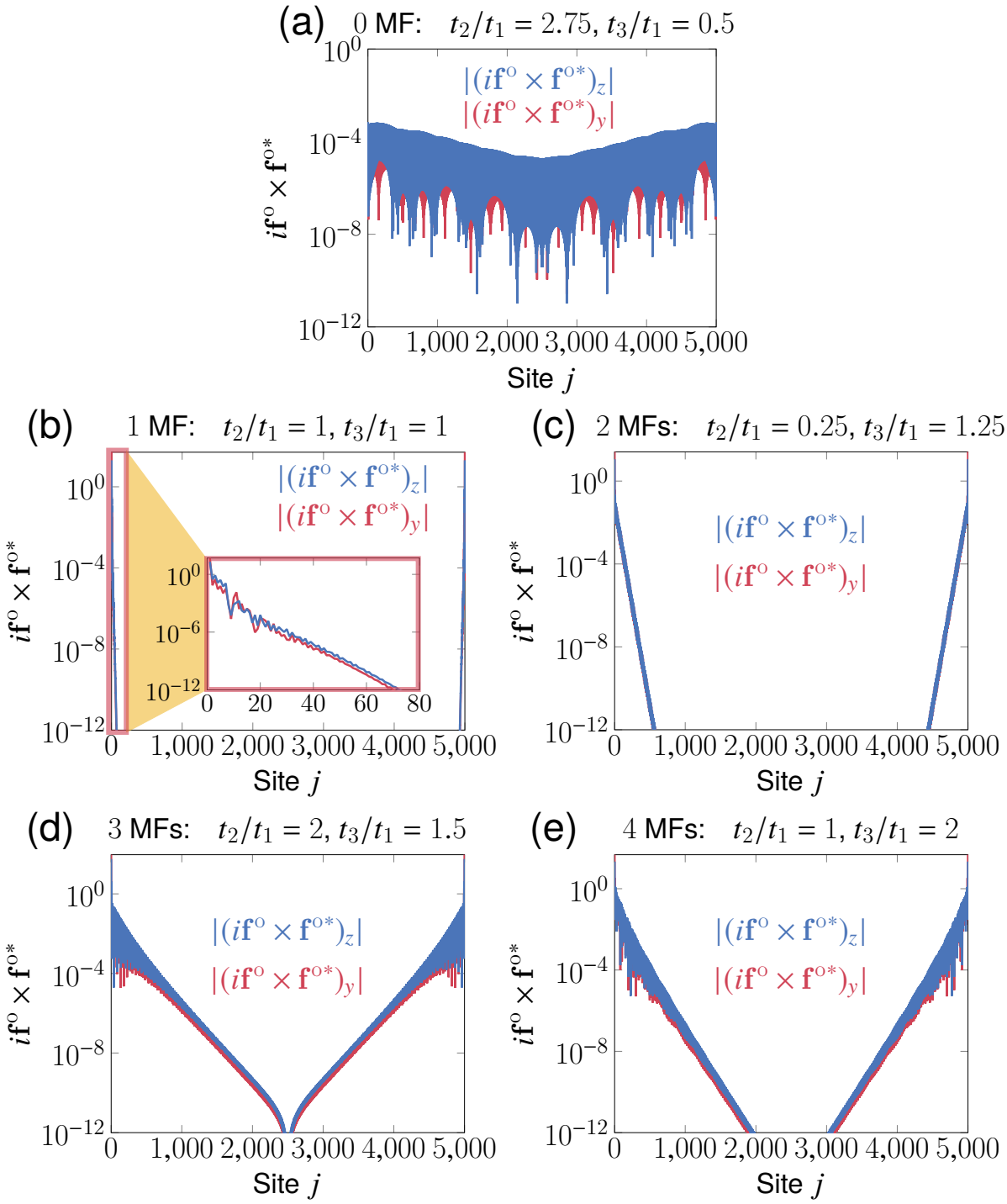

Figure 3.9: The spatial dependence of the spin of the odd-frequency Cooper pair states $\langle \sigma^{o} \rangle \propto i\mathbf{f}^{o} \times \mathbf{f}^{o*}$. (a) 0 MF, (b) 1 MF, (c) 2 MF, (d) 3 MF, (e) 4 MF phases. $\theta = \pi/4$, $h/t_1 = 2$, $\mu/t_1 = 1$. $\omega/t_1 = E_G/2$: (a) 2.3×10^{-3}, (b) 3.3×10^{-2}, (c) 2.9×10^{-2}, (d) 1.2×10^{-2}, (e) 1.4×10^{-2}. [7]

In this system, the nonunitary state is important for accessing the phase with multiple Majorana fermions. The matter can be understood from the structure of the winding number that is mentioned in Appendix 3.8. To investigate the nonunitary state of the odd-frequency

Cooper pair $\langle\sigma^{o}\rangle$, we calculate a cross vector $\langle\sigma^{o}\rangle \propto i\mathbf{f}^{o}\times\mathbf{f}^{o*}$ from the odd-frequency $\mathbf{f}$ vector. The cross vector takes a nonzero value for the nonunitary states.

The spatial dependence of the cross vectors in the 0–4 MF phases, shown in Figs. 3.9(a)–3.9(e), are similar to that of the pair amplitudes in Figs. 3.6(a)–3.6(e). They are on the order of about the square of the pair amplitude. In the first place, the spin state of pair potential $\langle\sigma\rangle \propto i\mathbf{d}\times\mathbf{d}^{*}$ is obtained as $i\mathbf{d}\times\mathbf{d}^{*} = [0, 0, (\Delta_{\uparrow\uparrow}^{2} - \Delta_{\downarrow\downarrow}^{2})/2]$ where we assume $d_z = 0$ and $\Delta_{\uparrow\uparrow}$ and $\Delta_{\downarrow\downarrow}$ are real. Since the magnetic fields, applied along $y = z$ direction, tilt the spin state of the odd-frequency Cooper pairs in the direction of $y = z$, only the x components of $\langle\sigma^{o}\rangle \propto i\mathbf{f}^{o}\times\mathbf{f}^{o*}$ is zero. This result can also be easily confirmed in a Kitaev chain [Appendix 3.11].

3.6 Discussion

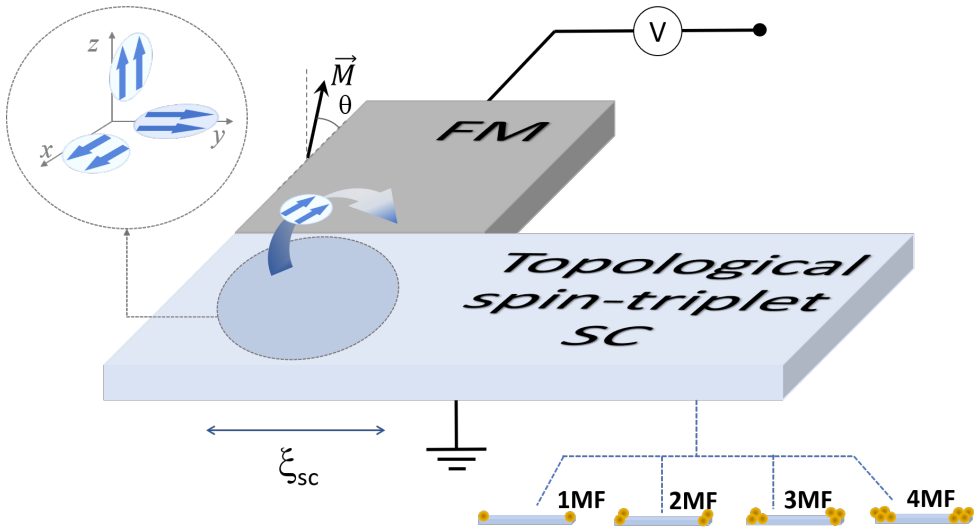

Figure 3.10: A Schematic view for detecting spin-dependent odd-frequency Cooper pairs in a topological spin-triplet superconductor by the scanning tunneling spectroscopy. A ferromagnetic (FM) tip with impurities contacts the edge of a topological spin-triplet superconductor (SC). [7]

In this section, we propose a method for detecting the spin structure of the odd-frequency Cooper pairs. When the spin direction of the odd-frequency spin-triplet s-wave Cooper pair is equal to that of the ferromagnet, it can penetrate into the ferromagnet over a long distance as compared to the case where the spin directions are different [40, 69, 70, 71, 72, 37]. In addition, the odd-frequency spin-triplet s-wave Cooper pairs are robust and resonate in impurities. This behavior has been known in the context of the anomalous proximity effect in a diffusive normal

metal attached to a spin-triplet p-wave superconductor junction [5, 42, 43, 44, 54, 1].

Taking advantage of these properties of the odd-frequency s-wave Cooper pairs, we propose a way to observe the electronic density of states of a topological spin-triplet superconductor by the scanning tunneling spectroscopy with a ferromagnetic chip containing impurities as shown in Fig. 3.10. Then, the local density of states is expected to have a zero-energy peak or splitted ones. From the height of this peak, it may be possible to observe one or two plateau structures in Fig. 3.5 and the structure of the odd-frequency $\mathbf{f}$ vector with a fixed orientation as shown in Figs. 3.8(b)–3.8(f).

3.7 Conclusion

In this chapter, we have shown that the spatial profile of the odd-frequency spin-triplet s-wave Cooper pairs can become an indicator for detecting and distinguishing the topological phases with different numbers of Majorana fermions in a spin-triplet p-wave superconductor with magnetic fields. It is not easy to distinguish the topological phases with different numbers of Majorana fermions by only focusing on the local density of states at the edge of the semi-infinite system. To solve this difficulty, we have considered the situation where the energy level of Majorana fermions deviate from zero by choosing the finite system size and applying additional magnetic fields to break the chiral symmetry. The induced odd-frequency pair amplitude at the edge as a function of the system size has two plateaus when the two energy modes with different localization lengths exist, such as in the 3 and 4 Majorana fermions phases. While the weak magnetic fields that break the chiral symmetry gap out the zero energy states in the even number of Majorana fermions phase, the odd-frequency pair amplitude at the edge as a function of the system size keeps its original shape. This result means that the odd-frequency pair amplitude tells us the fingerprints of the existence of the multiple Majorana fermions. The strong magnetic fields that break the chiral symmetry suppress the odd-frequency pair amplitude in only the even number of Majorana fermion phases. The suppression allows us to distinguish between the even and odd numbers of Majorana fermions.

The structure of the winding number tells us the importance of the nonunitary superconducting states to access the multiple Majorana phases. Therefore, we have defined the odd-frequency

f vector on the analogy of the **d** vector that characterizes the spin-triplet pair potential. Using the odd-frequency **f** vector, we have obtained the following three results. The odd-frequency **f** vectors near the edge are oriented in the same direction in each topological phase, unlike the even-frequency ones. By inverting the sign of the magnetic fields with keeping the winding number, we have found that the magnetic response of the odd-frequency **f** vector inherits the properties of the even-frequency one in the bulk. The nonunitary spin states of the odd-frequency Cooper pairs that are defined by the cross vector $i\mathbf{f}\times\mathbf{f}^*$ tend to point in the direction of the applied magnetic fields. Our results mean that the presence of the nonunitary spin state of odd-frequency Cooper pairs can feature the existence of a topological phase with multiple Majorana fermions.

3.8 Structure of the winding number

The winding number, defined in Eq. (3.7), characterizes the topology of the p-wave superconductor system shown in Fig. 3.1. In this Appendix, we investigate the structure of the winding number in the system.

The structure of the winding number is expressed by the off-diagonal component of the off-diagonalized Hamiltonian:

$$U^\dagger H(k) U = \begin{bmatrix} O & \tilde{H} \\ \tilde{H}^\dagger & O \end{bmatrix}, \tag{3.20}$$

where U is the 2×2 matrix diagonalizing the chiral operator $\Gamma = \tau_x\sigma_z$, and $H(k)$ is obtained in Eq. (3.6). When k change from $-\pi$ to π, the number of times of the determinant

$$\begin{aligned} \det\tilde{H} = {} & \varepsilon^2(k) - h_y^2 - h_z^2 + 4\Delta_{\uparrow\uparrow}\Delta_{\downarrow\downarrow}\sin^2 k \\ & + 2i\sin k\,[(\Delta_{\downarrow\downarrow} - \Delta_{\uparrow\uparrow})\varepsilon(k) - (\Delta_{\uparrow\uparrow} + \Delta_{\downarrow\downarrow})h_z] \end{aligned} \tag{3.21}$$

going around the origin on the complex plane corresponds to the winding number. Two matters can be seen from Eq. (3.21) as follows.

- The winding number does not depend on the sign of h_y.

- The nonunitary pairing ($\Delta_{\uparrow\uparrow} \neq \Delta_{\downarrow\downarrow}$) is important to reach the multiple Majorana fermion phases. [The term $2i \sin k(\Delta_{\uparrow\uparrow} - \Delta_{\downarrow\downarrow})\varepsilon(k)$ changes the sign of the imaginary part of $\det \tilde{H}$ more.]

In Sec. 3.5, we investigate the magnetic field response of the odd-frequency **f** vector by changing the sign of h_y so as not to change the phase. Additionally, we calculate the cross vector $i\mathbf{f}^{\mathrm{o}} \times \mathbf{f}^{\mathrm{o}*}$ to investigate the nonunitary state of the odd-frequency Cooper pairs.

3.9 Spectral bulk boundary correspondence

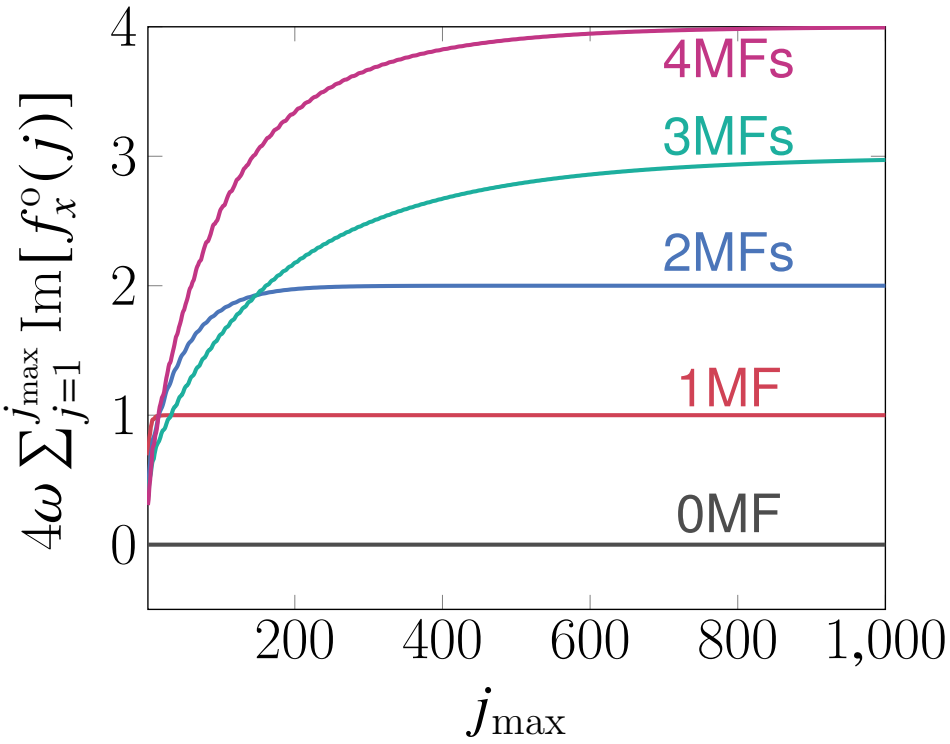

Figure 3.11: Sum of the odd-frequency **f** vector $\mathrm{Im} f_x$ from the edge $j = 1$ to $j_{\max}$ as a function of $j_{\max}$. This value represents F_{edge} [Eqs. 3.23 and 3.24] in the spectral bulk boundary correspondence [Eq. (3.22)] in a semi-infinite p-wave superconductor with magnetic fields at a infinitesimal frequency. $\theta = \pi/4$, $\Delta_{\uparrow\uparrow}/t_1 = 0.18$, $\Delta_{\downarrow\downarrow}/t_1 = 1.8$, $h/t_1 = 2$, $\mu/t_1 = 1$, $\omega/t_1 = 10^{-5}$. 0 MF: $t_2/t_1 = 2.75$, $t_2/t_1 = 0.5$, 1 MF: $t_2/t_1 = 1$, $t_3/t_1 = 1$, 2 MFs: $t_2/t_1 = 0.25$, $t_3/t_1 = 1.25$, 3 MFs: $t_2/t_1 = 2$, $t_3/t_1 = 1.5$, 4 MFs: $t_2/t_1 = 1$, $t_3/t_1 = 2$. [7]

Spectral bulk boundary correspondence is a relationship that connects a winding number being extended to a finite frequency and the odd-frequency pair amplitudes. The relationship is

defined in a semi-infinite system with chiral symmetry, and is written as

$$i\omega F^{\mathrm{odd}}_{\mathrm{edge}}(i\omega) = w_{\mathrm{bulk}}, \tag{3.22}$$

$$\begin{cases} w_{\mathrm{bulk}} = \frac{i}{2}\mathrm{Tr}_k\left[\Gamma G(\omega)\partial_k G^{-1}(i\omega)\right] \\ F^{\mathrm{odd}}_{\mathrm{edge}}(i\omega) = \mathrm{Tr}_j\left[\Gamma G(i\omega)\right], \end{cases} \tag{3.23}$$

with a Matsubara Green's function $G(i\omega)$ and a chiral operator Γ. For an infinitesimal Matsubara frequency, w_{bulk} becomes equal to the winding number.

In the p-wave superconductor with magnetic fields shown in Fig. 3.1, the second equation in Eq. (3.23) can be transformed as below:

$$\begin{aligned} F^{\mathrm{odd}}_{\mathrm{edge}} &= \sum_j \left[F_{j,j,\uparrow,\uparrow} - F_{j,j,\downarrow,\downarrow} + \tilde{F}_{j,j,\uparrow,\uparrow} - \tilde{F}_{j,j,\downarrow,\downarrow}\right] \\ &= 4\omega \sum_j \mathrm{Im} f^{\mathrm{o}}_x(j,z) \end{aligned} \tag{3.24}$$

where we use the chiral operator $\Gamma = \tau_x\sigma_z$ anticommuting with the Hamiltonian $H(k)$ in Eq. (3.6), the relation $\tilde{F} = -F^*$, and Eqs. (3.8)–(3.11). The sum of the odd-frequency vector $\mathrm{Im} f_x$ from the edge $j = 1$ to j_{max} [F_{edge} in Eq. (3.24)] is plotted as a function of j_{max} in Fig. 3.11. For a sufficiently large j_{max}, w_{bulk} matches the winding number (the number of Majorana fermions). In Sec. 3.4, we focus on f^{o}_x among the components of the odd-frequency $\mathbf{f}$ vector. This is because this component is most closely related to the winding number that is extended to a finite frequency.

3.10 Spatial dependence of even-frequency pair amplitude

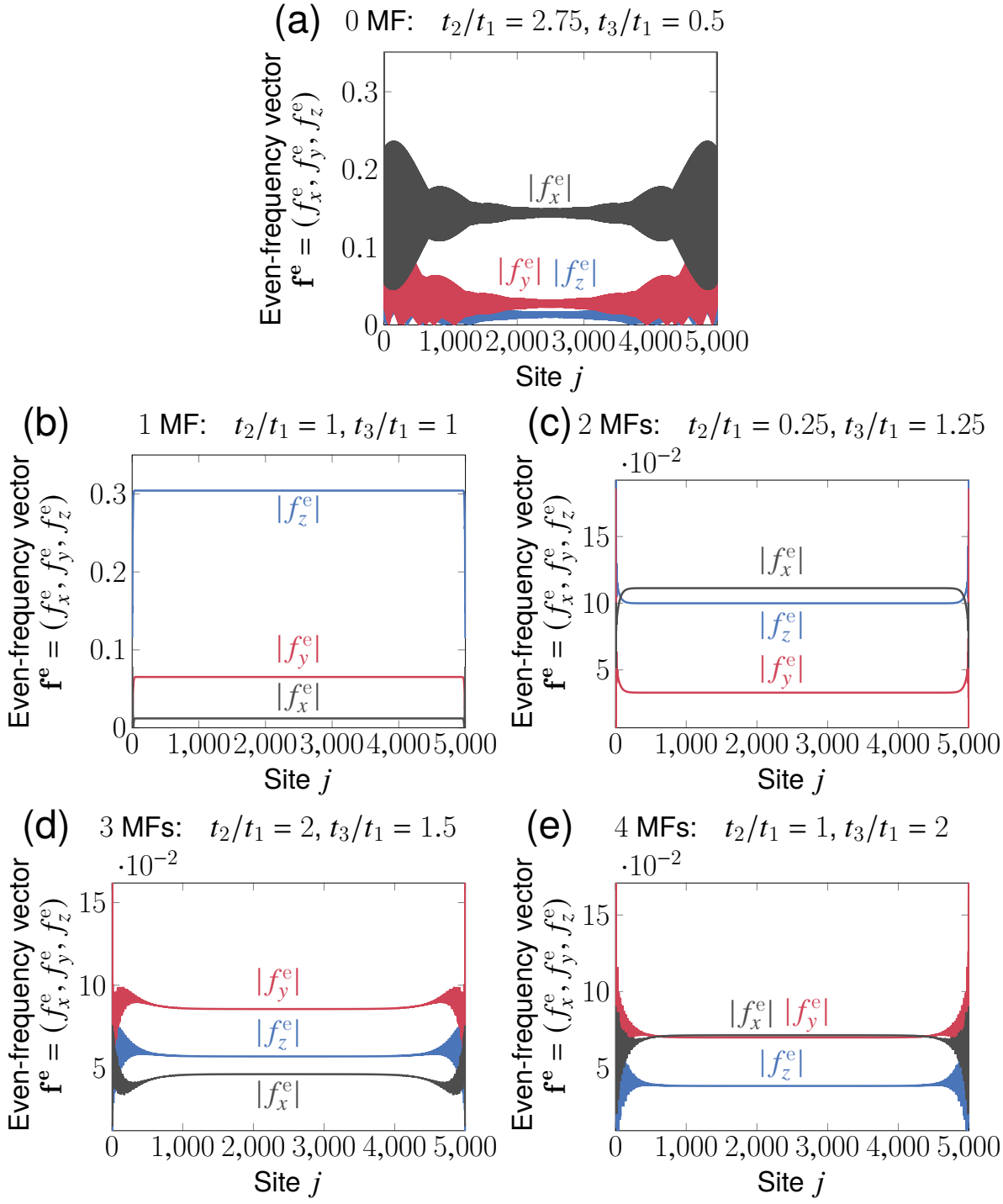

Figure 3.12: The spatial dependence of the even-frequency $\mathbf{f}$ vector in the (a) 0 MF (b) 1 MF (c) 2 MF (d) 3 MF (e) 4 MF phases. $\theta = \pi/4$, $\Delta_{\uparrow\uparrow}/t_1 = 0.18$, $\Delta_{\downarrow\downarrow}/t_1 = 1.8$, $h/t_1 = 2$, $\mu/t_1 = 1$, $L = 5000$. $\omega/t_1 = E_G/2$: (a) 2.3×10^{-3}, (b) 3.3×10^{-2}, (c) 2.9×10^{-2}, (d) 1.2×10^{-2}, (e) 1.4×10^{-2}. [7]

To compare the odd-frequency $\mathbf{f}$ vector to the even one, we calculate the spatial dependence of even one that is calculated by Eqs. (3.10) and (3.12). The spatial dependence of even-frequency $\mathbf{f}$ vector in 0–4 MF phases is shown in Figs. 3.12(a)–3.12(e) . In the trivial (0 MF) phase [Fig. 3.12(a)], the pair amplitudes oscillate throughout the space similar to odd-frequency pair amplitude in Fig. 3.6(a). In the topological (1–4 MF) phases [Fig. 3.12(b)–(e)], these values are constant near the bulk in Fig. 3.6(a). Particularly, in the 3 and 4 MF phases, the amplitudes oscillate near the edge as well as ones of odd-frequency in Figs. 3.6(d)and 3.6(e). The proportion of each component $|f_x^{\mathrm{e}}|$, $|f_y^{\mathrm{e}}|$, and $|f_z^{\mathrm{e}}|$ in 1–4MF [Figs. 3.12(b)–3.12(e)] are not equal unlike odd-frequency components [Figs. 3.6(b)–3.6(e)].

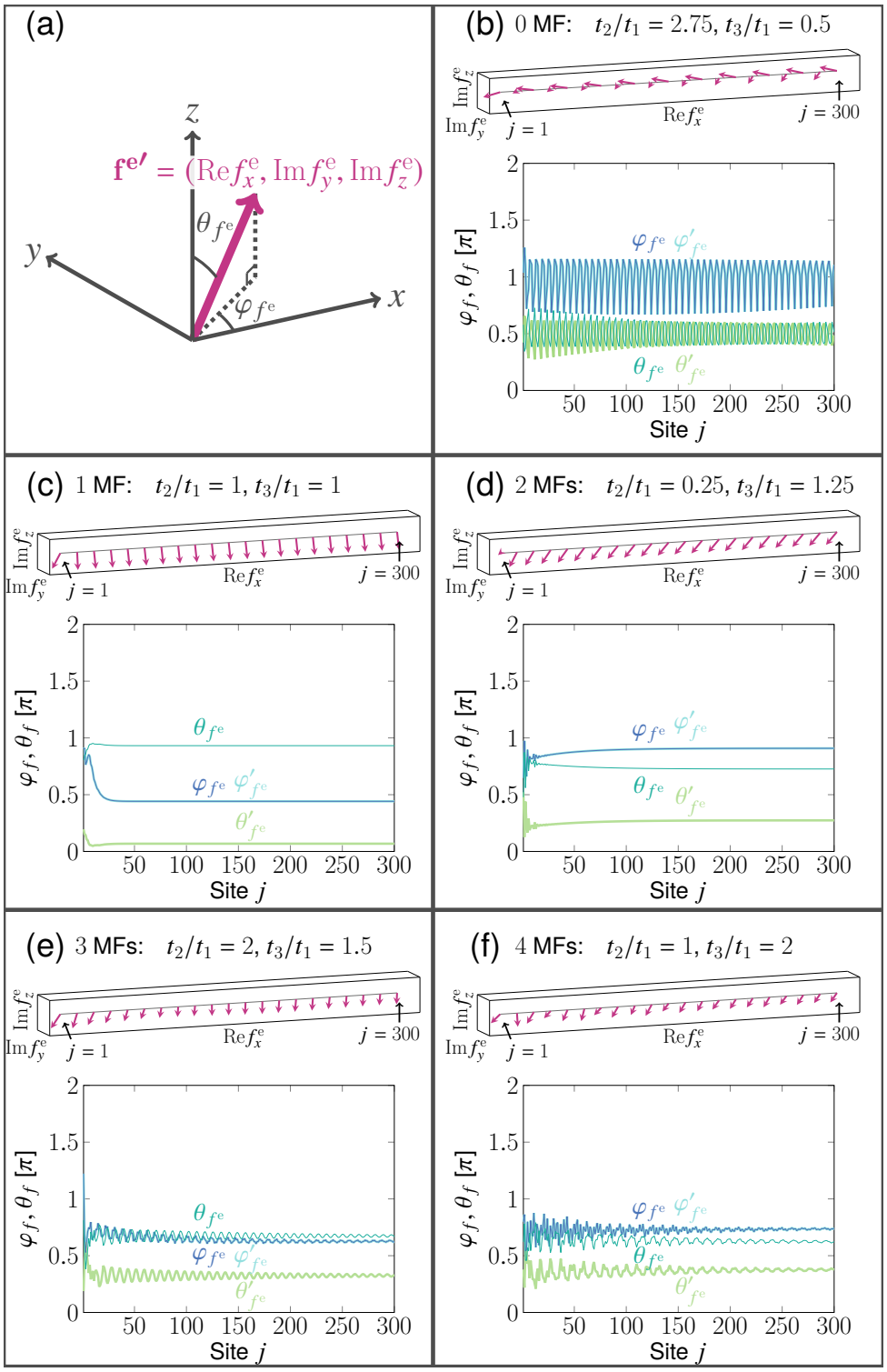

Figure 3.13: The direction of the even-frequency $\mathbf{f}$ vector: $\mathbf{f}^{e\prime} = [\mathrm{Re}f_x^e, \mathrm{Im}f_y^e, \mathrm{Im}f_z^e] = [\|\mathbf{f}^{e\prime}\| \sin\theta_{f^e} \cos\varphi_{f^e}, \|\mathbf{f}^{e\prime}\| \sin\theta_{f^e} \sin\varphi_{f^e}, \|\mathbf{f}^{e\prime}\| \cos\theta_{f^e}]$ in the (b) 0 MF (c) 1 MF (d) 2 MF (e) 3 MF (f) 4 MF phases. The unit vector $\mathbf{f}^{e\prime}/\|\mathbf{f}^{e\prime}\|$ (upper figure) and the angle of the vector $\varphi_{f^e}, \theta_{f^e}$ (lower figure) are plotted as a function of site j. We focus on near the edge of the system ($j \in [1, 300]$). $\theta = \pi/4$, $\Delta_{\uparrow\uparrow}/t_1 = 0.18$, $\Delta_{\downarrow\downarrow}/t_1 = 1.8$, $h/t_1 = 2$, $\mu/t_1 = 1$, $L = 5000$. $\omega/t_1 = E_G/2$: (a) 2.3×10^{-3}, (b) 3.3×10^{-2}, (c) 2.9×10^{-2}, (d) 1.2×10^{-2}, (e) 1.4×10^{-2}. φ'_{f^e} and θ'_{f^e}: φ_{f^e} and θ_{f^e} when $h_y \to -h_y$. [7]

To investigate the proportion of the pair amplitude $|f_x^{\mathrm{e}}|$, $|f_y^{\mathrm{e}}|$, and $|f_z^{\mathrm{e}}|$ in detail, we depicted the direction of the even-frequency $\mathbf{f}$ vector [upper figures in Figs. 3.13(b)–3.13(e)], that is defined in Fig. 3.13(a), and the angle $\theta_{f^{\mathrm{e}}}$ and $\varphi_{f^{\mathrm{e}}}$ [lower figures in Figs. 3.13(b)–3.13(e)] for $j \in [1, 300]$ in the $L = 5000$ sites system. In the 0 MF phase, as shown in Fig. 3.13(a), the even-frequency $\mathbf{f}$ vector oscillates around the negative direction of the x axis. In the 1MF phase, the direction is almost along the negative direction of the x axis without oscillation [Fig. 3.13(c)]. The even-frequency $\mathbf{f}$ vectors in 2MF, 3MF, and 4MF phases are roughly oriented in the direction of between $-x$ and $-z$ axes, that of y axis, that of between $-x$ and y axes, respectively [Figs. 3.13(d)–3.13(f), and also see Figs. 3.12(d)–3.12(f)]. The angle $\theta'_{f^{\mathrm{e}}}$ and $\varphi'_{f^{\mathrm{e}}}$ stand for $\theta_{f^{\mathrm{e}}}$ and $\varphi_{f^{\mathrm{e}}}$ when $h_y \to -h_y$, respectively. While $\varphi_{f^{\mathrm{e}}}$ does not change ($\varphi'_{f^{\mathrm{e}}} = \varphi_{f^{\mathrm{e}}}$) with the respect to the sign change of h_y, $\theta_{f^{\mathrm{e}}}$ change to $\pi - \theta_{f^{\mathrm{e}}}$ as shown in Figs. 3.13(b)–3.13(f).

In this appendix, we have got two important results. The even-frequency $\mathbf{f}$ vector in each topological phase does not point in the same direction, unlike the odd-frequency one. Similar to the odd-frequency $\mathbf{f}$ vector, the sign inversion of h_y inverts the sign of the z component of the even frequency $\mathbf{f}$ vector. These results support the discussion about the odd-frequency $\mathbf{f}$ vector in Sec. 3.4.

3.11 Spin structure of odd-frequency Cooper pairs in a Kitaev chain

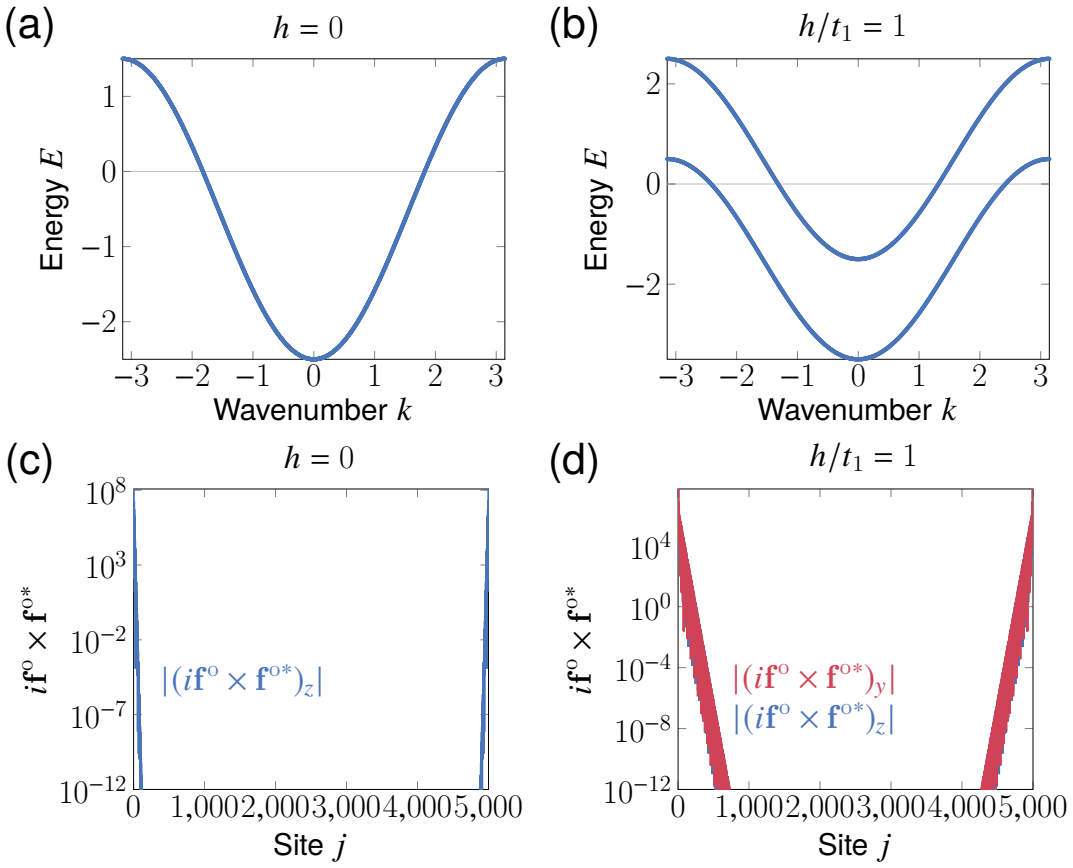

Figure 3.14: Energy bands of the Kitaev chain without pair potential for (a) $h = 0$ and (b) $h/t_1 = 1$ in $\mathbf{k}$ space. The spatial dependence of the spin of the odd-frequency Cooper pair states $\langle \sigma^{o} \rangle \propto i\mathbf{f}^{\mathbf{o}} \times \mathbf{f}^{\mathbf{o}*}$ for (c) $h = 0$ and (d) $h/t_1 = 1$ in real space: $\omega/t_1 = 10^{-5}$, $L = 5000$, $\Delta_{\uparrow\uparrow}/t_1 = 0.1$, $\Delta_{\downarrow\downarrow} = 0$. $\theta = \pi/4$, $\mu/t_1 = 0.5$. [7]

In Sec. 3.5, we have shown the spatial dependence of the spin states of the odd-frequency Cooper pairs $\langle \sigma^{o} \rangle$ in a p-wave superconductor with magnetic fields. The Kitaev chain, the simplest model expressing a spinless p-wave superconductor, is useful for investigating the effect of magnetic fields on the spin structure of the odd-frequency Cooper pairs. The Hamiltonian in Eqs. (3.1), and (3.5) (3.6) one can be rewritten as one in the Kitaev chain by replacing $\Delta_{\downarrow\downarrow}$, t_2, and $t_3 \to 0$.

The dispersions in the bulk of the Kitaev chain without pair potential ($\Delta_{\uparrow\uparrow} = \Delta_{\downarrow\downarrow} = 0$), shown in Figs. 3.14(a) and 3.14(b), were calculated by the diagonalization of the Hamiltonian in $\mathbf{k}$ space that is based on Eq. (3.6). Without magnetic fields, the up and down spin states are degenerate

to $E = -2t_1 \cos k - \mu$ [Fig. 3.14(a)]. For $h/t_1 = 1$, these states split to $E = -2t_1 \cos k - \mu \pm h$ [Fig. 3.14(b)].

The cross vector $i\mathbf{f^o} \times \mathbf{f^o}^*$ is proportional to the spin polarization of the odd-frequency Cooper pairs $\langle \sigma^{\mathrm{o}} \rangle$. Figure 3.14(c) [Figure 3.14(d)] shows the cross vector $i\mathbf{f^o} \times \mathbf{f^o}^*$ in the Kitaev chain without [with] magnetic fields. The spin of pair potential $\langle \sigma \rangle \propto i\mathbf{d} \times \mathbf{d}^* = [0, 0, \Delta^2_{\uparrow\uparrow}/2]$ points in the z direction. Without the magnetic fields, only the z component of $i\mathbf{f^o} \times \mathbf{f^o}^*$ exists since the spin state of the pair potential is inherited, as shown in Fig. 3.14(c). When magnetic fields in the $y = z$ direction are applied, the cross vector has the y component in addition to the z component [Fig. 3.14(d)]. These results indicate that the spin of the odd-frequency Cooper pairs inherits that of the pair potential, and tends to point in the direction of the magnetic fields.

Chapter 4

Summary

In this thesis, we have shown that odd-frequency Cooper pairs help us to understand one-dimensional topological superconductors hosting Majorana fermions. In Chap. 2, we have investigated the proximity effect in a Kitaev chain junction near a topological critical point. We have demonstrated that the odd-frequency Cooper pair causes the proximity effect even at the topological critical point. In Chap. 3, we have examined topological phases with multiple Majorana fermions in a p-wave superconductor. We have indicated that the odd-frequency pairing could be a good index for distinguishing between the topological phases.

The model being dealt with in this thesis is difficult to construct directly in experiments. We need to calculate in a system close to experiments. For example, calculations of transport phenomena in systems composed of superconducting nanowires are required.

Reference

[1] D. Takagi, S. Tamura, and Y. Tanaka, Phys. Rev. B **101**, 024509 (2020).

[2] A. Y. Kitaev, Usp. Fiz. Nauk (Suppl.) **44**, 131 (2001).

[3] Y. Asano and Y. Tanaka, Phys. Rev. B **87**, 104513 (2013).

[4] S. Tamura, S. Hoshino, and Y. Tanaka, Phys. Rev. B **99**, 184512 (2019).

[5] Y. Tanaka and A. A. Golubov, Phys. Rev. Lett. **98**, 037003 (2007).

[6] A. Umerski, Phys. Rev. B **55**, 5266 (1997).

[7] D. Takagi, M. T. Mercaldo, Y. Tanaka, and M. Cuoco, arXiv:2112.01009 (2021).

[8] M. T. Mercaldo, M. Cuoco, and P. Kotetes, Phys. Rev. B **94**, 140503(R) (2016).

[9] S. Kittaka, https://www.phys.chuo-u.ac.jp/labs/kittaka/contents/others/tc-history/index.html .

[10] J. Bardeen, L. N. Cooper, and J. R. Schrieffer, Phys. Rev. **108**, 1175 (1957).

[11] J. G. Bednorz and K. A. Müller, Z. für Phys. B **64**, 189 (1986).

[12] M. K. Wu, J. R. Ashburn, C. J. Torng, R. L. M. P. H. Hor, L. Gao, Z. J. Huang, Y. Q. Wang, and C. W. Chu, Physical review letters **58**, 908 (1987).

[13] Y. Kamihara, H. Hiramatsu, M. Hirano, R. Kawamura, H. Yanagi, T. Kamiya, and H. Hosono, J. Am. Chem. Soc. **128**, 10012 (2006).

[14] Y. Kamihara, T. Watanabe, M. Hirano, and H. Hosono, J. Am. Chem. Soc. **130**, 3296 (2008).

[15] A. P. Drozdov, M. I. Eremets, I. A. Troyan, V. Ksenofontov, and S. I. Shylin, Nature **525**, 73 (2015).

[16] E. Snider, N. Dasenbrock-Gammon, R. McBride, M. Debessai, H. Vindana, K. Vencatasamy, K. V. Lawler, A. Salamat, and R. P. Dias, Nature **586**, 373 (2020).

[17] M. Sigrist and K. Ueda, Reviews of Modern physics **63**, 239 (1991).

[18] Y. Maeno, H. Hashimoto, K. Y. S. Nishizaki, T. Fujita, J. G. Bednorz, and F. Lichtenberg, Nature **372**, 532 (1994).

[19] K. Ishida, H. Mukuda, Y. Kitaoka, K. Asayama, Z. Q. Mao, Y. Mori, and Y. Maeno, Nature **396**, 658 (1998).

[20] J. A. Duffy, S. M. Hayden, Y. Maeno, Z. Mao, J. Kulda, and G. J. McIntyre, Phys. Rev. Lett. **85**, 5412 (2000).

[21] A. Pustogow, Y. Luo, A. Chronister, Y.-S. Su, D. A. Sokolov, F. Jerzembeck, A. P. Mackenzie, C. W. Hicks, N. Kikugawa, S. Raghu, E. D. Bauer, and S. E. Brown, Nature **574**, 72 (2019).

[22] K. Ishida, M. Manago, K. Kinjo, and Y. Maeno, J. Phys. Soc. Jpn. **89**, 034712 (2020).

[23] G. R. Stewart, Z. Fisk, J. O. Willis, and J. L. Smith, Phys. Rev. Lett. **52**, 679 (1984).

[24] N. T. Huy, A. Gasparini, D. E. de Nijs, Y. Huang, J. C. P. Klaasse, T. Gortenmulder, A. de Visser, A. Hamann, T. Görlach, and H. v. Löhneysen, Physical review letters **99**, 067006 (2007).

[25] S. Ran, C. Eckberg, Q.-P. Ding, Y. Furukawa, T. Metz, S. R. Saha, I.-L. Liu, M. Zic, H. Kim, J. Paglione, and N. P. Butch, Science **365**, 684 (2019).

[26] D. D. Osheroff, R. C. Richardson, and D. M. Lee, Phys. Rev. Lett. **28**, 885 (1972).

[27] M. Sato, Y. Tanaka, K. Yada, and T. Yokoyama, Phys. Rev. B **83**, 224511 (2011).

[28] V. Mourik, K. Zuo, S. M. Frolov, S. Plissard, E. P. Bakkers, and L. P. Kouwenhoven, Science **336**, 1003 (2012).

[29] A. Das, Y. Ronen, Y. Most, Y. Oreg, M. Heiblum, and H. Shtrikman, Nat. Phys. **8**, 887 (2012).

[30] C. Nayak, S. H. Simon, A. Stern, M. Freedman, and S. DasSarma, Rev. Mod. Phys. **80**, 1083 (2008).

[31] R. M. Lutchyn, J. D. Sau, and S. D. Sarma, Phys. Rev. Lett. **105**, 077001 (2010).

[32] Y. Oreg, G. Refael, and F. von Oppen, Phys. Rev. Lett. **105**, 177002 (2010).

[33] M. Sato, Y. Takahashi, and S. Fujimoto, Phys. Rev. Lett. **103**, 020401 (2009).

[34] M. Sato, Y. Takahashi, and S. Fujimoto, Phys. Rev. B **82**, 134521 (2010).

[35] V. L. Berezinskii, JETP Lett. **20**, 287 (1974).

[36] A. Balatsky and E. Abrahams, Phys. Rev. B **45**, 13125 (1992).

[37] J. Linder and J. W. Robinson, Nat. Phys. **11**, 307 (2015).

[38] Y. Tanaka, A. A. Golubov, S. Kashiwaya, and M. Ueda, Phys. Rev. Lett. **99**, 037005 (2007).

[39] S.-P. Lee, R. M. Lutchyn, and J. Maciejko, Phys. Rev. B **95**, 184506 (2017).

[40] F. S. Bergeret, A. F. Volkov, and K. B. Efetov, Phys. Rev. Lett. **86**, 4096 (2001).

[41] A. D. Bernardo, Z. Salman, X. L. Wang, M. Amado, M. Egilmez, M. G. Flokstra, A. Suter, S. L. Lee, J. H. Zhao, T. Prokscha, , E. Morenzoni, M. G. Blamire, J. Linder, and J. W. A. Robinson, Phys. Rev. X **5**, 041021 (2015).

[42] Y. Tanaka and S. Kashiwaya, Phys. Rev. B **70**, 012507 (2004).

[43] Y. Tanaka, S. Kashiwaya, and T. Yokoyama, Phys. Rev. B **71**, 094513 (2005).

[44] Y. Asano, Y. Tanaka, and S. Kashiwaya, Phys. Rev. Lett. **96**, 097007 (2006).

[45] S.-I. Suzuki and Y. Asano, Phys. Rev. B **89**, 184508 (2014).

[46] S.-I. Suzuki and Y. Asano, Phys. Rev. B **91**, 214510 (2015).

[47] D. Takagi, S. Tamura, and Y. Tanaka, arXiv: 1809.09324v4 (2020).

[48] L. J. Buchholtz and G. Zwicknagl, Phys. Rev. B **23**, 5788 (1981).

[49] J. Hara and K. Nagai, Prog. of Theor. Phys. **76**, 1237 (1986).

[50] C. R. Hu, Phys. Rev. Lett. **72**, 1526 (1994).

[51] Y. Tanaka and S. Kashiwaya, Phys. Rev. Lett. **74**, 3451 (1995).

[52] S. Kashiwaya and Y. Tanaka, Rep. Prog. Phys. **63**, 1641 (2000).

[53] Y. Tanaka, M. Sato, and N. Nagaosa, J. Phys. Soc. Jpn. **81**, 011013 (2012).

[54] S. Ikegaya, S.-I. Suzuki, Y. Tanaka, and Y. Asano, Phys. Rev. B **94**, 054512 (2016).

[55] A. A. Golubov and M. Y. Kupriyanov, J. Low Tem. Phys. **70**, 83 (1988).

[56] J. W. Serene and D. Rainer, Phys. Rep. **101**, 221 (1983).

[57] G. Eilenberger, Z. Phys. **214**, 195 (1968).

[58] M. Eschrig, Phys. Rev. B **61**, 9061 (2000).

[59] H. Ebisu, K. Yada, H. Kasai, and Y. Tanaka, Phys. Rev. B **91**, 054518 (2015).

[60] P. A. Lee and D. S. Fisher, Phys. Rev. Lett. **47**, 882 (1981).

[61] S. S. Hegde and S. Vishveshwara, Phys. Rev. B **94**, 115166 (2016).

[62] S. Higashitani, S. Matsuo, Y. Nagato, K. Nagai, S. Murakawa, R. Nomura, and Y. Okuda, Phys. Rev. B **85**, 024524 (2012).

[63] Y. Tanaka, Y. V. Nazarov, A. A. Golubov, and S. Kashiwaya, Phys. Rev. B **69**, 144519 (2004).

[64] P. Burset, B. Lu, S. Tamura, and Y. Tanaka, Phys. Rev. B **95**, 224502 (2017).

[65] M. T. Mercaldo, M. Cuoco, and P. Kotetes, Physica B **536**, 730 (2018).

[66] J. Cayao, C. Triola, and A. M. Black-Schaffer, The European Physical Journal Special Topics **229**, 545 (2020).

[67] A. Daido and Y. Yanase, Phys. Rev. B **100**, 174512 (2019).

[68] S. Mishra, S. Tamura, A. Kobayashi, and Y. Tanaka, Phys. Rev. B **103**, 024501 (2021).

[69] F. S. Bergeret, A. F. Volkov, and K. B. Efetov, Rev. Mod. Phys. **77**, 1321 (2005).

[70] A. I. Buzdin, Rev. Mod. Phys. **77**, 935 (2005).

[71] M. Eschrig, Rep. Prog. Phys. **78**, 104501 (2015).

[72] A. A. Golubov, M. Y. Kupriyanov, and E. Ilichev, Rev. Mod. Phys. **76**, 411 (2004).